UNIVERSITÀ
DI PAVIA

Department of Chemistry
Head of Department Prof. **Mauro Freccero**

Master's Degree Programme in Chemistry

Disclosing Ancient Islamic Glaze Technology at Mértola (Portugal) by Ancient Ceramics Analysis and Experimental Replicas

Supervisor:
Ch.mo Prof. Malavasi Lorenzo

Co-supervisors:
Prof. Massimo Beltrame,
Prof. Mathilda Larsson Dias Coutinho

Author:
Maddalena Franzosi

Academic Year 2025 / 2026

List of Figures

Figure 1.. Spettri Raman normalizzati: cenere d'osso pura (nero), campione archeologico 666 zona verde (verde), replica sperimentale R7 (rosso). I tre spettri condividono la banda a 962 cm^{-1} (ν_1 PO_4^{3-}, apatite). Bande a 464 cm^{-1} (quarzo) e 633 cm^{-1} (SnO_2) visibili nella replica. X
Figure 2. Spettro Raman della ricetta Purple (P). Il quarzo (~464 cm^{-1}) domina; la regione 900–1000 cm^{-1} mostra solo una debole modulazione: fusione incompleta impedisce la cristallizzazione del fosfato di calcio. XI
Figure 3. Spettro Raman della ricetta Yellow (Y). Bande a 207 e 462 cm^{-1} (vetro e quarzo). Nessun picco di cassiterite (633 cm^{-1}) né di apatite (962 cm^{-1}): lo SnO_2 aggiunto resta dissolto nel vetro, la cenere d'osso è assente dalla formulazione. XI
Figure 4. Mappa EDS (Si blu, P giallo) della replica R7 (RED, 700 °C). Le inclusioni gialle ricche in P sono grani di cenere d'osso nella matrice piombo-silicatica. Scala: 100 µm XI
Figure 5.Mappa EDS (Si rosa, Pb rosa) della ricetta Y (700 °C). Nessuna inclusione fosfatica; le sfere grigie sono bolle d'aria. Scala: 100 µm. XII
Figure 6. Immagine di microscopia digitale della sezione trasversale del campione archeologico 1668. L'invetriatura contiene inclusioni bianche (SnO_2) sul corpo ceramico calcareo. Scala: 200 µm. XIII
Figure 7 Map of the Iberian Peninsula under Umayyad control, c. 750 AD. The highlighted marker indicates the location of Mértola, the primary site examined in this study. 5
Figure 8. example of crazing 11
Figure 9. Panoramic view of the town of Mértola and the Guadiana River, southern Portugal, illustrating its strategic position as a primary river port. 14
Figure 10. Photographs and Digital microscopy images of archaeological samples:(a) crvm1668, (b) crvm666, (c)crvm623, at 20× magnificaton 14
Bone ash from raw bovine cortical bone (Figure 11) was used as the key glaze additive for this study. In the context of glaze technology, bone ash is of interest as a potential opacifying agent: the refractive index of hydroxyapatite (~1.64) differs from that of a lead-silicate glass matrix (~1.9–2.1) sufficiently to generate light scattering at the particle–glass interface, and the material would have been locally and cheaply available as a by-product of butchery and food processing in any medieval urban context. 14
Figure 12. Photographs of raw bone 15
Figure 13 PbO-SiO_2 phase diagram highlighting equilibrium cristobalite (Pb_2SiO_4 at ~724°C) and liquidus (~1477°C) for glaze compositions (0.22–0.60 SiO_2 mole fraction). Firing at 959–1100°C drives partial crystallization, with bone ash influencing Ca-Si-P phases 16
Figure 14. Bone ash preparation images 22
Figure 15. set of replicas 22
Figure 16. XRD pattern of bone ash calcinated at 1000°C for 2 hours. Reflections are consistent with phase-pure hydroxyapatite ($Ca_{10}(PO_4)_6(OH)_2$). 30
Figure 17. TGA/DTA/DTG curves of raw bone ash. Three mass loss events are identified: moisture release below 200°C (−4.17%), organic matter combustion between 250–500°C (−20.42%), and phosphate/carbonate group dissociation between 600–800°C (−3.5%). 31
Figure 18. TGA/DTA/DTG curves of bone ash calcinated at 1000°C for 2 hours. Total mass loss below 1.2% with no significant thermal events, confirming complete removal of organic matter and thermal stability of the hydroxyapatite phase. The apparent mass increase at low temperature is a buoyancy artefact 32
Figure 19. FTIR spectrum of raw (not calcinated) bone ash. Bands at 1650 cm^{-1} (amide I, collagen), 1450 and 1415 cm^{-1} (ν_3 CO_3^{2-}), and 1080/565/603 cm^{-1} (ν_3 and ν_4 PO_4^{3-}) reflect the mixed organic–inorganic composition of unprocessed bone. The broad phosphate bands indicate lower crystallinity relative to the calcinated sample. 33
Figure 20. FTIR spectrum of calcinated bone ash (1000°C, 2 h). Principal bands: structural O–H stretching at 3571 cm^{-1}, ν_3 PO_4^{3-} at 1028 cm^{-1} (sharp, well-resolved), ν_4 PO_4^{3-} doublet at 565 cm^{-1}.

The sharpness of the phosphate bands reflects the high crystallinity of the calcinated material. Normalised absorbance..... 34
Figure 21. Raman spectrum of calcinated bone ash (1000°C, 2 h). Dominant band at 962 cm^{-1} (ν_1 PO_4^{3-} symmetric stretching). Band at 432 cm^{-1} assigned to ν_2 PO_4^{3-}. Normalised intensity (a.u.).. 35
Figure 22. Raman spectrum of NIST SRM 1400 (Bone Ash), measured as reference material. Dominant band at 962 cm^{-1} (ν_1 PO_4^{3-}). Band at 590 cm^{-1} assigned to ν_4 PO_4^{3-}. The broader baseline relative to the calcinated sample reflects the lower crystallinity of the commercial standard. Normalised intensity (a.u.). 35
Figure 23. XRPD pattern of the ceramic body fired at 950°C. Intensities are normalized (a.u.) to highlight the mineralogical phases and crystallinity at intermediate firing stages. 38
Figure 24**.** XRPD pattern of the ceramic body fired at 1100°C. Intensities are normalized (a.u.), showing the phase transformations and mineralogical evolution at the peak firing temperature 39
Figure 25. XRPD patterns of the ceramic body samples showing the thermal mineralogical evolution from the pre-fired state up to 1100. The stacked plot illustrates the phase transformations as a function of firing temperature and holding time. Intensities are normalized and displayed in arbitrary units with a vertical offset applied to the patterns to facilitate comparative analysis of peak intensity and crystallinity..... 40
Figure 26. SEM-BSE micrographs illustrating the microstructural evolution of the ceramic body: **(a)** Pre-fired state showing a porous matrix with unreacted clay aggregates and quartz inclusions; **(b)** 950°C showing incipient sintering and early glassy phase formation; **(c)** 1100°C (2 h) showing advanced densification and partial quartz dissolution; **(d)** 1100°C (6 h) showing a mature microstructure with enhanced vitrification and phase coarsening due to prolonged soaking. 41
Figure 27.. Projection of the bulk XRF composition (normalised to the CaO +MgO–Al_2O_3–SiO_2 ternary system) of the pre-fired calcareous ceramic tiles. The sample plots in the transitional zone between the gehlenite and anorthite stability fields, consistent with the phase assemblage observed by XRD at 950°C and 1100°C respectively. Phase field boundaries are approximate and based on the NIST CaO–Al_2O_3–SiO_2 system. 43
Figure 28. Digital Microscopy image in PL & XPL,, and EDS elemental mapping of sample CRVM666 GREEN, with detail of SEM-EDS composite elemental map of the glaze (Ca = red, P = blue). The distinct magenta coloration of the dispersed acicular (needle-like) crystals reveals a perfect spatial correlation between calcium and phosphorus, confirming the widespread precipitation of a calcium phosphate phase. 46
Figure 29. Raman spectrum of crvm666 GREEN SPOT 47
Figure 30. Digital Microscopy image in PL & XPL, SEM-BSE image, and EDS elemental mapping of sample CRVM666 BLACK 48
Figure 31. Raman spectrum of crvm666 BLACK SPOT 49
Figure 32. Digital Microscopy image in PL & XPL, SEM-BSE image, and EDS elemental mapping of sample CRVM1668 GREEN. 50
Figure 33. Digital Microscopy image in PL & XPL, SEM-BSE image, and detail of sample CRVM1668 BLACK. 52
Figure 34. Raman spectrum of sample CRVM1668 BLACK. 52
Figure 35. SEM-BSE image of sample CRVM623 “under”, and EDS elemental mapping of a detail. 54
Figure 36. Digital Microscopy image at [1000x] magnification, SEM-BSE image, and EDS elemental mapping of sample R7. 55
Figure 37. Raman spectrum of sample R7, ... 55
Figure 38. Digital Microscopy image at [1000x] magnification, SEM-BSE image, and EDS elemental mapping of sample R8. 56
Figure 39. Raman spectrum of sample R8, ... 56
Figure 40. Figure X. Digital Microscopy image at [1000x] magnification, SEM-BSE image, and EDS elemental mapping of sample R9. 57
Figure 41. Raman spectrum of sample R9 57

Figure 42. Digital Microscopy images at [700x high and 200x mid] magnification, and EDS elemental mapping of sample Y7. 58
Figure 43. Raman spectrum of sample Y7 58
Figure 44. Digital Microscopy images at [200x] magnification, SEM-BSE image, and EDS elemental mapping of sample P8. 60
Figure 45. Raman spectrum of sample P8. 60
Figure 46. Digital Microscopy images at [200x] magnification, SEM-BSE images of samples L7 and L8 62
Figure 47. Overlaid Raman spectra comparison between Pure Bone Ash (black), Archaeological sample CRVM666 (green), and Experimental Replica R7 (red). The spectra are normalized and corrected for instrumental shift (-6 cm^{-1}). The diagnostic peak for hydroxyapatite is highlighted at 962 cm^{-1}. 67
Figure 48. Digital Microscopy image at [140x] magnification of mid B7 and high B7 at [2000x] magnification, SEM-BSE image of B7 detail. 68
Figure 49. SEM-BSE image of Y8 sample, Digital Microscopy image at [100x] magnification of mid Y8 and at [50x] magnification. 69
Figure 50. Digital Microscopy image at [400x] magnification of mid R9 sample, and EDS elemental mapping. 70
Figure 51. EDS elemental mapping comparing samples Y8 and Y9, demonstrating a significant decrease in crystallite density as firing temperature increases. 70
Figure 52. SEM-BSE image of archaeological sample 71
Table 21. Figure 53 72
Figure 54. EDS elemental mappings of sample CRVM666. 72

List of tables

Table 1.Oxide composition (wt%) of the four raw materials used in this study. Only the principal oxides are listed; trace components and volatiles (CO2 from bone ash) are omitted for clarity..... 17
Table 2**.** Top: weight percentages of raw materials for each recipe. Bottom: resulting theoretical oxide composition and molar ratio [mol SiO^2 / (mol SiO^2 + mol PbO)]. LT599 = pure frit (transparent lead glaze baseline). R, P, B contain bone ash; Y does not. Dash (—) = not added. 17
Table 3. Detailed molar ratio calculation: PbO and SiO^2 total weight percentages from Table 2, converted to moles using Mw(PbO) = 223.19 g/mol, Mw(SiO^2) = 60.08 g/mol. Note that Red and LT599 share the same molar ratio because the added bone ash and SnO^2 do not contribute PbO or SiO^2..... 18
Table 4**.** Weighed amounts of each raw material for a total batch mass of 7.5 g per recipe. Each batch was suspended in water for application to the ceramic tiles. A dash (—) indicates the component was not included. 20
Table 5. Complete experimental matrix: 5 glaze compositions × 3 firing temperatures = 15 individual samples. Recipes are ordered by increasing molar ratio. All tiles were biscuit-fired at 950 °C prior to glaze application. 21
Table 6: Bulk chemical composition of bone ash determined by XR. Major oxides in wt.%, trace elements in ppm. Statistical error is the 1σ counting error. Elements below the lower limit of detection are not reported. 29
Table 7. Summary of mass loss events identified by TGA for raw bone ash. Temperature ranges and corresponding thermal processes are based on the TG/DTG curves (Figure 17). 31
Table 8. Bulk chemical composition of pre-fired calcareous ceramic tiles determined by XRF. Values are expressed as mean wt.% ± standard deviation (SD) of n = 3 replicates. %RSD = relative standard deviation. — indicates SD = 0.00 or concentration below reliable quantification threshold 36
Table 9. Semi-quantitative phase composition of the ceramic body at four thermal conditions, determined by the RIR method. Values in wt%. "/" = phase not detected. 41
Table 10. Quantitative chemical composition (wt.%) of the glaze oxides determined by EDS analysis. 47
Table 11. Quantitative chemical composition (wt.%) of the glaze oxides determined by EDS analysis. 48
Table 12. Quantitative chemical composition (wt.%) of the glaze oxides determined by EDS analysis. 51
Table 13. Quantitative chemical composition (wt.%) of the glaze oxides determined by EDS analysis. 52
Table 14. Quantitative chemical composition (wt.%) of the glaze oxides determined by EDS analysis. 54
Table 15. Quantitative chemical composition (wt.%) of the glaze oxides determined by EDS analysis. 55
Table 16. Quantitative chemical composition (wt.%) of the glaze oxides determined by EDS analysis. 56
Table 17. Quantitative chemical composition (wt.%) of the glaze oxides determined by EDS analysis. 57
Table 18. Quantitative chemical composition (wt.%) of the glaze oxides determined by EDS analysis. 58
Table 19. Quantitative chemical composition (wt.%) of the glaze oxides determined by EDS analysis. 60
Table 20.. Quantitative chemical composition (wt.%) of the glaze oxides determined by EDS analysis. 62
Table 21. Figure 53..... 72

Table of Contents

List of Figures ..... ***II***

List of tables ..... ***V***

Abstract ..... ***IX***

Resumo ..... ***XIV***

Introduction ***1***

Research objectives ***3***

1. Historical Background ***5***

1.1 The Islamic Period in the Iberian Peninsula **5**

1.3 Origins of Glazed Ceramic Technology **6**

1.4 Introduction of Glaze Technology in al-Andalus **7**

2. Technology of Islamic Ceramics ***8***

2.1 The Ceramic Body **8**

2.2 Glazes: Definition and Structure **9**

2.4 Ceramic body and the Glaze Interaction **10**

2.5 Opacifiers: Tin Oxide, Bone Ash, and Quartz **11**

2.6 Colourants and Decoration **12**

3. Materials ***13***

3.1. Archaeological samples: Mértola and the Gharb al-Andalus **13**

3.2 Experimental Replicas **14**

3.2.1 Design and Formulation of the Experimental Glaze Recipes 15

4. Methods and analytical techniques ***22***

4.2.1. Digital Optical Microscopy (DOM) 23

4.2.2 X-ray Powder Diffraction (XRPD) 23

4.2.3 Scanning Electron Microscopy with Energy Dispersive Spectroscopy (SEM-EDS) 24

4.2.4 Raman Spectroscopy 24

4.2.5 Thermogravimetric Analysis (TGA) 25

4.2.6 X-ray Fluorescence (XRF) 26

4.2.7 Fourier-Transform Infrared Spectroscopy (FTIR) 26

5.1 Characterization of bone ashes **28**

5.1.1. X-Ray Fluorescence (XRF) Analysis 28

5.1.4. FT-IR Spectroscopy Analysis 32

5.1.5 Raman Spectroscopy Analysis 34

5.2. Characterisation of the ceramic body **36**

5.2.1 X-Ray Fluorescence (XRF) Analysis 36

4.2 X-Ray Diffraction Powder (XRDP) Analysis 38

5.2.2 Scanning Electron Microscopy: microstructural evolution of the ceramic body 41

5.3 Characterisation of archaeological samples: DMI, SEM Images, Raman Spectra, EDS quantifications **46**

CRVM666 GREEN 46

..... 46

CRVM666 BLACK 48

CRWM1668 GREEN 50

CRVM1668 BLACK 52
CRVM623 54
SECONDARY GLAZE 54

5.4 Characterisation of replicas: DM, SEM Images, Raman Spectra, EDS quantifications 55
R7 55
R8 56
R9 57
Y7 58
P8 60

6. Discussion*..... *64

6.1 Experimental recipes vs. theoretical targets.....64

6.2 Bone ash identification 65

6.3 Opacification mechanisms.....68

6.4 Glaze–body interface and digestion process.....71

6.5 Comparison with archaeological samples.....73

6.6 Expected vs. observed outcomes.....74

References*..... *78

Supporting info*..... *82

Acknowledgements*..... *83

Abstract

Le ceramiche islamiche invetriate al piombo recuperate a Mértola, un sito urbano nel sud del Portogallo sotto amministrazione islamica dall'VIII al XIII secolo, sollevano una questione tecnologica ancora aperta: quali materie prime venivano impiegate per opacizzare le invetriature? L'ossido di stagno (SnO_2) è l'opacizzante tradizionalmente riconosciuto, ma la sua disponibilità nella penisola iberica è legata a depositi situati nel nord della regione, e la progressiva perdita di controllo su queste fonti da parte degli artigiani del sud ha posto la questione se materiali alternativi fossero stati impiegati. Studi precedenti hanno rilevato fosforo e calcio in invetriature archeologiche, suggerendo l'uso della cenere d'osso—un materiale a base di idrossiapatite, $Ca_5(PO_4)_3(OH)$—come agente opacizzante. Manca tuttavia una dimostrazione sperimentale diretta. Questa tesi affronta il problema combinando la replicazione sperimentale di invetriature al piombo con la caratterizzazione multi-analitica (OM, SEM-BSE, EDS, spettroscopia Raman) sia delle repliche sia dei campioni archeologici.

La formulazione delle ricette sperimentali è partita dal diagramma di fase binario $PbO–SiO_2$, che ha guidato la selezione di cinque composizioni con rapporti molari SiO_2/PbO crescenti: LT599 e Red (R) a 0,553, Yellow (Y) a 0,635, Blue (B) a 0,648 e Purple (P) a 0,783. Tutte condividono la medesima fritta piombo-silicatica (LT599) come base. Tre ricette (R, B, P) contengono cenere d'osso (0,375 g per lotto di 7,5 g) con SnO_2 e SiO_2; due (LT599, Y) fungono da controlli privi di cenere d'osso. Ciascuna ricetta è stata applicata su piastrelle ceramiche calcaree previamente cotte a 950 °C (biscotto) e sottoposta a seconda cottura a 700, 800 o 900 °C, seguendo un protocollo di doppia cottura. La matrice sperimentale comprende 15 campioni. In parallelo sono stati analizzati tre campioni archeologici da Mértola (CRVM623, CRVM666, CRVM1668), con analisi EDS condotte su zone di invetriatura distinte (nero, verde, under, bianco).

Il risultato centrale è l'identificazione della cenere d'osso tramite spettroscopia Raman. Le repliche contenenti cenere d'osso (R7, R8, R9—ricetta RED a 700, 800 e 900 °C) mostrano una banda intensa a ~962–965 cm^{-1}, corrispondente al modo ν_1 del tetraedro PO_4^{3-} nelle fasi di fosfato di calcio, in sovrapposizione precisa con lo spettro della cenere d'osso pura di riferimento. La stessa banda è stata rilevata nei campioni archeologici CRVM666 e CRVM1668 (Figura 1). L'identificazione dei cristalliti di fosfato di calcio tramite micro-Raman si è rivelata complessa in tutti i campioni archeologici, poiché le particelle sono estremamente fini e disperse nella matrice vetrosa; ciononostante, un segnale diagnostico è stato ottenuto in due campioni su tre. Nel campione CRVM623 non è stato possibile estrarre un segnale Raman consistente a causa delle dimensioni ridotte dei cristalliti.

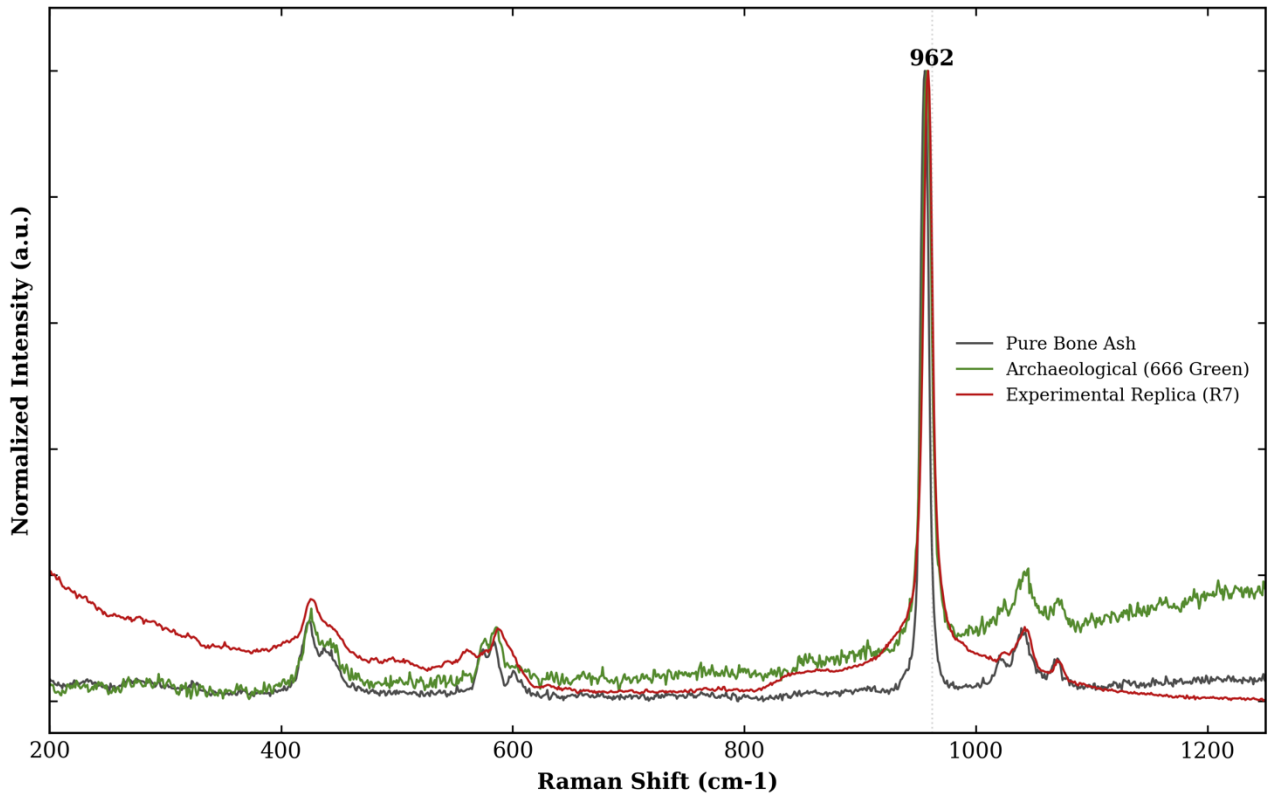


Figure 1.. Spettri Raman normalizzati: cenere d'osso pura (nero), campione archeologico 666 zona verde (verde), replica sperimentale R7 (rosso). I tre spettri condividono la banda a 962 cm⁻¹ (ν_1 PO_4^{3-}, apatite). Bande a 464 cm⁻¹ (quarzo) e 633 cm⁻¹ (SnO_2) visibili nella replica.

La specificità diagnostica del picco è confermata dai controlli. La ricetta Y, priva di cenere d'osso, non presenta alcuna banda nella regione 960–970 cm^{-1} (Figure 3): il suo spettro mostra solo i modi del vetro piombo-silicatico e del quarzo (207 e 462 cm^{-1}), senza traccia di cassiterite né di fosfato di calcio. L'assenza del picco SnO_2 nel controllo Y indica che la quantità di ossido di stagno aggiunta non è sufficiente a produrre la precipitazione di cassiterite rilevabile al Raman: lo stagno resta dissolto nella matrice vetrosa. Questo dato ha implicazioni per l'interpretazione archeologica: concentrazioni di Sn nell'invetriatura non equivalgono automaticamente alla presenza di cassiterite come fase opacizzante. La ricetta Purple (Figure 2), che contiene cenere d'osso ma possiede il rapporto molare più elevato (0,783), non mostra un picco di apatite ben risolto: il suo spettro è dominato dal quarzo con solo una debole modulazione nella regione 900–1000 cm^{-1}. A rapporti molari così elevati la matrice non raggiunge una fusione sufficiente, nemmeno a 900 °C, per la completa dissoluzione e riprecipitazione della cenere d'osso. P funge da test negativo interno: la sola presenza di cenere d'osso nella formulazione non basta a produrre la firma Raman se le condizioni di fusione non sono adeguate.

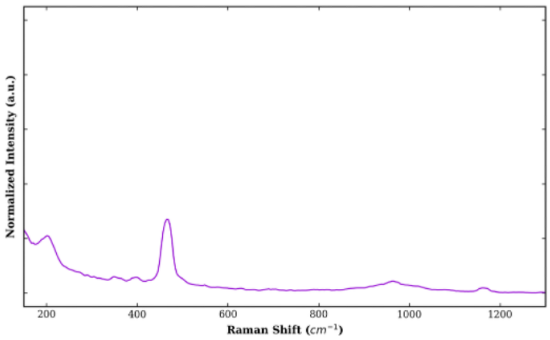


Figure 2. Spettro Raman della ricetta Purple (P). Il quarzo (~464 cm⁻¹) domina; la regione 900–1000 cm⁻¹ mostra solo una debole modulazione: fusione incompleta impedisce la cristallizzazione del fosfato di calcio.

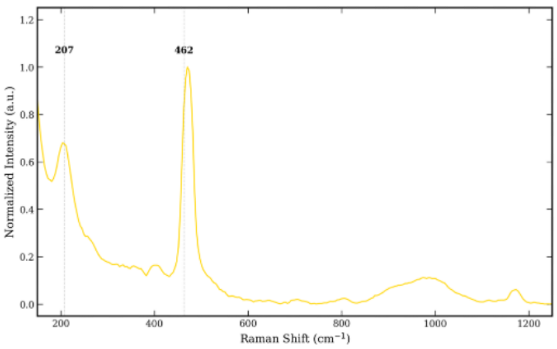


Figure 3. Spettro Raman della ricetta Yellow (Y). Bande a 207 e 462 cm⁻¹ (vetro e quarzo). Nessun picco di cassiterite (633 cm⁻¹) né di apatite (962 cm⁻¹): lo SnO_2 aggiunto resta dissolto nel vetro, la cenere d'osso è assente dalla formulazione.

Le mappe EDS confermano il dato Raman. La mappa Si/P della replica R7 (Figure 4) mostra inclusioni ricche in fosforo (gialle) distribuite nella matrice piombo-silicatica (blu): grani di cenere d'osso parzialmente dissolti. La mappa Si/Pb della ricetta Y (Figure 5) mostra una matrice omogenea senza inclusioni fosfatiche, ma con abbondanti bolle sferiche che a 700 °C rappresentano il meccanismo dominante di opacificazione per diffusione della luce. Le immagini SEM-BSE delle repliche con cenere d'osso rivelano due popolazioni di inclusioni: particelle ad alto contrasto (aggregati di SnO_2) e particelle a basso contrasto le cui analisi puntuali EDS restituiscono Ca e P elevati, coerenti con grani di idrossiapatite. Queste ultime sono assenti nei controlli.

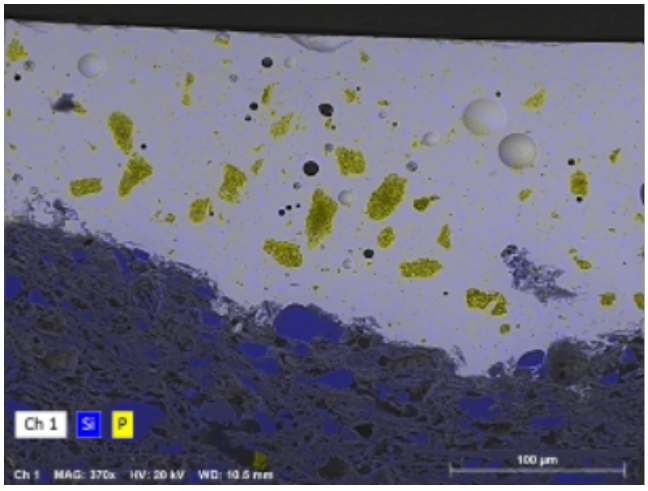


Figure 4. Mappa EDS (Si blu, P giallo) della replica R7 (RED, 700 °C). Le inclusioni gialle ricche in P sono grani di cenere d'osso nella matrice piombo-silicatica. Scala: 100 µm

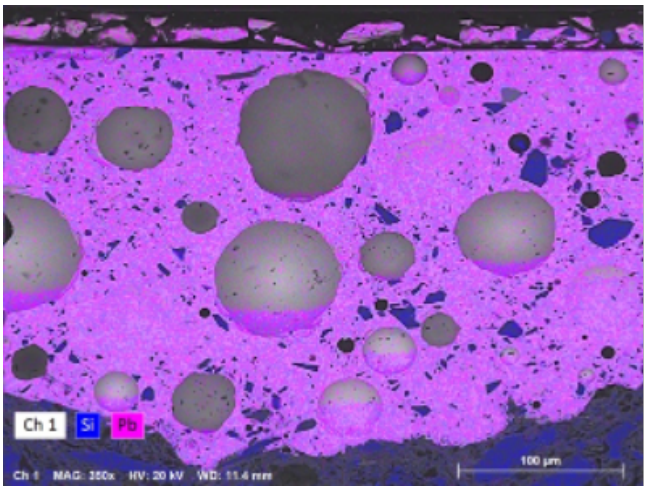


Figure 5.Mappa EDS (Si rosa, Pb rosa) della ricetta Y (700 °C). Nessuna inclusione fosfatica; le sfere grigie sono bolle d'aria. Scala: 100 µm.

Il meccanismo di opacificazione varia con la temperatura. A 700 °C la matrice non è completamente fusa e l'aspetto bianco è prodotto dalle bolle d'aria intrappolate. A 800–900 °C le bolle vengono espulse e l'opacità dipende dalla cristallizzazione di fosfato di calcio e ossido di stagno. I dati EDS confermano che Ca e P si concentrano nella porzione superiore dell'invetriatura a 900 °C (RED top: Ca = 5,69 wt%, P = 4,00 wt%). L'opacificazione efficace tramite SnO_2 richiede concentrazioni superiori a quanto previsto dal calcolo di formulazione: nelle repliche RED il contenuto medio di Sn (R7: 1,71; R8: 1,93; R9: 2,06 wt%) corrisponde a un'opacità modesta, indicando che gran parte dello stagno resta dissolto nel vetro.

L'interazione tra invetriatura e corpo ceramico durante la seconda cottura produce una zona di reazione all'interfaccia (digestione), caratterizzata dalla decomposizione delle fasi argillose, dalla diffusione elementare e dalla formazione di nuove fasi cristalline. Le mappe EDS delle repliche confermano che Al, Fe, Ca e K aumentano dalla sommità dell'invetriatura verso il corpo, mentre Pb e Si diminuiscono. Nella ricetta RED il gradiente si accentua con la temperatura: a 700 °C, Al passa da 1,63 wt% (top) a 3,21 wt% (bottom); a 900 °C, da 1,58 a 5,35 wt%.

Il confronto con i campioni archeologici rafforza le conclusioni. Il campione CRVM666 presenta fosforo nelle zone nero (3,01 wt%) e verde (2,04 wt%) con Ca elevato (6,67 e 5,27 wt%), mentre le zone bianco e under non contengono fosforo rilevabile: distribuzione coerente con l'aggiunta selettiva di cenere d'osso nelle aree di decorazione colorate. Il Raman ha confermato la presenza di apatite in CRVM666 e in CRVM1668. Nel campione CRVM623 non è stato possibile estrarre un segnale Raman consistente a causa delle dimensioni ridotte dei cristalliti. Il campione CRVM1668 (Figure 6) mostra P non rilevabile all'EDS areale ma Sn elevato nella zona bianca (2,77 wt%); il segnale Raman di apatite rilevato indica la co-presenza di cenere d'osso e ossido di stagno, con quest'ultimo come opacizzante dominante.



Figure 6. Immagine di microscopia digitale della sezione trasversale del campione archeologico 1668. L'invetriatura contiene inclusioni bianche (SnO_2) sul corpo ceramico calcareo. Scala: 200 µm.

La convergenza di evidenze Raman, EDS e microstrutturali costituisce, per quanto è a conoscenza dell'autrice, la prima dimostrazione sperimentale che la cenere d'osso è stata impiegata come opacizzante alternativo nella tradizione ceramica islamica. I dati suggeriscono un'adattamento tecnologico locale: l'uso della cenere d'osso riflette probabilmente la perdita dell'accesso alle fonti di stagno nel nord della penisola iberica, mentre la formulazione generale dell'invetriatura—un sistema ad alto piombo e bassa silice su corpi calcarei—resta coerente con la più ampia tradizione islamica, indicando che il sapere tecnologico di base era preservato anche quando le specifiche materie prime venivano sostituite. Le repliche sperimentali forniscono un quadro di riferimento calibrato per l'interpretazione archeometrica delle invetriature al piombo islamiche.

Resumo

Esta dissertação investiga a tecnologia de produção de cerâmicas islâmicas vidradas a chumbo recuperadas em Mértola, um sítio urbano do sul de Portugal sob administração islâmica do século VIII ao século XIII. O objetivo central é a identificação dos agentes opacificantes utilizados nos vidrados, com especial atenção à hipótese de que cinza de osso—um material à base de hidroxiapatite, $Ca_5(PO_4)_3(OH)$—tenha sido empregue como alternativa ao óxido de estanho (SnO_2), cujo acesso se tornou progressivamente difícil devido à localização das fontes de estanho no norte da península Ibérica.

O trabalho combina a caracterização analítica de três amostras arqueológicas de Mértola (CRVM623, CRVM666, CRVM1668) com um programa de replicação experimental. Cinco receitas de vidrado foram formuladas a partir do diagrama de fases binário $PbO–SiO_2$, com razões molares SiO_2/PbO crescentes (0,553 a 0,783). Três receitas (R, B, P) contendo cinza de osso e duas de controlo sem cinza de osso (LT599, Y) foram aplicadas sobre placas cerâmicas calcárias previamente cozidas a 950 °C (biscoito) e submetidas a segunda cozão a 700, 800 ou 900 °C, num total de 15 amostras. Todas as caracterizações foram realizadas por microscopia óptica (OM), SEM-BSE, EDS e espectroscopia Raman.

O resultado central é a identificação da cinza de osso por espectroscopia Raman. As réplicas contendo cinza de osso (R7, R8, R9) apresentam uma banda intensa a ~962–965 cm^{-1}, correspondente ao modo ν_1 do tetraedro PO_4^{3-} em fases de fosfato de cálcio, em sobreposição precisa com o espectro da cinza de osso pura de referência. As receitas de controlo (LT599, Y) não apresentam esta banda, confirmando a sua especificidade diagnóstica. A mesma assinatura Raman foi detetada nas amostras arqueológicas CRVM666 e CRVM1668, constituindo evidência direta de que os oleiros islâmicos utilizavam cinza de osso como matéria-prima opacificante. Na amostra CRVM623, os cristalitos de fosfato de cálcio são demasiado finos e dispersos para a extração de um sinal Raman consistente, embora dados complementares de EDS apoiem a presença de material derivado de apatite. Os mapas elementares EDS das réplicas confirmam a presença de inclusões ricas em fósforo nas receitas com cinza de osso e a sua ausência nos controlos.

Os mecanismos de opacificação variam com a temperatura: a 700 °C dominam as bolhas de ar na matriz não completamente fundida; a 800–900 °C, o fosfato de cálcio cristalino e o óxido de estanho tornam-se os principais centros de dispersão óptica. A opacificação eficaz por SnO_2 requer concentrações superiores às previstas pelo cálculo de formulação: uma fração significativa do estanho permanece dissolvida na matriz vítrea. A convergência de evidências Raman, EDS e microestruturais

constitui, tanto quanto é do conhecimento da autora, a primeira demonstração experimental de que a cinza de osso foi utilizada como opacificante alternativo na tradição cerâmica islâmica vidrada, refletindo provavelmente uma adaptação tecnológica local face à perda de acesso às fontes de estanho. As réplicas experimentais fornecem um quadro de referência calibrado para a interpretação arqueométrica dos vidrados islâmicos a chumbo.

Introduction

Ceramic materials are among the most widespread and long-lasting products of human craftsmanship. They are obtained by shaping and firing clay-based mixtures, which typically consist of fine-grained minerals — primarily phyllosilicates — combined with non-plastic additives that improve workability and reduce deformation during drying [1]. The firing process transforms the raw clay into a chemically stable and durable material, which is why ceramics are so frequently found at archaeological sites and represent such a valuable source of information about past societies and technologies.

Glazes are thin glassy coatings applied to the ceramic surface before or after an initial firing and subsequently fused at high temperature. Their optical, mechanical, and chemical properties are governed by their elemental composition, the nature and distribution of crystalline phases, and the thermal history of the firing process [2] [3]. Beyond their practical function of making vessels impermeable to liquids, glazes served an important aesthetic and social role: through colour, shine, and decorative motifs, they transformed everyday objects into refined, sometimes luxury goods that circulated widely through trade networks [4] [5].The study of glaze composition and microstructure therefore offers a privileged window into the technical knowledge, raw material procurement strategies, and cultural exchanges of past communities.

This thesis investigates the glaze technology of Islamic-period ceramics recovered at Mértola [6], a historically significant urban site in southern Portugal that was under Islamic administration from the early 8th to the mid-13th century AD [7]. The central aim of the research is to characterize the opacified glazes of the Mértola assemblage — that is, glazes rendered white and non-transparent through the addition of specific mineral compounds — and to reconstruct the technology behind their production. Focus is placed on the identification of the opacifying agents employed, most notably tin oxide (SnO_2), which is a hallmark of Islamic glaze tradition [8]. However, the scarcity of tin in the Iberian Peninsula raises the question of whether alternative opacifying materials were locally available and exploited. This thesis proposes and investigates bone ash — a calcium phosphate-rich material readily accessible as a by-product of animal processing [9]— as a plausible alternative opacifier [10], a hypothesis that, to the best of the author's knowledge, has not been previously explored in the literature on Islamic glaze technology. To test the hypotheses emerging from the analysis of the archaeological material, a series of experimental replicas were produced under controlled laboratory conditions, with the aim of reconstructing and testing the original production technology [11].

The thesis is structured as follows. After an explanation over the research objectives and how to conquer them, Chapter 1" ***Historical background***" provides a brief historical overview of the Islamic period in the Iberian Peninsula and traces the origins and diffusion of glazed ceramic production within Al-Andalus. Chapter 2 "***Technology of Islamic ceramics*** "reviews the technical aspects of ceramic and glaze technology, covering raw material selection, preparation methods, firing procedures, and the use of colourants and opacifiers, with particular attention to the role of opacifying agents and their interaction with the ceramic body. Chapter 3 "M***aterials***" describes the samples investigated in this work, including both the archaeological assemblage from Mértola and the experimental replicas produced in the laboratory from controlled recipes. Chapter 4 "***Methods and analytical techniques***" describes the analytical methodology applied to both the archaeological samples and the experimental replicas. Chapter 5 "***Analytical results***" presents the results obtained from the archaeological assemblage, while Chapter 6 "***Discussions***" reports the outcomes of the experimental programme and discusses their implications for the reconstruction of the original production technology. A final chapter draws together the main conclusions and suggests directions for future research.

Research objectives

This work combines archaeological science and materials chemistry, with the goal of reconstructing the glazing technology used to produce Islamic "green and brown" glazed ceramics recovered at Mértola. To do this, both the chemical and microstructural characterization of archaeological samples and the production of experimental replicas in the laboratory were carried out.

More specifically, the research revolves around three main questions. First, what opacifying agents were used in the glazes of the Mértola assemblage? Tin oxide (SnO_2) is well documented as the standard opacifier in the Islamic glaze tradition [12] [13], but tin was located in the north of the Iberian Peninsula, meaning that probably, with time, local craftsmen lost the control of its source; this raises the question of whether something else was instead [14]. This thesis explores bone ash — a calcium phosphate-rich by-product of animal processing — as a possible alternative, a hypothesis that has not been previously explored in the literature.

The second question concerns the role of quartz in the decorated glaze surfaces. Building on recent work by Salinas and Pradell, this study looks at how quartz additions behave during firing: quartz [4] acts as a highly viscous melt that limits pigment spreading, allowing for finer and more controlled decorative detail. More specifically, the effect of varying the lead-to-silica molar ratio on the dissolution of quartz particles within the glaze matrix is examined. For reasons of time, in this work are presented the replicas with a white and transparent background.

The third question is broader: where do the Mértola ceramics fit within the wider polychrome glazed tradition of Al-Andalus and the Mediterranean [15]? The aim here is to understand whether what was found represents a local adaptation or something more connected to larger patterns of knowledge transfer.

Taken together, these objectives aim to contribute new knowledge to the understanding of Islamic glaze technology in the Iberian Peninsula, while also demonstrating the value of combining analytical archaeometry with experimental archaeology in the study of historical ceramic production.

To address all of this, both the ceramic bodies and the glazes were characterized in terms of chemical composition, microstructure, and mineralogical phase assemblage [16]. This allows for an assessment of the raw materials used, the processing and firing conditions applied, and any variations in craftsmanship that may reflect different chronologies, production centers, or technological transfers. A minimally invasive analytical approach was used throughout, following current best practices in archaeometric studies of cultural heritage materials: the analysis were carried out at the HERCULES

Laboratory of the University of Évora, Portugal. The experimental replica programme then translates these findings into practice: using historically plausible recipes, a series of glazes was produced in the laboratory to test the hypotheses emerging from the archaeological evidence — particularly around the use of bone ash and the behaviour of quartz in the glaze melt.

1. Historical Background

1.1 The Islamic Period in the Iberian Peninsula

The Islamic presence in the Iberian Peninsula began in 711 AD, when Umayyad forces crossed the Strait of Gibraltar and rapidly overwhelmed the Visigothic kingdom [17]. Within a few years, the greater part of the peninsula had come under Islamic control, becoming an Emirate of the Umayyad Caliphate of Damascus, and inaugurating a period of Muslim rule that would last, in varying forms, for nearly eight centuries. The conquered territory was designated al-Andalus, a political and cultural entity that became one of the most sophisticated civilisations of the medieval world.

The history of al-Andalus is conventionally divided into successive political phases. In 750 AD, the Abbasid revolution overthrew the Umayyad dynasty in Damascus, replacing it with a new caliphate centred in Baghdad. One of the few surviving members of the Umayyad royal family, the prince ʿAbd al-Raḥmān I, fled westward across North Africa and reached the Iberian Peninsula, where in 756 AD he seized power in Córdoba and founded an independent Umayyad emirate: The Emirate of Córdoba (756–929 AD) establishing the first autonomous Muslim state on Iberian soil [18]. This was followed by the Caliphate of Córdoba (929–1031 AD), a period of remarkable cultural and economic flourishing. The subsequent fragmentation into the Taifa kingdoms (1031–1086 AD) gave way to two successive North African dynasties — the Almoravids (1086–1147 AD) and the Almohads (1147–1238 AD) — before the final contraction of Islamic territory to the Emirate of Granada (1238–1492 AD).

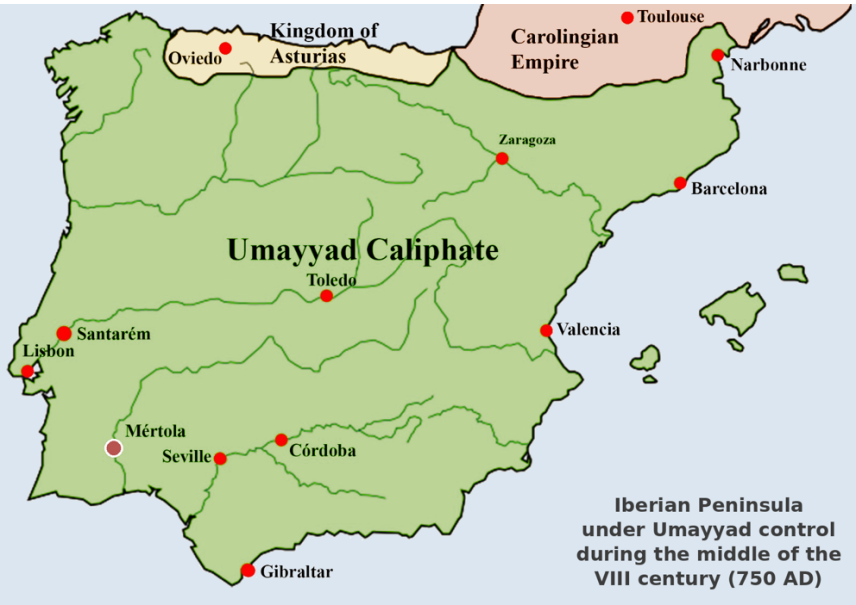


Figure 7 Map of the Iberian Peninsula under Umayyad control, c. 750 AD. The highlighted marker indicates the location of Mértola, the primary site examined in this study.

Throughout these phases, the population of al-Andalus was in constant contact with Christian kingdoms to the north, as well as with North Africa and the broader Mediterranean world. Communities arriving from North Africa and the eastern Mediterranean brought with them their culture, technical skills, and technological knowledge, leaving a lasting mark on Iberian material culture. This prolonged intercultural exchange contributed to the formation of the Hispano-Moorish (mudéjar) cultural identity and shaped the development of distinctive craft traditions — among which glazed ceramic production occupies a central place.

1.3 Origins of Glazed Ceramic Technology

The glazed ceramics examined in this thesis are the product of a long technological tradition predating the Islamic period in the Iberian Peninsula. The earliest evidence for Islamic glazed ceramic production comes from Egypt and Syria in the late 7th and 8th centuries AD, where potters developed opaque yellow and green glazed wares — known respectively as Coptic Glazed Ware and the Yellow Glazed Family [19] [20]. These early glazes were of the high-lead type and were opacified using lead stannate ($Pb(Sn,Si)O_3$), a technology inherited from Byzantine glassmakers who had continued the Roman tradition of using tin-based compounds as yellow opacifiers [21] [13].

The transition from yellow to white opacified glazes — the defining aesthetic of the Islamic ceramic tradition — took place in Abbasid Iraq during the 9th century AD, most probably at Basra. Compositional analyses have shown that, while the earlier Egyptian and Levantine yellow glazes were of the very high-lead type (typically >60 wt% PbO), the Mesopotamian white glazes shifted towards alkali-lead and alkali-dominant compositions, with PbO dropping to as low as 2–5 wt% and alkali content ($Na_2O + K_2O$) rising to 10–12 wt% [21] [22]. This new class of wares, known as Samarra-type pottery after the Iraqi city where early examples were securely dated, used tin oxide (SnO_2) dispersed in an alkali glaze to produce a dense, opaque white surface inspired by imported Chinese stoneware and porcelain [23] [15]. Replication experiments have demonstrated that the technological link between the two traditions was direct: mixing a lead-tin calx (Pb/Sn > 3) with silica and alkalis and firing above 750 °C caused the dissolution of lead-tin-oxide particles and the precipitation of tin oxide crystals, yielding a white opaque frit [22]. The white tin-opacified ground thus obtained provided the ideal canvas for the cobalt-blue painted and lustre decorations that became hallmarks of Abbasid ceramic production.

The common assumption that Islamic glazed ceramics emerged primarily in response to Chinese imports has been critically reassessed: as Watson (2014) [22] has argued, the Chinese ceramics recovered from the Belitung Shipwreck more plausibly reflect commissions placed by Middle Eastern importers targeting a market already supplied by locally produced glazed wares.

From Mesopotamia, the white tin-opacified glaze tradition spread westward across the Islamic world along established trade and pilgrimage routes. It reached North Africa — first Ifriqiya (present-day Tunisia) and subsequently the Maghreb — during the 9th and 10th centuries, transmitted through the movement of finished goods. Through the contact with Ifriqiyan and Maghrebi production centers, the innovative technology was introduced into the Iberian Peninsula, where it would be further developed and adapted over the following centuries.

1.4 Introduction of Glaze Technology in al-Andalus

The introduction of glazing in al-Andalus was not a single event but occurred through successive "technological waves" influenced by Oriental traditions [24]. Two distinct glazing technologies were established [4], [26]. The first was the production of high-lead silica glazes, introduced around the mid-9th century during the Emiral period, with the earliest known centres at Pechina (Almería) and Córdoba [14]. Recent evidence also suggests that lead ore was already being exploited for glass production from the early Emirate onwards [27]. The second technology — the introduction of alkali metal oxides (Na_2O, K_2O) combined with tin oxide (SnO_2) to produce lead-alkali tin-opacified white glazes — followed shortly after, by the end of the Emiral period or the beginning of the Caliphate in the 9th–10th centuries [28], [3].

The diffusion of these technologies across al-Andalus was gradual, radiating outward from the productive heartland of southern Iberia toward peripheral regions such as the Gharb al-Andalus. It is within this context that the glazed ceramics of Mértola must be understood — as products of an established Islamic tradition, precursor to the European majolica tradition, adapted to local conditions, and potentially incorporating technical solutions that reflect the specific material constraints of the western periphery of al-Andalus.

2. Technology of Islamic Ceramics

2.1 The Ceramic Body

The behaviour of a ceramic body during firing follows two distinct trajectories depending on its chemical composition, and specifically on whether the clay is rich in calcium or in silica [29] [30]. Calcareous clays — that is, raw materials containing a significant proportion of calcium carbonate (typically 15–25 wt% CaO) — were the most common choice for tin-opacified glazed wares across the Islamic world, including the Iberian Peninsula, because the calcium component inhibits the crystallisation of hematite (Fe_2O_3) during firing, yielding a characteristic buff or cream-coloured surface that does not interfere with the colour of the overlying glaze. However, non-calcareous, silica-rich clays (with CaO as low as 2–3 wt%) were also employed, particularly when a transparent lead glaze — whose colour depends in part on the underlying body — was applied directly onto the surface without the need for an opaque white background. In either case, the raw clay mixture comprises fine-grained phyllosilicate minerals — principally illite, kaolinite, and smectite — combined with non-plastic temper additives such as quartz, feldspar, and calcite, which improve workability and reduce shrinkage during drying.

During firing, the ceramic body undergoes a series of progressive mineralogical transformations. The first is dehydroxylation — the loss of structurally bound water from the clay minerals — which occurs between approximately 450 and 600 °C. This is followed by the decomposition of carbonates at around 700–850 °C, releasing CO_2, and by the onset of vitrification at higher temperatures. The nature of the high-temperature mineral phases that subsequently nucleate and grow depends critically on the body composition. In calcareous clays, the calcium released by carbonate decomposition reacts with the silicate matrix to form phases such as wollastonite ($CaSiO_3$), diopside ($CaMgSi_2O_6$), gehlenite ($Ca_2Al_2SiO_7$), and anorthite ($CaAl_2Si_2O_8$). In silica-rich, non-calcareous clays, by contrast, the dominant neoformed phase is mullite ($3Al_2O_3 \cdot 2SiO_2$), alongside cristobalite at higher temperatures. These newly formed crystalline phases confer mechanical strength and chemical stability to the fired product — which is precisely why ceramics survive so well in the archaeological record and can retain compositional information about raw materials and production conditions for centuries.

The typical firing temperatures for Islamic glazed ceramics from al-Andalus ranged between approximately 850 and 1000 °C, achieved in updraft kilns fuelled by wood or other biomass, under predominantly oxidising atmospheric conditions. The phase equilibrium diagram for the $PbO–SiO_2$ system shows that a eutectic melt forms at 717 °C at a composition of approximately 70 wt% PbO

and 30 wt% SiO_2 [31], meaning that the glaze would begin to melt and interact with the ceramic body well before the body itself reached its maximum firing temperature.

2.2 Glazes: Definition and Structure

A ceramic glaze is a thin glassy layer fused onto the surface of a ceramic body through firing. Unlike a glass object, a glaze is an open system: its composition evolves during the firing process as a result of interdiffusion of elements between the molten glaze and the underlying ceramic body, and of the volatilisation of some of its constituents [32]. On a structural level, glazes are predominantly amorphous — that is, lacking a regular long-range crystalline atomic arrangement — and can be described as silicate glasses whose properties are determined by elemental composition, the nature and distribution of any residual crystalline or undissolved phases, and the thermal history of the firing process.

The glassy matrix is built around a silicate network (SiO_2), the principal network former, whose continuous three-dimensional structure of $(SiO_4)^{4-}$ tetrahedral units is disrupted by the addition of network-modifying oxides that lower its melting temperature and viscosity. In the Islamic ceramic tradition, two major glaze families can be distinguished on the basis of their fluxing system. The first is the high-lead type, in which PbO (typically 45–60 wt%) serves as the primary flux, reacting with silica and producing a transparent, optically brilliant surface. The second is the lead-alkali type, in which a proportion of the lead is replaced by alkali metal oxides (Na_2O, K_2O), typically reaching 5–12 wt% alkali alongside 20–40 wt% PbO. This second composition was essential for the production of opaque white glazes: alkalis facilitate the dissolution of lead stannate and the subsequent recrystallisation of tin oxide (SnO_2) particles, producing dense white opacity rather than the yellow colour obtained in purely high-lead glazes [33]. Al_2O_3 acts as an intermediate oxide, entering the silicate network in tetrahedral coordination and stabilising the glass structure. Transition metal oxides — FeO, CuO, CoO, MnO — serve as colourants and are discussed in Section 2.6. The physical compatibility between glaze and body, and the consequences of their chemical interaction during firing, are addressed in Section 2.4.

2.3 Raw Materials and Frit Preparation

Islamic glazes from Iberian Peninsula are generally classified as lead-alkali glazes [16], meaning that their glassy matrix is based on a combination of lead oxide (PbO), as the primary flux, silica (SiO_2) as the network former, and alkali metal oxides (Na_2O, K_2O) as secondary fluxes. Lead was valued for his ability to significantly lower the melting temperature of the glaze, producing a fluid melt at kiln temperatures achievable with the technology of the time [9], while also conferring a characteristic

brilliance to the finished surface. The primary source of lead was galena ore (PbS[35], extracted from deposits in the southeast of the Iberian Peninsula and processed by roasting to produce lead oxide before incorporation into the glaze mixture. Silica was typically introduced in the form of quartz sand or crushed quartz, while alkali fluxes were sourced from plant ash — principally the ash of halophytic plants rich in sodium, or wood ash rich in potassium — or from naturally occurring natron deposits [36]. The use of plant ash in al-Andalus is attested both by the chemical signatures (elevated MgO, K_2O, and P_2O_5) found in lead-alkali glazes and by comparison with the raw materials described in the 14th-century treatise of Abu'l-Qasim of Kashan [37].

The glaze was not applied as simple powder mixture of raw materials. Rather, the raw ingredients were first pre-melted and quenched to form a glassy mass know as *frit*, which was then ground into a fine powder and suspended in water for application to the ceramic surface. This step was needed to make the raw materials soluble and chemically inert and safer to handle —especially the potentially toxic components as the lead compounds— while also providing a more homogeneous glaze composition. A small quantity of clay or organic binder such as gum Arabic was sometimes added to the suspension to improve its viscosity and adhesion to the ceramic surface before firing. The use of frits rather than raw lead ore applied directly to the body surface has been consistently demonstrated archaeometrically in Islamic Iberian production from the earliest known centers at Pechina and Córdoba onwards.

2.4 Ceramic body and the Glaze Interaction

The dominant practice in Islamic Iberian ceramic production was double firing: the body was first biscuit-fired, then the powdered frit suspension was applied and the piece was fired again to melt and fuse the glaze. This ensured that defects could be identified before glazing, that CO_2 from carbonate decomposition had already been released, and that the higher open porosity of the biscuit allowed rapid, predictable absorption of the glaze suspension[30].

During the glaze firing, elements such as Al_2O_3, CaO, FeO, K_2O, and MgO diffuse from the body into the glaze, while PbO diffuses in the opposite direction. This generates composition gradients and promotes precipitation of crystalline compounds at the interface: lead-potassium feldspars ($(K,Pb)AlSi_3O_8$) on non-calcareous bodies, wollastonite ($CaSiO_3$) and pyroxenes ($(Ca,Mg,Fe)_2Si_2O_6$) on calcareous bodies. In double-fired ceramics the interface is thin (≤30 μm), with acicular crystallites at the boundary; single firing produces thicker, more diffuse interfaces. A significant fraction of the Al_2O_3 and FeO_3 (2–7 wt% in transparent high-lead glazes, 0.5–3 wt% in tin-opacified lead-alkali glazes) in the finished glaze derives from this diffusion rather than from deliberate additions to the glaze mixture.

Compatibility between glaze and body during cooling below the glass transition temperature (~500 °C) is governed by their respective thermal expansion coefficients. If the glaze contracts more than the body, tensile stresses cause *crazing* — fine surface cracks (Figure 8). If it contracts significantly less, compressive stresses cause *shivering* (flaking of the glaze) or *shattering* (cracking of the body). High-lead glazes (5–7 × 10^{-6}/°C) match well with both non-calcareous (3–5 × 10^{-6}/°C) and calcareous (5–7 × 10^{-6}/°C) clay bodies; lead-alkali glazes (7–9 × 10^{-6}/°C) pair best with calcareous clays; pure alkali glazes (9–10 × 10^{-6}/°C) are highly prone to crazing on earthenware. *Crawling* — the retraction of molten glaze to leave exposed biscuit — relates to surface tension: high-lead glazes (~230 mJ/m²) wet the body better than alkali glazes (~280 mJ/m²) and are less susceptible. Lead-alkali formulations offered a practical compromise, reducing crawling risk while also lowering the danger of PbO reduction to metallic lead (causing blackening) that affects very high-lead glazes under insufficiently oxidising conditions.



Figure 8. example of crazing

2.5 Opacifiers: Tin Oxide, Bone Ash, and Quartz

Opacification is achieved by dispersing sub-micrometre crystalline particles within the glassy matrix, whose refractive index differs sufficiently from the surrounding glass to scatter light efficiently [38]. Tin-based opacification first appeared in 8th-century Egypt and Syria as lead stannate ($Pb(Sn,Si)O_3$) in high-lead yellow glazes [6]. High-temperature XRD studies have shown that increasing the silica content and adding alkalis lowers the temperature at which lead stannate dissolves and recrystallises as cassiterite (SnO_2) — which produces white opacity—, from ~1030 °C to as low as 750 °C. Replication experiments confirmed that plant ash further facilitates this transition. The resulting cassiterite particles — sub-micrometre and smaller than unreacted particles from the original calx — produce the dense white opacity of Abbasid and later Islamic wares.

In al-Andalus, tin oxide became the dominant opacifier from the late 9th–early 10th century [39]. However, tin is not locally abundant in most of Iberia, raising the question of whether alternative agents were used in peripheral centres such as the Gharb al-Andalus. One candidate is bone ash — predominantly hydroxyapatite ($Ca_{10}(PO_4)_6(OH)_2$) — well attested as an opacifier in Byzantine glass tesserae from the 5th–6th century onward [40]. Experimental replicas have shown that bone must be pre-fired to ~800 °C, mixed with base glass, and heated at ~700 °C for 18–36 hours to produce the characteristic microstructure of hydroxyapatite cores with β-rhenanite rims and neoformed wollastonite. Whether Islamic potters in western Iberia adapted this technique is a central hypothesis of this thesis.

Quartz is also relevant: coarse particles added to a lead-rich frit dissolve only partially during firing, creating zones of high viscosity that scatter light and limit pigment diffusion, enabling finer polychrome decorations. The rate of dissolution depends on the PbO/SiO_2 ratio, firing temperature, and duration — parameters explored in the experimental programme of Chapter 3.

2.6 Colourants and Decoration

The white opacified glaze surface provided an ideal substrate for polychrome decoration, applied using metal oxide-based pigments prior to the glaze firing. The principal colourants used in Islamic al-Andalus ceramics include cobalt oxide (CoO) for blue, copper oxide (CuO) for green, manganese oxide (MnO_2) for brown and black, and iron oxide (Fe_2O_3) for ocher and red tones. These pigments were either applied directly onto the unfired glaze surface, or mixed with a small quantity of frit to improve adhesion, depending on the specific decorative technique employed [41].

The range of decorative styles documented in Islamic Iberian ceramics — from simple monochrome finishes to elaborate polychrome geometric and vegetal motifs — reflects both the technical sophistication of the craftsmen and the evolving aesthetic preferences of successive dynastic periods. The characterisation of both opacifiers and colourants in the Mértola assemblage therefore provides information not only on production technology, but also on the broader cultural and commercial networks within which these objects were made and consumed.

3. Materials

This chapter presents the materials and the methodological framework supporting the present study, comprising a total of three archaeological reference specimens and fifteen experimental replicas. The first section introduces the archaeological assemblage recovered from the medieval Islamic site of Mértola, establishing the compositional and optical baseline for the historical glazed ceramics. The subsequent section details the design and production of the experimental replicas, encompassing the evaluation of the ceramic body, the preparation of bone ash as an opacifying agent, and the thermodynamic principles governing the formulation of the lead-silicate glaze recipes. By bridging the analysis of historical artifacts with controlled laboratory reproductions, this comparative approach aims to elucidate the specific technological choices and physical properties characteristic of the original ceramics.

3.1. Archaeological samples: Mértola and the Gharb al-Andalus

Within this broader historical framework, the site of Mértola occupies a position of relevance to the present study. Located on the banks of the Guadiana River in southern Portugal, Mértola functioned as one of the most important river ports of the Gharb al-Andalus — the westernmost frontier region of al-Andalus, roughly corresponding to present-day Portugal — throughout the Islamic period (8th–13th centuries AD). Its strategic position along a navigable river connecting the interior to the Atlantic coast made it a significant node in regional trade networks, and the ceramic assemblage recovered from the site reflects not only local production practices, but also the wider circulation of goods and technological knowledge across the Islamic western Mediterranean (Figure 9).



Figure 9. Panoramic view of the town of Mértola and the Guadiana River, southern Portugal, illustrating its strategic position as a primary river port.

The three archaeological samples selected for this study — excavated from the medieval Islamic layers of Mértola and catalogued as crvm623, crvm666, and crvm1668 (Figure 10)— belong precisely to this assemblage, and serve as the primary analytical reference for glaze and body compositions. All three are opacified and decorated glazed calcareous ceramics whose white background colour cannot be fully accounted for by tin oxide content alone [42], a discrepancy that motivates the central hypothesis of this work. They therefore function as the analytical comparanda against which the experimental replicas are evaluated: the aim being to reproduce, in a controlled laboratory setting, the glaze chemistry and optical behaviour observed in the archaeological material.

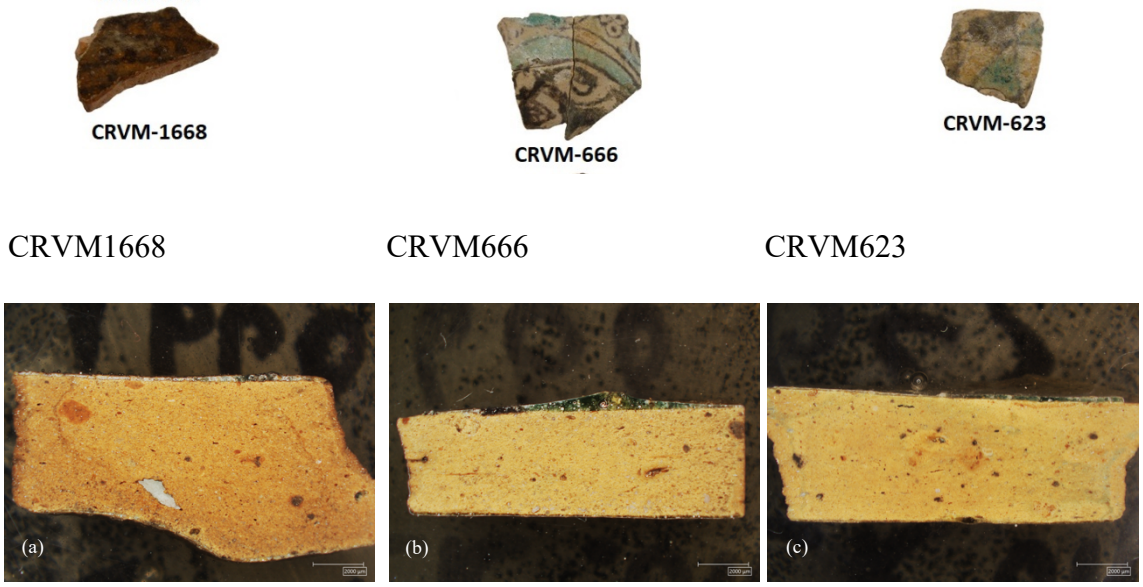


Figure 10. Photographs and Digital microscopy images of archaeological samples:(a) crvm1668, (b) crvm666, (c)crvm623, at 20× magnificaton

3.2 Experimental Replicas

The experimental program was designed to systematically investigate the interaction between lead-silicate glazes and calcareous substrates. The ceramic body selected for the replicas consists of a calcareous clay pre-fired at 950 °C, specifically chosen to replicate the mineralogical and thermal characteristics of the archaeological samples from Mértola. This ensures a consistent baseline for evaluating glaze-body compatibility, thermal expansion matching, and the development of the interfacial layer during the subsequent firing stages.

Bone ash from raw bovine cortical bone (Figure 11) was used as the key glaze additive for this study. In the context of glaze technology, bone ash is of interest as a potential opacifying agent: the refractive index of hydroxyapatite (~1.64) differs from that of a lead-silicate glass matrix (~1.9–2.1) sufficiently

to generate light scattering at the particle–glass interface, and the material would have been locally and cheaply available as a by-product of butchery and food processing in any medieval urban context.



Figure 12. Photographs of raw bone

3.2.1 Design and Formulation of the Experimental Glaze Recipes

The PbO–SiO_2 binary phase diagram: theoretical framework

The formulation of the experimental glaze recipes was based on the thermodynamic principles governing the the binary phase diagram of PbO–SiO_2 system. In the lead-silicate glazes, PbO serves as a powerful flux that drastically lowers the melting temperature of silica (which would be around 1600°C). However, the extent to which free quartz dissolves into the lead-rich melt depends critically on the molar ratio of PbO to SiO_2 : if this ratio falls outside the appropriate range for a given firing temperature, residual undissolved quartz grains would persist in the glaze, producing an inhomogeneous, rough, and optically poor surface. PbO–SiO_2 phase diagram provides the liquidus curve that defines, for each composition, the minimum temperature at which the melt becomes fully liquid and all cristalline silica is dissolved.

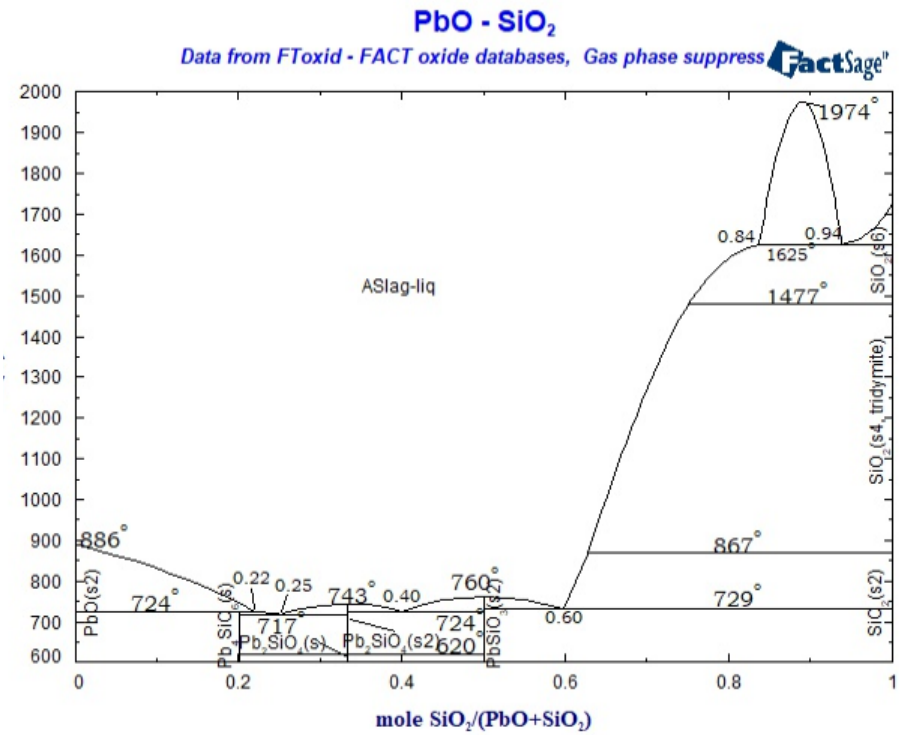


Figure 13 PbO-SiO_2 phase diagram highlighting equilibrium cristobalite (Pb_2SiO_4 at ~724°C) and liquidus (~1477°C) for glaze compositions (0.22–0.60 SiO_2 mole fraction). Firing at 959–1100°C drives partial crystallization, with bone ash influencing Ca-Si-P phases

The key parameter extracted from this diagram for recipe formulation is the **molar ratio**, defined here as:

$$\textit{Molar ratio} = \textit{mol } SiO_2 \textit{ / (mol } SiO_2 \textit{ + mol PbO)}$$

This ratio expresses the proportion of SiO_2 molecules relative to the total number of network-forming and flux molecules. It is equivalent to the mole fraction of SiO_2 in the binary PbO–SiO_2 system, which is precisely the quantity plotted on the x-axis of the phase diagram. By reading the diagram, one can determine the temperature range within which a given molar ratio will produce a fully molten, homogeneous glaze. The experimental recipes were designed so that each one corresponds to a different molar ratio, covering an interval from 0.55 to approximately 0.78, thereby spanning the region of the phase diagram from just above the eutectic (low liquidus, easy to melt) to well into the cristobalite field (high liquidus, more refractory).

From diagram to recipe: the calculation procedure

The starting point for each recipe is a *target molar ratio* chosen from the phase diagram. The challenge is then to translate this molar ratio back into a practical recipe — that is, into the weight percentages (wt%) of raw materials that must be weighed on a balance.

The raw materials used in this work and their oxide compositions are listed in Table 1. For each recipe, the theoretical composition in terms of individual oxides is calculated as follows: the weight percentage of each oxide X in the final batch is obtained by summing the contributions from all raw materials

$$wt\%\ of\ oxide\ X = \Sigma_i\ [(wt\%\ of\ X\ in\ raw\ material_i) / 100 \times (wt\%\ of\ raw\ material_i\ in\ the\ recipe)]$$

Each recipe proportions were therefore selected specifically so that the corresponding resulting molar ratio equals to the theoretical chosen one. The procedure followed the path of adjusting the proportion of frit and additional silica until the target molar ratio was reached. Table 2 summarises the calculated oxide compositions, and Table 3 summarises all the molar ratios.

Oxide	LT599 frit	Bone Ash	SnO^2	SiO^2
Na_2O	0.00	1.31	0.00	0.00
MgO	0.00	1.28	0.00	0.00
Al_2O_3	0.00	0.45	0.00	0.00
SiO_2	25.00	0.17	0.00	100.00
K_2O	0.00	0.00	0.00	0.00
CaO	0.00	51.67	0.00	0.00
PbO	75.00	0.00	0.00	0.00
SnO_2	0.00	0.00	100.00	0.00
P_2O_5	0.00	42.88	0.00	0.00

Table 1.Oxide composition (wt%) of the four raw materials used in this study. Only the principal oxides are listed; trace components and volatiles (CO2 from bone ash) are omitted for clarity.

	LT599	Red (R)	Purple (P)	Blue (B)	Yellow (Y)
Frit (wt%)	100.0	92.5	62.5	82.5	88.5
Bone Ash (wt%)	—	5.0	5.0	5.0	0.0
SnO^2 (wt%)	—	2.5	2.5	2.5	2.5
SiO^2 added (wt%)	—	0.0	30.0	10.0	9.0
Resulting oxide composition (wt%)					
PbO	75.00	69.38	46.88	61.88	66.38
SiO_2	25.00	23.13	45.63	30.63	31.13
CaO	0.00	2.58	2.58	2.58	0.00
P_2O_5	0.00	2.14	2.14	2.14	0.00
SnO_2	0.00	2.50	2.50	2.50	2.50
Molar ratio	**0.553**	**0.553**	**0.783**	**0.648**	**0.635**

Table 2. Top: weight percentages of raw materials for each recipe. Bottom: resulting theoretical oxide composition and molar ratio [mol SiO^2 / (mol SiO^2 + mol PbO)]. LT599 = pure frit (transparent lead glaze baseline). R, P, B contain bone ash; Y does not. Dash (—) = not added.

Recipe	PbO (wt%)	SiO^2 (wt%)	mol PbO	mol SiO^2	Molar ratio
LT599	75.00	25.00	0.3360	0.4161	**0.553**
Red (R)	69.38	23.13	0.3108	0.3850	**0.553**
Purple (P)	46.88	45.63	0.2100	0.7596	**0.783**
Blue (B)	61.88	30.63	0.2772	0.5099	**0.648**
Yellow (Y)	66.38	31.13	0.2974	0.5181	**0.635**

Table 3. Detailed molar ratio calculation: PbO and SiO^2 total weight percentages from Table 2, converted to moles using Mw(PbO) = 223.19 g/mol, Mw(SiO^2) = 60.08 g/mol. Note that Red and LT599 share the same molar ratio because the added bone ash and SnO^2 do not contribute PbO or SiO^2.

A result that emerges immediately from Table 3 deserves explicit discussion: the pure frit LT599 and the Red recipe share the same molar ratio (0.553), a necessary consequence of the recipe design. The Red recipe was formulated by replacing 7.5 wt% of the frit with bone ash (5 wt%) and SnO_2 (2.5 wt%). Neither bone ash nor tin oxide contributes any significant amount of PbO or SiO_2 to the batch (the SiO_2 content of bone ash is only 0.17 wt%, negligible). Therefore, the PbO:SiO_2 molar equilibrium of the melt is preserved identically to that of the pure frit. This makes Red the ideal paired comparison for LT599: any difference observed between these two samples — in microstructure, opacity, crystal morphology, glaze–body interaction — can be attributed exclusively to the effect of bone ash and tin oxide, with no confounding change in the fundamental glass-forming equilibrium.

Furthermore, this observation reveals the logic behind the choice of the frit composition itself. The 75:25 wt% PbO:SiO_2 ratio of LT599 was not arbitrary: it corresponds to a molar ratio of 0.553, which places the composition on the SiO_2-rich side of the eutectic in the PbO–SiO_2 phase diagram, where the liquidus temperature is only ~750–800 °C. This means that even at the lowest firing temperatures documented for Islamic Iberian productions (~850 °C), a frit with this composition would be fully molten, with all silica dissolved and a homogeneous glassy melt formed. Archaeometric analyses of pre-13th-century Islamic frits from al-Andalus have consistently reported PbO:SiO_2 weight ratios clustering precisely in this range (approximately 70–80 wt% PbO, 20–30 wt% SiO_2), confirming that medieval potters arrived empirically at a composition that sits in the thermodynamically optimal region for low-temperature, easily fusible lead glazes [30], [43]. The LT599 frit thus replicates this historically attested composition, and 0.553 serves as the *lower bound* of the molar ratio range explored in this study, representing the easiest-to-melt baseline from which the other recipes progressively depart by adding increasing amounts of free silica.

Interpretation: what each molar ratio means on the phase diagram

The five recipes span a wide range of the PbO–SiO_2 phase diagram, from the PbO-rich side near the eutectic to deep in the cristobalite primary field. Reading the liquidus curve:

LT599 and Red (molar ratio ≈ 0.55) — as discussed above, these two compositions are thermodynamically equivalent in terms of the PbO–SiO_2 equilibrium. They fall near the SiO_2-rich side of the eutectic, where the liquidus is approximately 750–800 °C. At any firing temperature above ~800 °C, these compositions should be completely molten, producing a smooth, homogeneous glaze.

Yellow and Blue (molar ratio ≈ 0.64) are shifted into the cristobalite primary field. The liquidus rises to approximately 850–900 °C. At 900 °C, these compositions should be close to or just above their liquidus, producing a well-formed glaze. At 800 °C, some residual silica may persist.

Purple (molar ratio ≈ 0.78) lies far into the cristobalite field, where the liquidus is estimated at approximately 1000–1050 °C. This composition is the most refractory of the set: at 900 °C, the melt will very likely contain undissolved cristobalite or quartz grains, producing a visibly rough and opaque surface. This recipe was intentionally designed as an extreme case, to observe the consequences of an excessively high SiO_2 molar ratio.

It should be noted that the PbO–SiO_2 binary phase diagram provides a first approximation. The actual glaze systems are more complex because they include minor oxides (CaO, P_2O_5, SnO_2) which can modify the liquidus. CaO from bone ash raises the viscosity and may slightly raise the melting point; P_2O_5 can promote liquid–liquid immiscibility. SnO_2 is moderately soluble in lead glass and reprecipitates as cassiterite crystals on cooling, producing the opacifying effect [44]. Nevertheless, since PbO and SiO_2 together constitute more than 90 wt% of all compositions (see Table 2), the binary phase diagram is a reliable guide for predicting the melting behaviour.

Firing protocol: three temperatures to reconstruct the sequence of glaze formation

Each of the five glaze batches was weighed for a total of 7.5 g (Table 4), ground, and suspended in water to form a suspension. Each suspension was applied to three separate ceramic tiles that had been previously biscuit-fired at 950 °C, ensuring a fully sintered and mineralogically stable substrate. The three coated tiles were then fired at three distinct peak temperatures: **700, 800, and 900 °C**.

This choice of temperatures is directly linked to the phase diagram:

At 700 °C, the system is below the eutectic temperature (~725 °C) of the PbO–SiO_2 binary. At this temperature, the glaze batch has barely begun to soften: individual grains of frit, silica, bone ash, and tin oxide are still largely unreacted. Only localised, incipient sintering or partial surface reactions may occur. This temperature serves as the "pre-melting" reference point, capturing the raw state of the glaze mixture just before significant liquid forms.

At 800 °C, the PbO-rich recipes (LT599, Red) are above their liquidus and should form a homogeneous melt. The intermediate recipes (Yellow, Blue) are near their liquidus — some residual silica may still be dissolving. The Purple recipe, with its high molar ratio, is far below its liquidus and will contain abundant undissolved quartz in a partially formed melt. This temperature captures the critical "mid-melting" stage, where composition-dependent differences become most visible.

At 900 °C, most recipes (except Purple) should be well above their liquidus. The melt is fully developed, viscosity is low enough for the glaze to spread and wet the substrate, and the chemical interaction between glaze and ceramic body (diffusion of Al, Ca, Si from the body into the melt) reaches its maximum extent. Tin oxide dissolution and reprecipitation is most complete, and the bone-ash-derived phosphate phases are expected to develop their characteristic microstructural signatures. Only Purple, whose liquidus lies at ~1000–1050 °C, will still show clear evidence of incomplete melting.

By examining the same composition at these three temperatures, it is possible to reconstruct the *sequence of physical and chemical events* that occur during glaze firing: the onset of melting, the progressive dissolution of free silica, the redistribution of the tin oxide opacifier, the development of the glaze–body interface, and the formation of new crystalline phases. Each temperature provides a "frozen snapshot" of the glaze at a different stage of maturation. Crucially, this approach also allows the estimation of the original firing temperature of the archaeological glazes by comparing their microstructure with that of the replicas fired at known temperatures — a methodology demonstrated in experimental studies on Islamic and Hispano-Moresque glazed ceramics [45] [32] [46].

The complete experimental matrix is summarised in Table 5: five recipes × three firing temperatures = 15 individual samples.

Component	LT599 (g)	R (g)	P (g)	B (g)	Y (g)
Frit LT599	7.500	6.938	4.688	6.188	6.638
Bone Ash	—	0.375	0.375	0.375	—
SnO_2	—	0.188	0.188	0.188	0.188
SiO_2	—	—	2.250	0.750	0.675
Total	**7.500**	**7.500**	**7.500**	**7.500**	**7.500**

Table 4. Weighed amounts of each raw material for a total batch mass of 7.5 g per recipe. Each batch was suspended in water for application to the ceramic tiles. A dash (—) indicates the component was not included.

Recipe	Molar ratio	700 °C	800 °C	900 °C	Bone Ash
LT599	0.553	✓	✓	✓	No
Red (R)	0.553	✓	✓	✓	Yes

Yellow (Y)	0.635	✓	✓	✓	No
Blue (B)	0.648	✓	✓	✓	Yes
Purple (P)	0.783	✓	✓	✓	Yes

Table 5. Complete experimental matrix: 5 glaze compositions × 3 firing temperatures = 15 individual samples. Recipes are ordered by increasing molar ratio. All tiles were biscuit-fired at 950 °C prior to glaze application.

4. Methods and analytical techniques

4.1. Sampling and sample preparation

After boiling the bone in water and $NaHCO_3$ to remove the residual meat and excess of fat, bone ash was prepared by calcination at 1000°C in two stages: an initial 30-minute firing followed by a two-hour hold at temperature, with a further two-hour cooling phase inside the furnace. This protocol ensures the complete combustion of organic matter (collagen and residual lipids) and the conversion of biogenic hydroxyapatite into a phase-pure, thermally stable calcium phosphate, as confirmed by the TGA data described in section *5.1.3.* The calcined material was then ground in an agate mortar to a fine white powder before incorporation into the glaze batches [14].

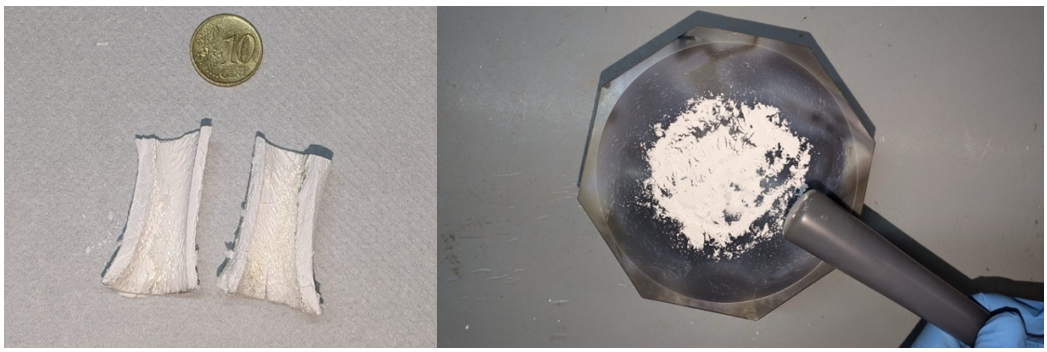


Figure 14. Bone ash preparation images

The development of the experimental replica programme proceeded through a series of iterative cycles, each designed to progressively refine both the glaze composition and the ceramic body conditions until a set of samples chemically and visually comparable to the Mertola archaeological material was achieved. Practically, each glaze mixture was suspended in 5 ml of distilled water and applied to ceramic tiles (previously biscuit-fired at 950°C), followed by firing at 700, 800, or 900°C. For microstructural characterization, cross-sections of the fired tiles were cut, embedded in epoxy resin, and polished to a mirror finish to allow for high-resolution SEM-EDS analysis.



Figure 15. set of replicas

4.2. Analytical techniques

4.2.1. Digital Optical Microscopy (DOM)

Digital Optical microscopy was employed to characterize the microstructure of the ceramic body and its interface with the glaze. Observations were performed on polished cross-sections using a Hirox optical microscope, under both plane-polarized light (PPL) and cross-polarized light (XPL), enabling discrimination between amorphous and crystalline phases, identification of inclusions, and assessment of the vitrification degree of the clay matrix.

For the original samples, the analysis documented the organization of the clay matrix, the nature and distribution of temper, porosity, and the morphology of the body–glaze interface, with particular attention to reaction layers and diffusion fronts. For the experimental replicas, the technique allowed evaluation of the white opacifier distribution, detection of air bubbles or undesired interposed phases, and assessment of glaze homogeneity in cross-section. Detailed specifications for each sample are reported in the Supplementary Materials associated with this work.

4.2.2 X-ray Powder Diffraction (XRPD)

X-ray powder diffraction (XRPD) identifies crystalline phases by exploiting the periodic atomic structure of minerals: when a monochromatic X-ray beam strikes a powdered sample, each crystalline phase diffracts at angles governed by Bragg's law ($n\lambda = 2d \sin \theta$), producing a characteristic set of peaks at defined 2θ positions that function as a phase-specific fingerprint. Amorphous material contributes only a broad background signal, so the relative proportion of crystalline to amorphous content is also visible in the profile shape. In ceramic archaeometry, XRPD is the primary tool for reconstructing the thermal history of a body, as the decomposition of clay minerals and the sequential crystallisation of high-temperature neogenic phases — gehlenite, anorthite, diopside — are strongly temperature-dependent.

Analyses were performed in standard Bragg–Brentano (macro) geometry on a Bruker D8 Advance diffractometer equipped with a Cu Kα radiation source (λ = 1.5406 Å), operating at 40 kV and 40 mA, with a LynxEye position-sensitive detector. Patterns were collected in the 5–65° 2θ range with a step size of 0.02° and a counting time of 1 s/step. Phase identification was carried out using Diffrac.EVA software with the ICDD PDF-2 mineralogical database. Each sample was ground to a fine powder prior to analysis and backloaded into the sample holder to minimise preferred orientation effects.

4.2.3 Scanning Electron Microscopy with Energy Dispersive Spectroscopy (SEM-EDS)

Scanning electron microscopy focuses a nanometre-scale electron beam across the sample surface in a raster pattern, generating several simultaneous signals. Backscattered electrons (BSE), whose yield is proportional to the mean atomic number of the material, produce compositional contrast images in which heavy-element-rich phases appear bright against a darker matrix- directly useful for distinguishing the Pb-rich glaze from the ceramic body and for locating high-*Z* opacifier particles. Secondary electrons (SE) provide surface morphological imaging. The energy-dispersive spectrometer attached to the column collects the characteristic X-rays emitted when primary electrons eject inner-shell electrons from sample atoms; the energy of each photon identifies the emitting element, and their intensities — after matrix correction — yield quantitative elemental concentrations.

Analyses were performed Hitachi S-3700N variable-pressure SEM equipped with a Bruker Nano XFlash 630 silicon drift detector (spectral resolution 129 eV at Mn Kα), operated at 20 kV accelerating voltage and a current of 120 microA, to generate sufficient overvoltage for the Pb M-series lines (~2.3 keV) and heavier L-lines. Resin inglobated polished blocks were analysed by BSEM-EDS using a HITACHI S3700N interfaced with a Quanta EDS microanalysis system. The Quanta system was equipped with a Bruker AXS XFlash® Silicon Drift Detector (129 eV Spectral Resolution at FWHM/MnKα). Standardless pHIROZ quantitative elemental analysis method was performed using the Bruker ESPRIT software. The operating conditions for EDS analysis were as follows: BSEM mode (BSEM), 20 kV accelerating voltage, 10 mm workingdistance, and 120μA emission current.The detection limits for major elements (Na) were in the order of 0.1 wt.%. Oxygen was excluded from direct quantification due to its low fluorescence yield and strong absorption of O Kα X-rays (0.525 keV) by the detector window; compositions are therefore reported as oxide weight percentages with stoichiometric oxygen recalculated from cation valences after normalisation to 100 wt.%. Quantification was performed using ZAF matrix correction. System stability was routinelly checked with the analysis of differenbt glass standard. Quantitative accuracy on was determined for the following oxides: Na_2O, MgO, Al_2O_3, SiO_2, P_2O_5, K_2O, CaO, Fe_2O_3, PbO, TiO_2, SnO_2, MnO, CuO and it was validated against standard reference materials (CMOG B D sgt8), yielding an accuracy within ±5% of the certified values.

4.2.4 Raman Spectroscopy

Raman spectroscopy probes the vibrational modes of chemical bonds by measuring the inelastic scattering of laser photons by the sample. When a photon interacts with a molecular bond, a small fraction

of the scattered light emerges at a different energy: the shift between incident and scattered photon energies — the Raman shift, expressed in cm^{-1} — corresponds to the energy of a specific bond vibration. Because different molecular groups and crystal structures have distinct sets of vibrational modes, each phase produces a characteristic Raman spectrum. The technique is non-destructive, requires no sample preparation beyond a flat surface, and achieves spatial resolution of ~1–2 μm when coupled to a confocal microscope — making it ideal for phase identification in the heterogeneous microenvironments of ceramic glazes and their interfaces. The choice of laser wavelength can influence the scattering efficiency, spectral resolution, and susceptibility to fluorescence, while the diffraction grating is adjusted to optimize spectral dispersion and resolution for the selected wavelength.

In this study, Raman spectroscopy was used to confirm the identity of bone ash-derived phases in the experimental replicas and, where possible, in the archaeological samples.

Micro-Raman spectroscopy (μ-RS) was used in the paint cross-sections using a Raman spectrometer Horiba XPlora equipped with a diode laser of operating at 532 nm, coupled to an Olympus microscope. Raman spectra were acquired in extended mode in the 100–1500 cm–1 region. The laser was focused with an Olympus 100× lens, 50-100% of the laser power on the sample surface (10 s exposure, 5 cycles of accumulation). The spectra were analysed with the equipment software (LabSPEC 5 from Horiba Jobin Yvon, France) application.

4.2.5 Thermogravimetric Analysis (TGA)

Thermogravimetric analysis records the mass of a sample continuously as it is heated through a controlled temperature programme. The instrument — a microbalance enclosed in a furnace with programmable atmosphere control — measures mass with microgram resolution while the sample is heated at a defined rate. Exothermic and endothermic events that involve mass change appear as steps in the mass-versus-temperature curve; their onset temperatures and integrated mass losses allow assignment to specific processes. Events that do not involve mass change (polymorphic transitions, for instance) are invisible to TGA but detectable by differential thermal analysis if run in parallel. The derivative of the mass curve (DTG) sharpens the onset and peak temperatures of each event, making overlapping steps easier to resolve.

In this study, bone ash powder was analysed from 40 to 1000°C at a heating rate of 10 K/min, under a controlled atmosphere. The choice of a slow ramp rate is deliberate: faster heating tends to shift event temperatures upward and can cause overlapping steps to merge, reducing resolution of adjacent transformations. The aim is to verify the completion of calcination and to confirm the absence of volatile content (residual organic matter, adsorbed water, carbonate) that would interfere with XRF

oxide quantification. The thermal stability of the calcined product is a prerequisite for reliable elemental analysis and confirms that the hydroxyapatite added to the replica glazes is chemically inert under the glaze firing conditions (700–900°C).

The ceramic paste weight loss of 1.47% at 1100°C, measured by gravimetric calcination, reflects the residual volatile content of the fired body — primarily structural water from incompletely dehydroxylated phyllosilicates and trace carbonate

4.2.6 X-ray Fluorescence (XRF)

X-ray fluorescence determines bulk elemental composition by irradiating a sample with primary X-rays energetic enough to eject inner-shell electrons from the atoms present. The resulting characteristic fluorescence X-rays, emitted as outer-shell electrons fall to fill the vacancies, have energies specific to each element; their intensities, after matrix correction, are proportional to elemental concentrations. The technique is non-destructive in the sense that no chemical dissolution is required, but the spatial resolution is limited — typically millimetres — so it measures an average composition over the analysed volume rather than individual phases.

In this study, XRF was used for two purposes: (i) bulk compositional characterisation of the ceramic paste and bone ash raw material; and (ii) in combination with XRPD and the $CaO–Al_2O_3–SiO_2$ ternary diagram, to constrain the firing temperature range of the original tiles. The data allow an assessment of whether the raw material choices and firing conditions of the experimental programme are plausible analogues for the Mértola production context The P_2O_5 content also functions as a tracer for bone ash addition to the glaze: phosphorus is virtually absent from typical lead-silica glaze raw materials (sand, galena, plant ash), so any significant P_2O_5 in the glaze bulk is a direct indicator of deliberate bone ash incorporation rather than contamination from the ceramic body.

Analyses were performed on lithium tetraborate ($Li_2B_4O_7$) fusion beads prepared from the ceramic paste and from the bone ash, at a sample-to-flux ratio that ensures complete dissolution of the material and eliminates mineralogical matrix effects. Loss on ignition of the ceramic paste was determined gravimetrically by firing approximately 1 g to 1100°C in pre-heated ceramic crucibles, and used as a correction factor for the XRF oxide totals.

4.2.7 Fourier-Transform Infrared Spectroscopy (FTIR)

Fourier-transform infrared spectroscopy measures the absorption of infrared radiation by the vibrational modes of chemical bonds and crystal lattice. In the mid-infrared range (4000–400 cm^{-1}), each molecular group and crystalline phase produces a characteristic pattern of absorption band

positions and relative intensities. FTIR is particularly sensitive to hydroxyl and carbonate species, which are weak Raman scatterers but prominent in the infrared — making it the preferred complement to Raman spectroscopy for the full characterisation of bone-derived apatite, where both the phosphate framework and the OH and CO_3^{2-} substituents carry diagnostic information.

In this study, FTIR was applied to both the raw bone ash and the calcined bone ash (1000°C, 2 h) to document the spectroscopic transformation induced by the calcination protocol and to confirm the phase identity and thermal maturation of the final product. The comparison between the two spectra is central to validating the preparation method.

5. Analytical Results

5.1 Characterization of bone ashes

5.1.1. X-Ray Fluorescence (XRF) Analysis

The bulk chemical composition of the bone ash was determined by XRF using the fused bead method. Each bead was prepared by mixing 1.2 g of sample with 12.0 g of lithium tetraborate flux ($Li_2B_4O_7$), at a 1:10 dilution ratio. Two beads were prepared: one from the bone ash sample, measured using the HRC_CERAMIC calibration programme, and one from NIST SRM 1400 (Bone Ash), used as a reference material to verify the accuracy of the measurement.

The composition of the bone ash is dominated by CaO (51.67 wt.%) and P_2O_5 (42.88 wt.%), which together account for over 97.8% of the total (Table 6). The CaO/P_2O_5 weight ratio of approximately 1.21 corresponds to a Ca/P molar ratio close to 1.67, consistent with stoichiometric hydroxyapatite ($Ca_{10}(PO_4)_6(OH)_2$), confirming the high phase purity of the material. All remaining oxides are below 0.05 wt.%, confirming negligible silicatic contamination. Among the trace elements, Sr (92 ppm) and Zn (91 ppm) fall within the range expected for biogenic hydroxyapatite, where these elements substitute Ca^{2+} in the crystal lattice.

Component	Concentration	Stat. Error
Major oxides (wt.%)		
Na_2O	1.31	± 0.90
MgO	1.28	± 0.31
Al_2O_3	0.45	± 0.08
SiO_2	0.17	± 0.04
P_2O_5	42.88	± 0024
S	0.05	± 0.02
K_2O	0.01	± 0.29
CaO	51.67	± 0.76
TiO_2	0.01	± 0.03
Fe_2O_3	0.01	± 0.01
Trace elements (ppm)		
Cl	40.5	± 0.08
V	78.7	± 1.14
Cr	177.5	± 0.59
Mn	29.8	± 0.68

Component	Concentration	Stat. Error
Ni	213.1	± 0.45
Cu	14.6	± 0.26
Zn	90.5	± 0.28
Rb	7.4	± 0.27
Sr	92.3	± 0.36
Zr	25.8	± 0.38
Ba	485.9	± 15.0

Table 6: Bulk chemical composition of bone ash determined by XR. Major oxides in wt.%, trace elements in ppm. Statistical error is the 1σ counting error. Elements below the lower limit of detection are not reported.

5.1.2 X-Ray Powder Diffraction (XRDP) Analysis

The XRDP pattern of the bone ash fired at 1000°C for 2 hours (Figure 16) shows a phase assemblage dominated by hydroxyapatite ($Ca_{10}(PO_4)_6(OH)_2$), identified by its characteristic reflections throughout the 5–65° 2θ range: specifically the 31.78° and 32.91° (Cu Kα radiation), corresponding to the (211) and (300) planes of the hexagonal apatite structure [48] . The diffractogram is consistent with a well-crystallised, phase-pure hydroxyapatite, with no secondary phases detectable at this resolution. The sharpness and intensity of the reflections indicate a high degree of crystallinity, as expected following thermal treatment at 1000°C, which promotes crystal growth and eliminates residual amorphous domains present in lower-temperature or unprocessed bone material. These results are fully consistent with the bulk chemistry determined by XRF, where the CaO/P_2O_5 ratio confirmed stoichiometric hydroxyapatite as the dominant phase.

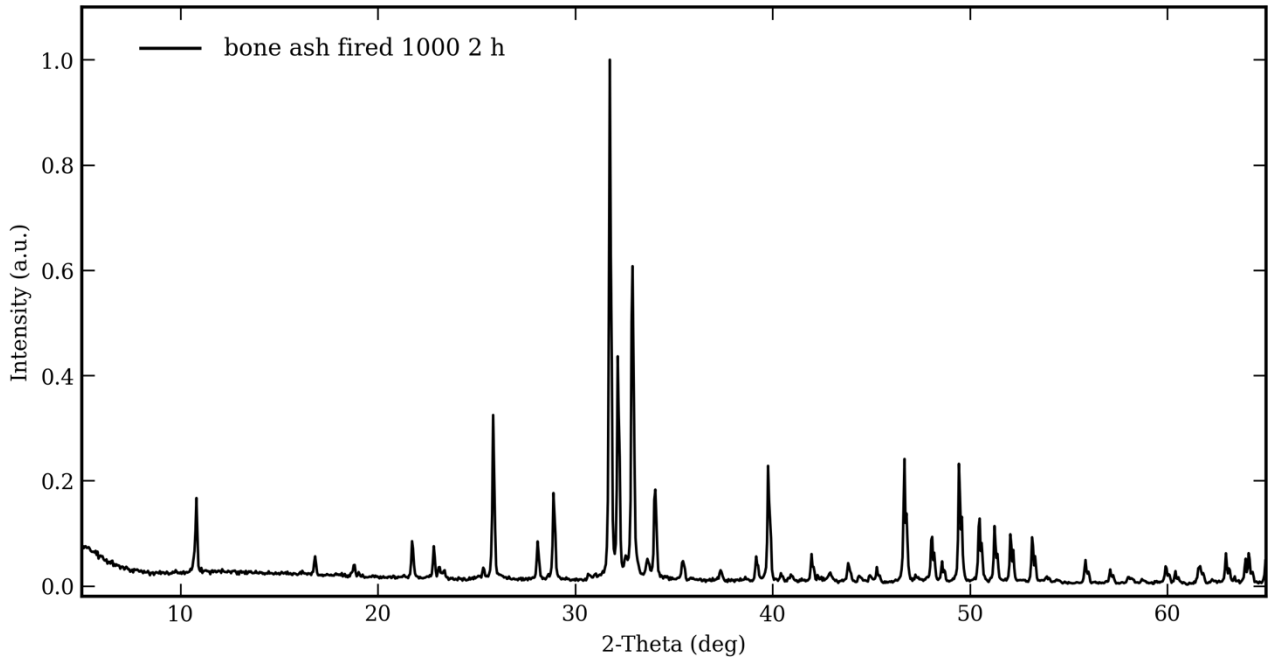


Figure 16. XRD pattern of bone ash calcinated at 1000°C for 2 hours. Reflections are consistent with phase-pure hydroxyapatite ($Ca_{10}(PO_4)_6(OH)_2$).

5.1.3 Thermogravimetric (TGA) Analysis

Thermogravimetric analysis (TGA) was performed on both the raw and calcinated bone ash (Figure 17 & Figure 18). The thermal behaviour observed is consistent with that reported in the literature for bovine bone-derived hydroxyapatite calcinated at increasing temperatures.

The raw bone exhibits a total mass loss of approximately 28% across the full temperature range, distributed across three distinct events. A first loss below 200°C is attributed to the release of residual surface-adsorbed moisture. Between 250 and 500°C, a major mass loss event is observed in the DTG curve, associated with the combustion and thermal decomposition of the organic fraction — primarily collagen[49] — which typically constitutes 30–40% of raw bone by weight. A third event between 600 and 800°C is attributed to the endothermic dissociation of phosphate and residual carbonate groups (PO_3^{2-}/CO_3^{2-}) substituted within the hydroxyapatite lattice between 600 and 800°C. The absence of a stabilisation plateau within the investigated range suggests that complete mineralisation requires temperatures approaching 1000°C [50].

T (°C)	Weight loss characterization	%
50-200	Residual surface-adsorbed moisture	4.17
250-500	Thermal decomposition of organic matter	20.42
600-800	Endothermic dissociation of CO_3^{2-}/PO_3^{2-}	3.55
>800	/ No further weight loss occurred	/

Table 7. Summary of mass loss events identified by TGA for raw bone ash. Temperature ranges and corresponding thermal processes are based on the TG/DTG curves (Figure 17).

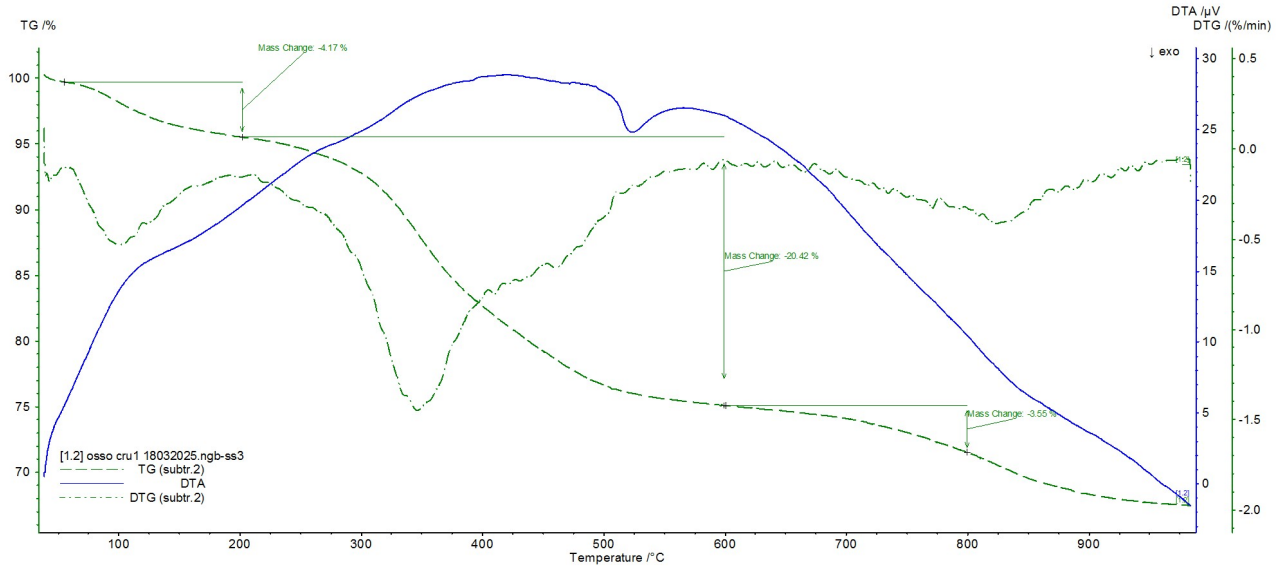


Figure 17. TGA/DTA/DTG curves of raw bone ash. Three mass loss events are identified: moisture release below 200°C (−4.17%), organic matter combustion between 250–500°C (−20.42%), and phosphate/carbonate group dissociation between 600–800°C (−3.5%).

The calcinated bone ash (1000°C, 2 h) shows a near-flat TGA curve with total mass losses below 1.2% across the entire temperature range, with no significant exothermic or endothermic events. This confirms complete elimination of the organic fraction and good thermal stability of the extracted hydroxyapatite, as expected at this calcination temperature. No further weight loss after 800°C is observed, in agreement with published data for hydroxyapatite calcinated at 950°C and above [50]. The slight apparent mass increase at low temperature is a buoyancy artefact and carries no physical significance.

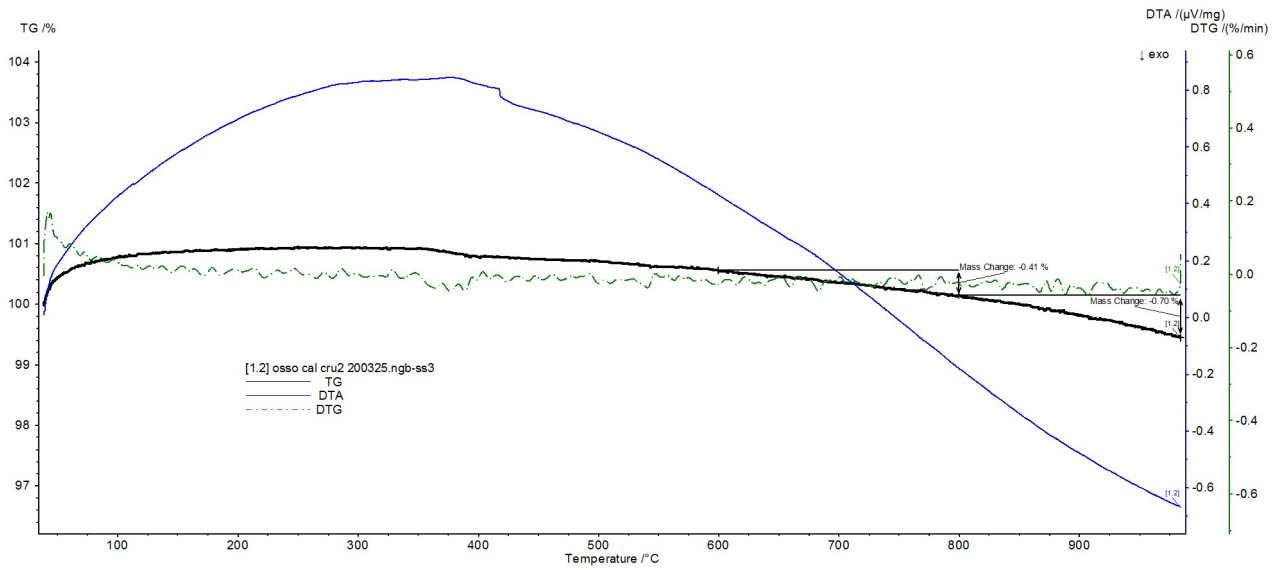


Figure 18. TGA/DTA/DTG curves of bone ash calcinated at 1000°C for 2 hours. Total mass loss below 1.2% with no significant thermal events, confirming complete removal of organic matter and thermal stability of the hydroxyapatite phase. The apparent mass increase at low temperature is a buoyancy artefact

5.1.4. FT-IR Spectroscopy Analysis

FTIR resolves the molecular-level functional groups — phosphate, hydroxyl, and carbonate — that define the structural state of hydroxyapatite and reveal any substitutions or disorder not detectable by diffraction alone.

FTIR spectra were collected on both the raw and calcinated bone ash (Figure 19 & Figure 20). The most diagnostic spectral region for hydroxyapatite is the 1000–1100 cm^{-1} range, where the ν_3 PO_4^{3-} asymmetric stretching modes produce strong, characteristic absorption bands; the sharpness and resolution of these bands are directly related to the degree of crystallinity of the material.

In the raw bone spectrum, the phosphate bands at 1080 cm^{-1} (ν_3 PO_4^{3-}) and 565/603 cm^{-1} (ν_4 PO_4^{3-}) are present but relatively broad, reflecting the lower crystallinity and structural disorder of unprocessed biogenic apatite. Additional bands confirm the presence of the organic fraction: a broad O–H/N–H absorption envelope between 3700 and 2800 cm^{-1}, a band at 1650 cm^{-1} (amide I, C=O stretching of collagen), and features at 1450 and 1415 cm^{-1} assigned to ν_3 CO_3^{2-} stretching from B-type carbonate substitution in the apatite lattice.

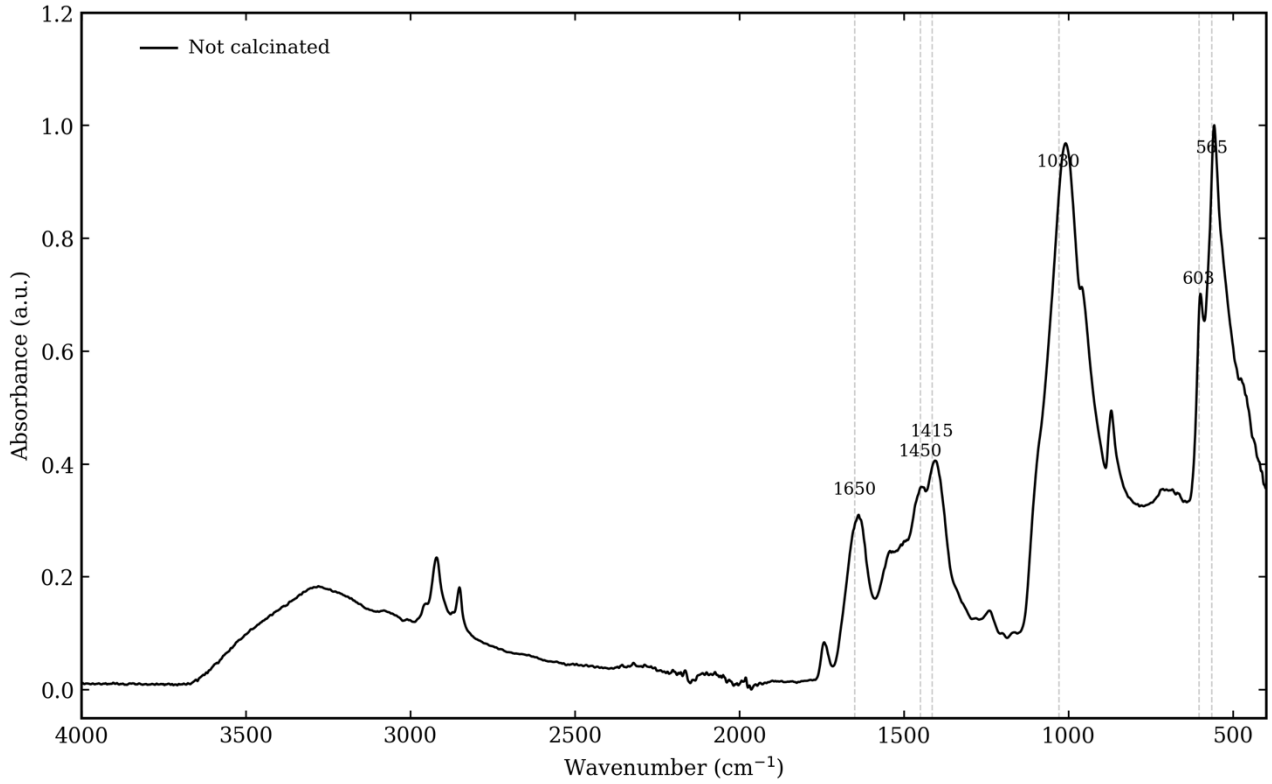


Figure 19. FTIR spectrum of raw (not calcinated) bone ash. Bands at 1650 cm⁻¹ (amide I, collagen), 1450 and 1415 cm⁻¹ (ν_3 CO_3^{2-}), and 1080/565/603 cm⁻¹ (ν_3 and ν_4 PO_4^{3-}) reflect the mixed organic–inorganic composition of unprocessed bone. The broad phosphate bands indicate lower crystallinity relative to the calcinated sample.

After calcination at 1000°C for 2 hours, the spectrum is dramatically simplified. All organic bands disappear entirely, and the carbonate features at 1415–1450 cm⁻¹ are no longer visible, consistent with the TGA results showing complete combustion of the organic matrix and loss of carbonate substitution at high temperature. Crucially, the phosphate bands become markedly sharper and better resolved: the ν_3 PO_4^{3-} band narrows to a well-defined peak at 1028 cm⁻¹ and the ν_4 doublet at 565 cm⁻¹ is clearly split, both diagnostic of a highly crystalline hydroxyapatite phase. A sharp O–H stretching band appears at 3571 cm⁻¹, characteristic of the structural hydroxyl channel in stoichiometric hydroxyapatite. This evolution from broad to sharp phosphate bands upon calcination is a consistent feature reported for bovine bone-derived hydroxyapatite and confirms the progressive structural ordering induced by high-temperature treatment, in full agreement with the XRD results [50].

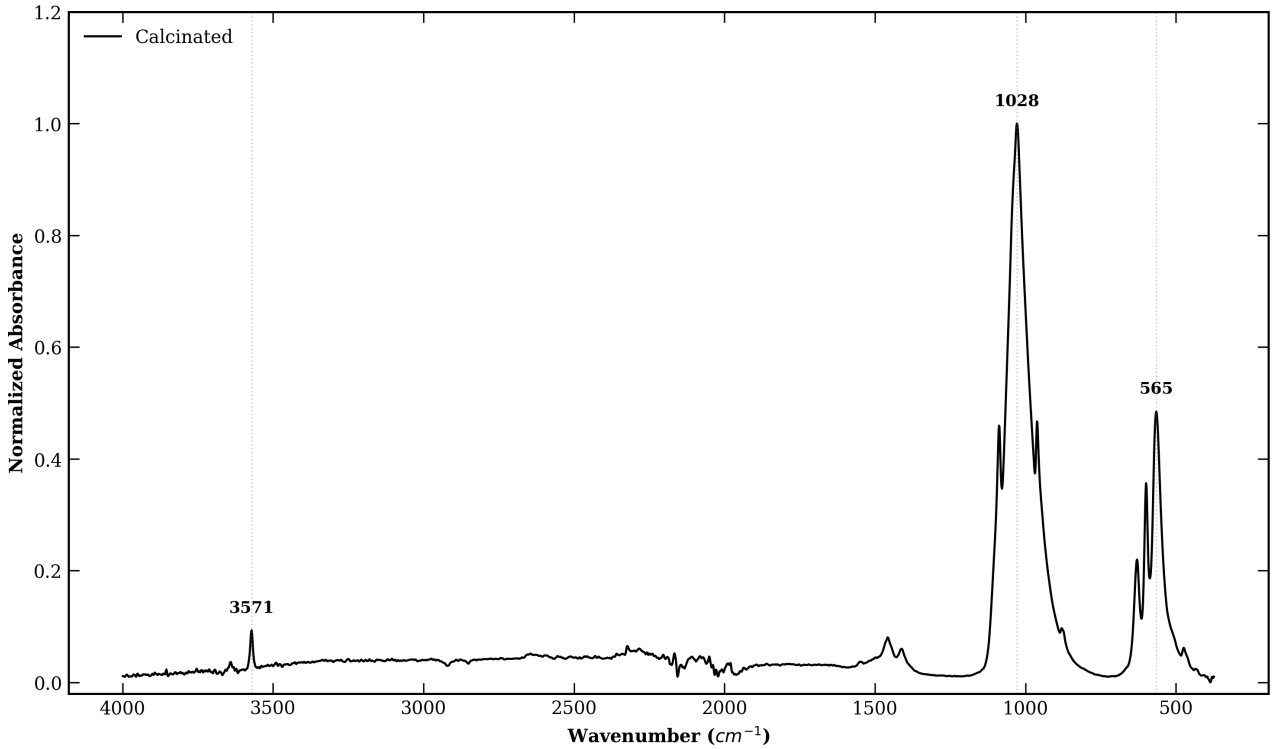


Figure 20. FTIR spectrum of calcinated bone ash (1000°C, 2 h). Principal bands: structural O–H stretching at 3571 cm⁻¹, ν₃ PO_4^{3-} at 1028 cm⁻¹ (sharp, well-resolved), ν₄ PO_4^{3-} doublet at 565 cm⁻¹. The sharpness of the phosphate bands reflects the high crystallinity of the calcinated material. Normalised absorbance

5.1.5 Raman Spectroscopy Analysis

Raman spectra were collected on the calcinated bone ash sample and on NIST SRM 1400 (Bone Ash) used as a reference material (Figure 21 & Figure 22). Both spectra are dominated by the ν₁ PO_4^{3-} symmetric stretching band at 962 cm^{-1}, the most diagnostic Raman band for hydroxyapatite. The calcinated sample yields a notably cleaner spectrum with a flat baseline, while the SRM 1400 spectrum shows broader features and a slightly elevated background, suggesting a lower degree of crystallinity in the commercial standard relative to the laboratory-calcinated material. This is consistent with the controlled high-temperature treatment (1000°C, 2 h) applied to the sample, which promotes crystal growth beyond what is typically achieved in commercially prepared bone ash. The band at 432 cm^{-1} in the sample spectrum (ν₂ PO_4^{3-}) and at 590 cm^{-1} in the standard (ν₄ PO_4^{3-}) are consistent with published hydroxyapatite reference spectra [50].

The diagnostic spectrum of hydroxyapatite is dominated by the ν₁ symmetric P–O stretching mode of the phosphate group at ~960 cm^{-1}, with secondary bands from the ν₂ and ν₄ bending modes between 400–600 cm^{-1} and the ν₃ antisymmetric stretching modes at 1050–1100 cm^{-1}. Carbonate substitution within the apatite lattice — common in biogenic hydroxyapatite — produces additional bands at ~1400–1500 cm^{-1}. The sharpness and relative intensity of the 960 cm^{-1} peak are sensitive to

crystallinity: poorly crystalline or defect-rich apatite from low-temperature calcination shows a broad, asymmetric band, while well-crystallised material calcined above 900°C displays a narrow, symmetric peak. This crystallinity shift provides an internal consistency check between the Raman data and the TGA/XRD evidence on calcination state.

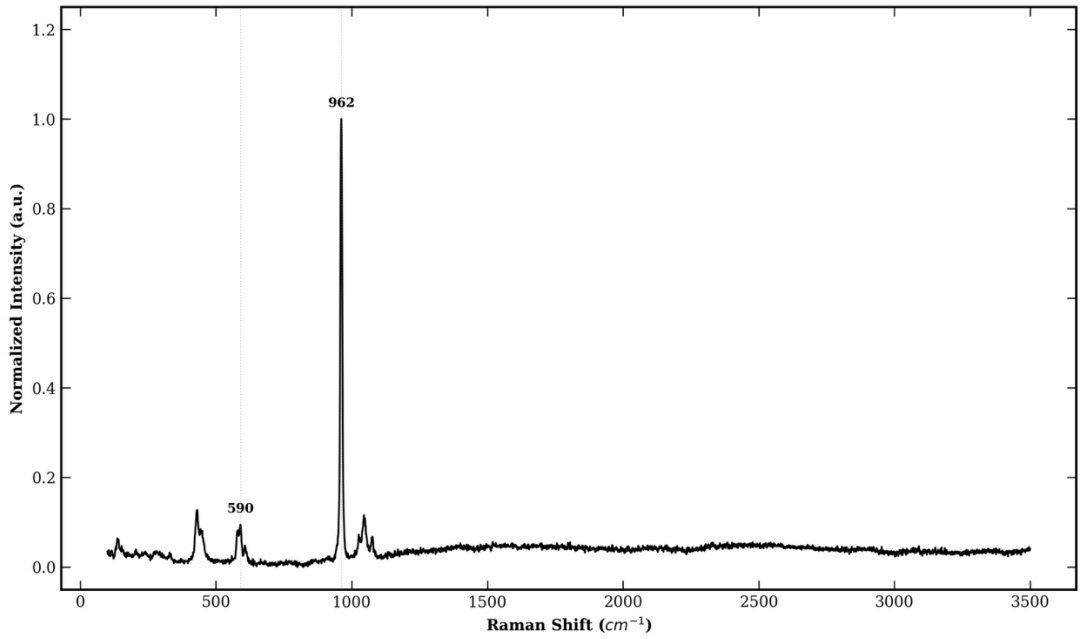


Figure 21. Raman spectrum of calcinated bone ash (1000°C, 2 h). Dominant band at 962 cm⁻¹ (ν_1 PO_4^{3-} symmetric stretching). Band at 432 cm⁻¹ assigned to ν_2 PO_4^{3-}. Normalised intensity (a.u.).

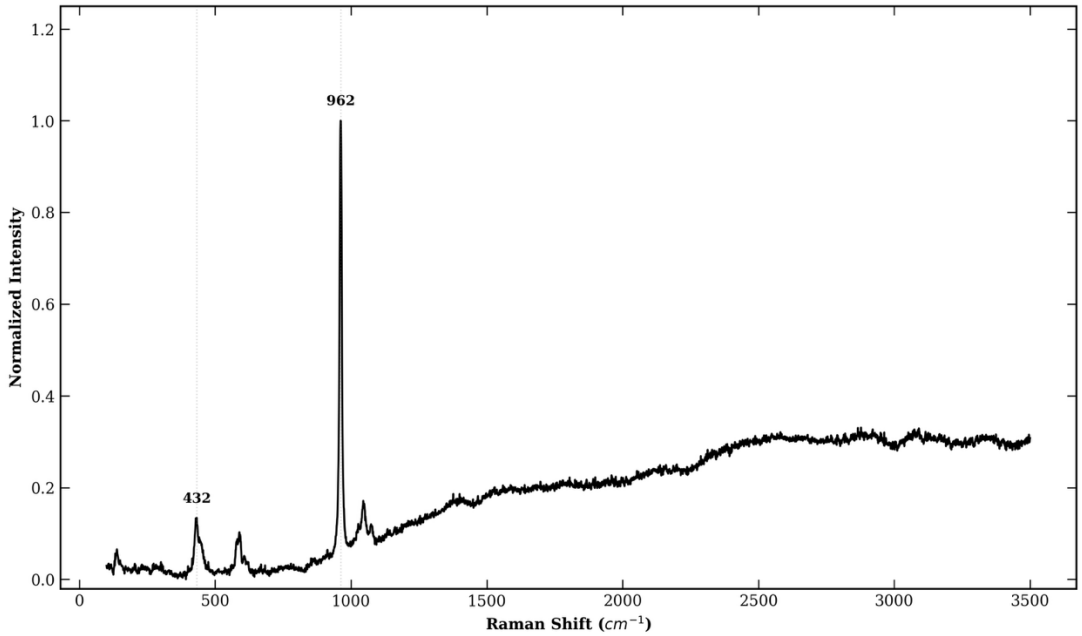


Figure 22. Raman spectrum of NIST SRM 1400 (Bone Ash), measured as reference material. Dominant band at 962 cm⁻¹ (ν_1 PO_4^{3-}). Band at 590 cm⁻¹ assigned to ν_4 PO_4^{3-}. The broader baseline relative to the calcinated sample reflects the lower crystallinity of the commercial standard. Normalised intensity (a.u.).

5.2. Characterisation of the ceramic body

The use of calcareous clays—common in the southern Iberian Peninsula—was likely a deliberate choice to ensure thermal expansion compatibility with the glaze and to provide a pale substrate that enhances the final glaze appearance. The interaction between the calcium-rich body and the lead-rich glaze during firing creates an interfacial layer that influences the overall structural integrity and optical properties of the vessel [51].

5.2.1 X-Ray Fluorescence (XRF) Analysis

The bulk chemical composition of the pre-fired calcareous ceramic tiles was determined by X-ray fluorescence spectrometry (XRF). Three independent replicates were measured for each sample, and results are reported as mean values with associated standard deviation (SD) and relative standard deviation (%RSD). All values are expressed as weight percent (wt.%) of oxides.

Oxide	Mean (wt.%)	SD	%RSD
Na_2O	0.17	0.08	47.1
MgO	2.50	0.03	1.2
Al_2O_3	18.06	0.07	0.4
SiO_2	56.85	0.09	0.2
P_2O_5	0.13	0.01	7.7
S	0.06	0.00	—
K_2O	3.25	0.06	1.8
CaO	10.73	0.01	0.1
TiO_2	0.80	0.01	1.3
Fe_2O_3	4.64	0.02	0.4
Oxides total	**97.19**		
LOI	**1.47**		
Total	**98.66**		

Table 8. Bulk chemical composition of pre-fired calcareous ceramic tiles determined by XRF. Values are expressed as mean wt.% ± standard deviation (SD) of n = 3 replicates. %RSD = relative standard deviation. — indicates SD = 0.00 or concentration below reliable quantification threshold

The XRF data presented in Table 8 reveal a compositional profile consistent with a calcareous ceramic body, characterised by a dominant silica content and a substantial calcium oxide fraction.

Silicon dioxide (SiO_2) represents the principal oxide with a mean of 56.85 ± 0.09 wt.%, followed by aluminium oxide (Al_2O_3) at 18.06 ± 0.07 wt.%, calcium oxide (CaO) at 10.73 ± 0.01 wt.%, and iron oxide (Fe_2O_3) at 4.64 ± 0.02 wt.%. These four major oxides account for approximately 90 wt.% of the total composition.

The elevated CaO content (>10 wt.%) is a defining characteristic of calcareous ceramic bodies and reflects the significant contribution of calcite-bearing raw materials, typically marls or calcareous clays, to the ceramic paste. During firing, the thermal decomposition of calcite ($CaCO_3$) above approximately 850°C releases CO_2 and produces free lime (CaO), which subsequently reacts with silicates and aluminosilicates to form calcium-rich phases such as gehlenite ($Ca_2Al_2SiO_7$) and anorthite ($CaAl_2Si_2O_8$). The identification and quantification of these neogenic phases are discussed in the XRD analysis section (following section).

The potassium oxide (K_2O) content of 3.25 ± 0.06 wt.% and the relatively minor MgO (2.50 ± 0.03 wt.%) suggest the presence of phyllosilicate minerals, namely illite and chlorite respectively, as primary components of the clay fraction. The low TiO_2 content (0.80 ± 0.01 wt.%) is characteristic of sedimentary clays with limited contribution from heavy mineral fractions.

Minor components include Na_2O (0.17 ± 0.08 wt.%), P_2O_5 (0.13 ± 0.01 wt.%), and S (0.06 wt.%), the latter likely representing residual sulfate phases. The notably high %RSD observed for Na_2O (47.1%) reflects the very low absolute concentration of this oxide, approaching the detection limit of the instrument, rather than genuine compositional heterogeneity of the ceramic body.

The analytical reproducibility, as expressed by the % RSD values, is excellent for the major and minor oxides, with values consistently below 2% for all oxides above 1 wt.%. This confirms the homogeneity of the ceramic paste and the reliability of the XRF measurements.

The total oxide sum of 97.26 wt.%, complemented by a loss on ignition (LOI) of 1.47 wt.%, yields a combined total of 98.73 wt.%, consistent with the expected range for a fired calcareous ceramic material. The LOI value reflects the residual mass loss associated with the thermal decomposition of minor carbonate phases, the loss of structural water from incompletely dehydroxylated phyllosilicates and trace carbonate and the combustion of residual organic matter not fully eliminated during the pre-firing stage. The relatively low LOI confirms that the ceramic body had undergone substantial decarbonation prior to analysis, as expected for a pre-fired tile.

4.2 X-Ray Diffraction Powder (XRDP) Analysis

XRDP patterns were collected on ceramic tile samples fired at 950°C and 1100°C (Figure 23,Figure 24) to characterize the phase assemblage and track the mineralogical transformations induced by thermal treatment. The comparison between the two diffractograms provides direct evidence of the progressive recrystallisation processes governing the evolution of the calcareous ceramic body with increasing firing temperature. The central question being whether the phase assemblages observed in the prefabricated tiles are consistent with the temperatures estimated for the archaeological samples, and thus being able to to constrain the original firing temperature range and soaking time with the aim of reproducing the same conditions experimentally (in the replicas).

950°C pattern. The diffractogram retains several reflections attributable to the original clay mineral assemblage. Phyllosilicate phases are identified by a characteristic basal reflection at approximately 8–9° 2θ, with a secondary peak around 19–20° 2θ, both of which persist with limited intensity reduction up to 950°C. This behaviour indicates incomplete dehydroxylation of the clay fraction at this firing temperature, consistent with the slow kinetics of phyllosilicate breakdown in calcareous systems, as documented in the literature for calcareous clays fired under oxidizing conditions [18]. Quartz reflections, most prominently the principal peak at ~26.6° 2θ, remain stable across both firing temperatures, confirming that quartz acts as an inert non-plastic filler within the investigated temperature range. Feldspar reflections are also consistently present. Calcite, identified by its diagnostic reflection at ~29.4° 2θ, is fully absent in both patterns, confirming complete decarbonation below 700°C, in agreement with the thermal decomposition temperature of calcite in fine-grained ceramic matrices. The disappearance of calcite liberates reactive CaO, which constitutes the primary driver of the high-temperature phase crystallization sequence described below.

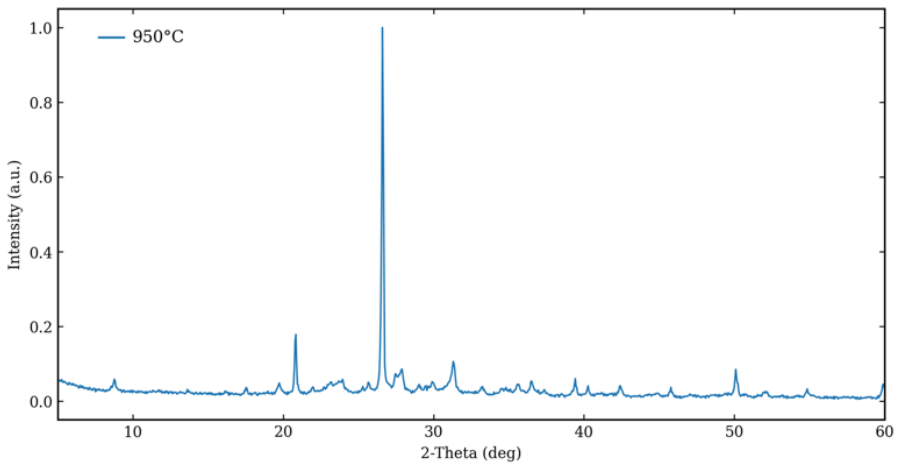


Figure 23. XRPD pattern of the ceramic body fired at 950°C. Intensities are normalized (a.u.) to highlight the mineralogical phases and crystallinity at intermediate firing stages.

1100°C pattern. The progressive increase in firing temperature from 950°C to 1100°C triggers significant mineralogical reorganization, reflected in the appearance and growth of new crystalline phases. At intermediate temperatures (750–850°C), hematite (Fe_2O_3) begins to crystallize, as evidenced by a reflection at ~33° 2θ. Its formation indicates oxidizing firing conditions, under which iron released from the breakdown of Fe-bearing phyllosilicates is oxidized rather than being incorporated into reduced iron-bearing silicate phases. This is consistent with the reddish colouration typically associated with oxidized calcareous ceramics.

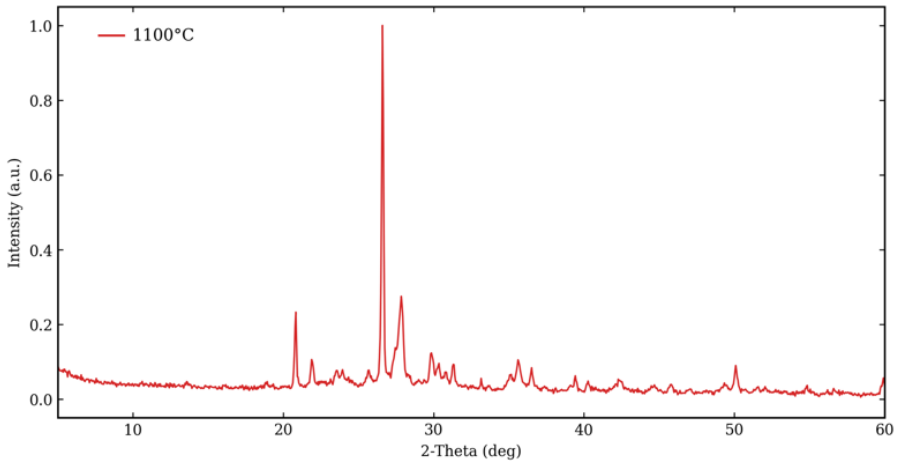


Figure 24. XRPD pattern of the ceramic body fired at 1100°C. Intensities are normalized (a.u.), showing the phase transformations and mineralogical evolution at the peak firing temperature

At higher temperatures, the available CaO released by calcite decomposition reacts with the alumina and silica derived from the molten aluminosilicate matrix to produce calcium-rich neogenic silicate phases. Gehlenite ($Ca_2Al_2SiO_7$) and kermanite ($Ca_2MgSi_2O_7$) are identified as intermediate crystallization products in this temperature range. These phases are metastable under prolonged high-temperature conditions: as firing temperature increases toward and beyond 1000°C, gehlenite and kermanite progressively dissolve in favour of more stable phases, notably calcic plagioclase (anorthite, $CaAl_2Si_2O_8$) and Ca–Mg–Fe pyroxenes (diopside-series, $(Ca,Mg,Fe)_2Si_2O_6$). Iron not partitioned into hematite is thus incorporated into the pyroxene structure, reducing the proportion of free iron oxides and shifting the ceramic body colour toward paler, more whitish tones — a diagnostic feature noted in analogous fired calcareous assemblages.

At 1100°C, the diffractogram shows a marked increase in pyroxene reflections and enhanced plagioclase crystallinity, alongside a reduction in gehlenite/kermanite peak intensities, indicating that the high-temperature phase equilibrium strongly favours the anorthite & diopside assemblage. The elevated and broad background signal in this pattern is also consistent with an increasing proportion of vitreous phase, as partial melting of the aluminosilicate matrix is expected above ~1050°C in calcareous compositions.

1100°C, 6 hours. After 6 hours of soaking, the background increases substantially and the relative intensity of the quartz peak decreases, indicating progressive incorporation of silica into the glassy matrix and further development of pyroxene and plagioclase phases. The higher amorphous content suggests the body is moving towards over-firing relative to original production conditions, with a degree of vitrification that would not have been achievable in a traditional wood-fired kiln.

Implications for firing conditions. The phase assemblage observed in the analyzed tiles is consistent with a calcareous ceramic body fired under oxidizing conditions at temperatures in the range of 950–1100°C. The coexistence of residual phyllosilicate reflections with nascent pyroxene and plagioclase phases at 950°C places the lower bound of effective firing in this interval, while the pronounced pyroxene crystallization and incipient vitrification at 1100°C define the upper limit of the investigated range. These data will be further integrated with the XRF bulk chemistry and ternary diagram projection to constrain the most probable firing temperature and atmospheric conditions of the original production.

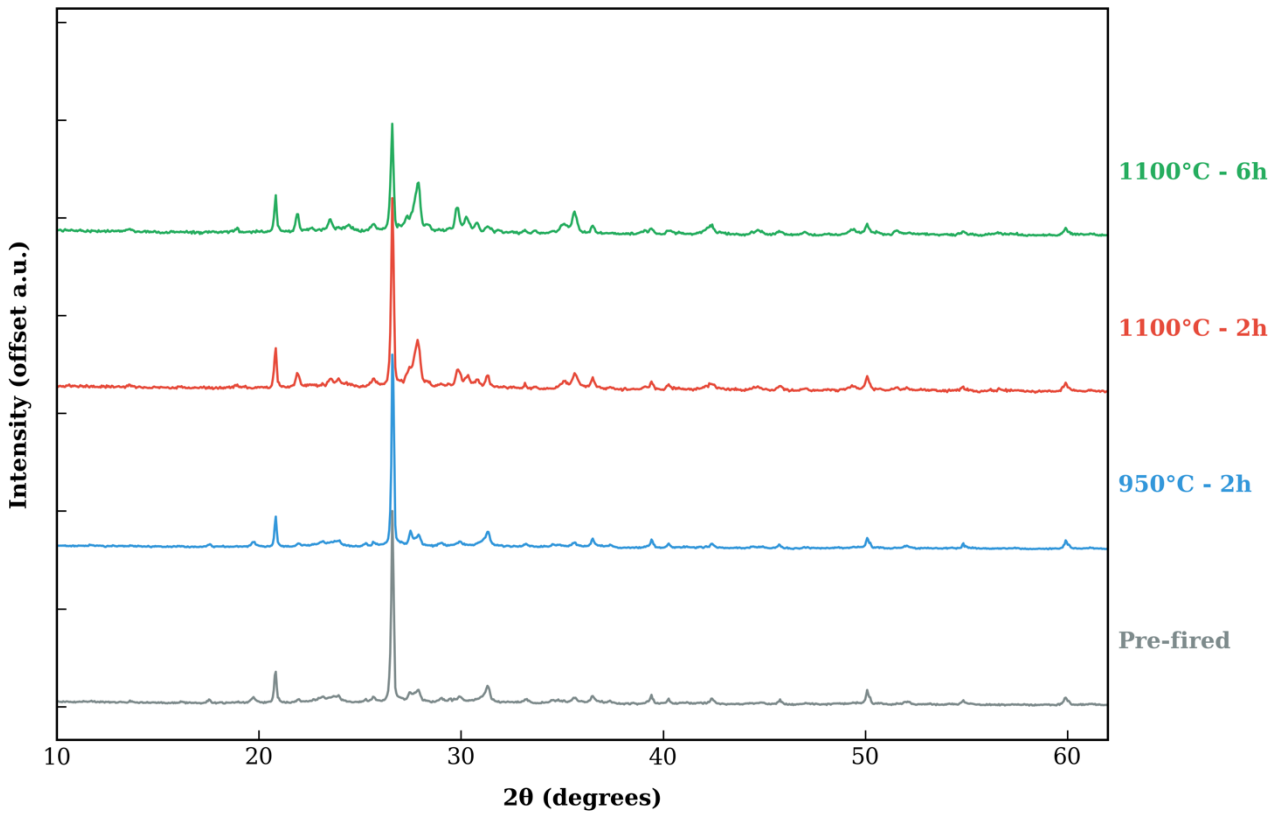
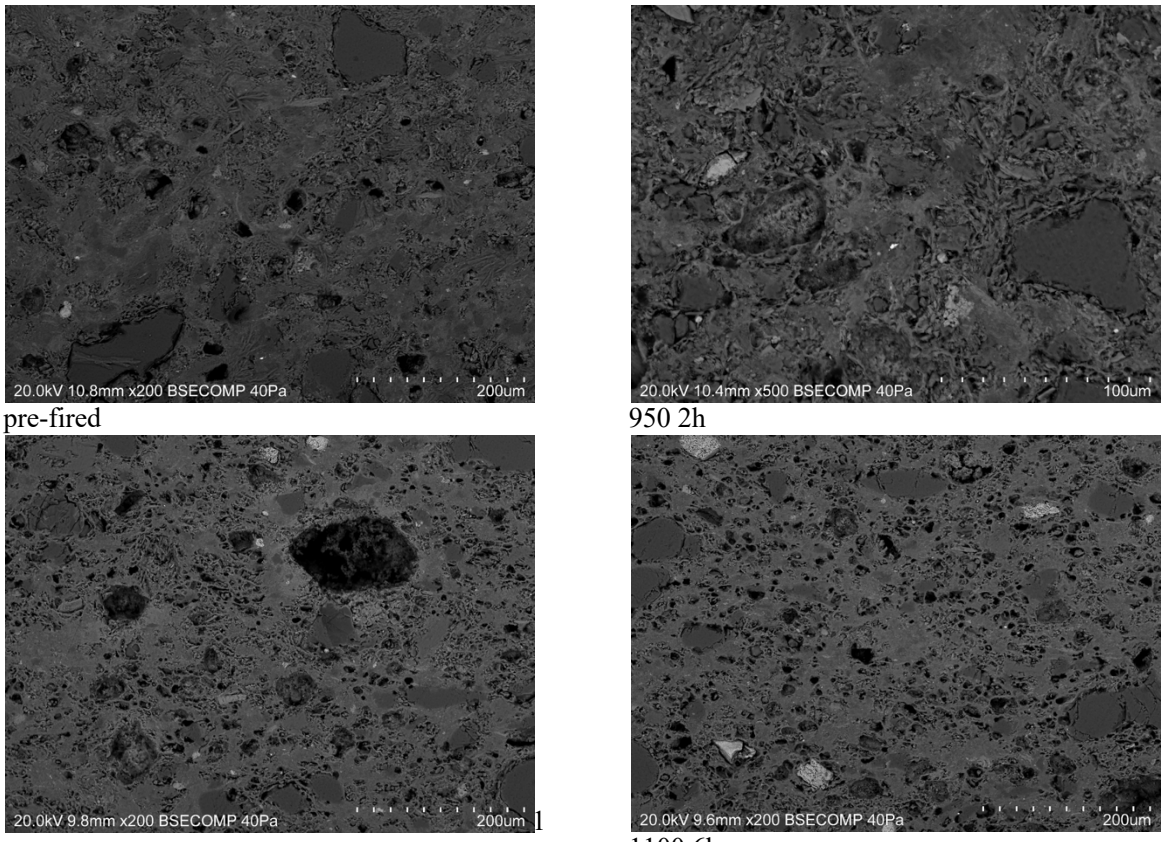


Figure 25. XRPD patterns of the ceramic body samples showing the thermal mineralogical evolution from the pre-fired state up to 1100. The stacked plot illustrates the phase transformations as a function of firing temperature and holding time. Intensities are normalized and displayed in arbitrary units with a vertical offset applied to the patterns to facilitate comparative analysis of peak intensity and crystallinity.

Sample	quartz (01-085-0797)	gehlenite (01-072-2128)	hematite (01- 079-1741)	plagioclase (01-076-0927)	potassium feldspate (01-075-1190)	Muscovite /illite (01- 075-0948)	pyroxene (01-075-1577)
Precotto 950	43	7	1	21	10	8	10
R1 950	49	6	1	18	10	7	9
1100 2h	28	3	2	42	12	/	13
1100 6h	22	3	2	46	14	/	13

Table 9. Semi-quantitative phase composition of the ceramic body at four thermal conditions, determined by the RIR method. Values in wt%. "/" = phase not detected.

5.2.2 Scanning Electron Microscopy: microstructural evolution of the ceramic body



pre-fired

950 2h

100 2h

1100 6h

*Figure 26. SEM-BSE micrographs illustrating the microstructural evolution of the ceramic body: **(a)** Pre-fired state showing a porous matrix with unreacted clay aggregates and quartz inclusions; **(b)** 950°C showing incipient sintering and early glassy phase formation; **(c)** 1100°C (2 h) showing advanced densification and partial quartz dissolution; **(d)** 1100°C (6 h) showing a mature microstructure with enhanced vitrification and phase coarsening due to prolonged soaking.*

The XRPD phase quantification and SEM-BSE imaging together document the progressive mineralogical transformation of the calcareous ceramic body across the investigated temperature range. At 950 °C — the pre-firing condition used as a substrate for the experimental replicas — quartz remains the dominant crystalline phase (43–49 wt%), accompanied by gehlenite (6–7 wt%), plagioclase (18–21 wt%), potassium feldspar (10 wt%), muscovite/illite (7–8 wt%), hematite (1 wt%), and pyroxene (9–10 wt%). The persistence of muscovite/illite at this temperature indicates that dehydroxylation of the phyllosilicate fraction is not yet complete, while the presence of gehlenite — a calcium aluminium silicate ($Ca_2Al_2SiO_7$) — confirms that carbonate decomposition has released sufficient calcium to drive the first neoformation reactions. This assemblage is entirely consistent with the theoretical framework outlined in Chapter 2, which predicts gehlenite as the primary high-temperature phase in calcareous clays between approximately 850 and 1000 °C. At 1100 °C, the phase assemblage shifts markedly: quartz content drops to 22–28 wt%, muscovite/illite is no longer detectable, and plagioclase rises to 42–46 wt% while pyroxene stabilises at 13 wt%. This transformation records the progressive conversion of gehlenite — a metastable intermediate — to the equilibrium anorthite-dominated assemblage, driven by increasing temperature and extended soaking time. The SEM-BSE images mirror this evolution: at 950 °C the matrix retains angular quartz grains and a heterogeneous texture, whereas at 1100 °C the glassy background expands and quartz inclusions are visibly rounded and reduced in number, indicating partial dissolution into the melt. The extended soaking at 1100 °C for 6 hours produces a further increase in the amorphous fraction and minor coarsening of the pyroxene phase, suggesting that beyond 2 hours of soaking the body approaches a degree of vitrification that would not have been achievable in a traditional wood-fired kiln operating with uncontrolled cooling rates. The coexistence of residual quartz with incipient pyroxene and plagioclase at 950 °C, and the incomplete transformation to the anorthite equilibrium at 1100 °C, is diagnostic of a calcareous ceramic body fired in the 950–1100 °C range under oxidising conditions — fully consistent with the archaeometrically documented production technology of al-Andalus glazed wares.

To further constrain the firing conditions inferred from XRD, the bulk XRF composition was normalised to the (CaO+MgO)–Al_2O_3–SiO_2 ternary system (SiO_2: 64.5 wt.%, Al_2O_3: 20.5 wt.%, CaO+MgO: 15.0 wt.%) and projected onto the corresponding ternary phase diagram (Figure 27). This system governs phase stability in calcareous ceramics fired under oxidizing conditions and provides the thermodynamic framework for interpreting the observed mineralogical sequence

The sample plots in the transitional zone between the gehlenite ($Ca_2Al_2SiO_7$) and anorthite ($CaAl_2Si_2O_8$) stability fields, fully consistent with the XRD evidence: at 950°C the gehlenite is the

dominant neogenic phase, while at 1100°C anorthite and diopside-series pyroxenes progressively replace it as the equilibrium assemblage. This compositional positioning confirms that the ceramic body lies precisely within the temperature-sensitive transition interval between these two-phase fields, reinforcing the interpretation that the original firing temperature falls within the 950–1100°C range under oxidizing atmospheric conditions. The coexistence of metastable intermediate phases with equilibrium products is a well-documented kinetic signature of traditional pre-industrial kilns, where rapid and uncontrolled cooling quenches the phase assemblage before full thermodynamic equilibration is reached — consistent with the operational characteristics of Islamic kilns in the Iberian Peninsula, which typically achieved peak temperatures in the 900–1100°C range without sustained isothermal soaking.

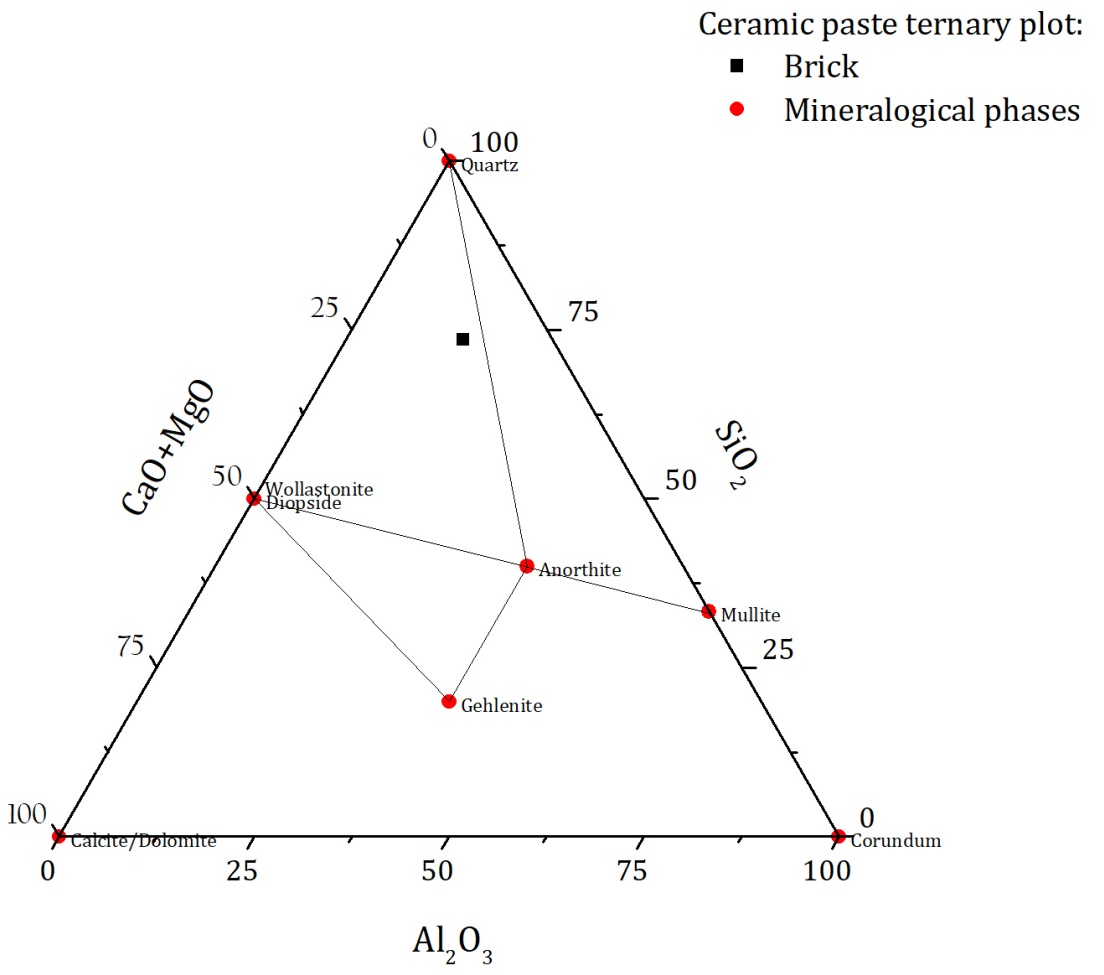


Figure 27.. Projection of the bulk XRF composition (normalised to the (CaO +MgO)–Al_2O_3–SiO_2 ternary system) of the pre-fired calcareous ceramic tiles. The sample plots in the transitional zone between the gehlenite and anorthite stability fields, consistent with the phase assemblage observed by XRD at 950°C and 1100°C respectively. Phase field boundaries are approximate and based on the NIST CaO–Al_2O_3–SiO_2 system. In this (CaO+MgO)–Al_2O_3–SiO_2 system, CaO and MgO are treated as a single basic oxide component given their similar geochemical behaviour and the subordinate MgO content (2.50 wt.%) of the ceramic body

Normalizing the major oxide data to the $CaO–Al_2O_3–SiO_2$ system — the three components governing phase stability in calcareous ceramics fired under oxidizing conditions — the composition of the analyzed tiles plots within the anorthite primary phase field, in proximity to the gehlenite–anorthite–wollastonite boundary region. This position is fully consistent with the XRD evidence presented in Section 4.2, where gehlenite and kermanite are observed as intermediate phases giving way to anorthite and diopside-series pyroxenes at temperatures approaching and exceeding 1000°C. In oxidizing calcareous systems, this compositional field predicts an anorthite + diopside + liquid assemblage as the stable high-temperature product, in agreement with the phase crystallization sequence documented in the diffractograms.

Firing temperature estimation. The integration of XRF composition, XRD phase assemblage, and CAS phase equilibria allows for a refined estimation of the original firing conditions. The complete absence of calcite, the partial persistence of phyllosilicate reflections, and the contemporaneous presence of gehlenite/kermanite alongside incipient anorthite and pyroxene at 950°C collectively indicate that the lower bound of the firing temperature lies in the 900–950°C range. The more advanced pyroxene crystallisation and the onset of vitrification observed at 1100°C suggest that this temperature was not systematically reached or sustained during original production.

On the basis of these observations, and with reference to comparative data from analogous calcareous ceramic assemblages from the Al-Andalus tradition of the Iberian Peninsula [52] the most probable effective firing temperature of the original tiles is estimated in the range of 950–1050°C. This interval is consistent with the technological capabilities of pre-industrial Islamic kilns in the Iberian Peninsula, which typically operated intermittent updraft or downdraft wood-fired structures capable of reaching peak temperatures in the 900–1100°C range, but with limited ability to maintain isothermal conditions for extended soaking times.

Cooling regime and technological implications. The natural, uncontrolled cooling characteristic of traditional kiln technologies — a slow post-firing cooling curve — favours the metastable preservation of intermediate phases such as gehlenite and kermanite rather than their complete conversion to the equilibrium anorthite + diopside assemblage. This kinetic overprint, well documented in the archaeometric literature on calcareous ceramics[1], is precisely what renders the coexistence of gehlenite, pyroxene, and plagioclase in the same ceramic body a diagnostic indicator of traditional firing practice, as opposed to a controlled laboratory firing where thermodynamic equilibrium would be more closely approached.

The observed phase assemblage therefore reflects not a single equilibrium temperature, but rather the integrated thermal history of the ceramic body: a rapid heating stage reaching peak temperatures in the 950–1050°C range, followed by a slow and uncontrolled cooling during which metastable phases

were partially quenched. This interpretation is fully consistent with the pre-industrial production technology inferred for the Al-Andalus ceramic tradition and provides a robust archaeometric framework for the technological characterisation of the investigated tiles.

5.3 Characterisation of archaeological samples: DMI, SEM Images, Raman Spectra, EDS quantifications

CRVM666 GREEN

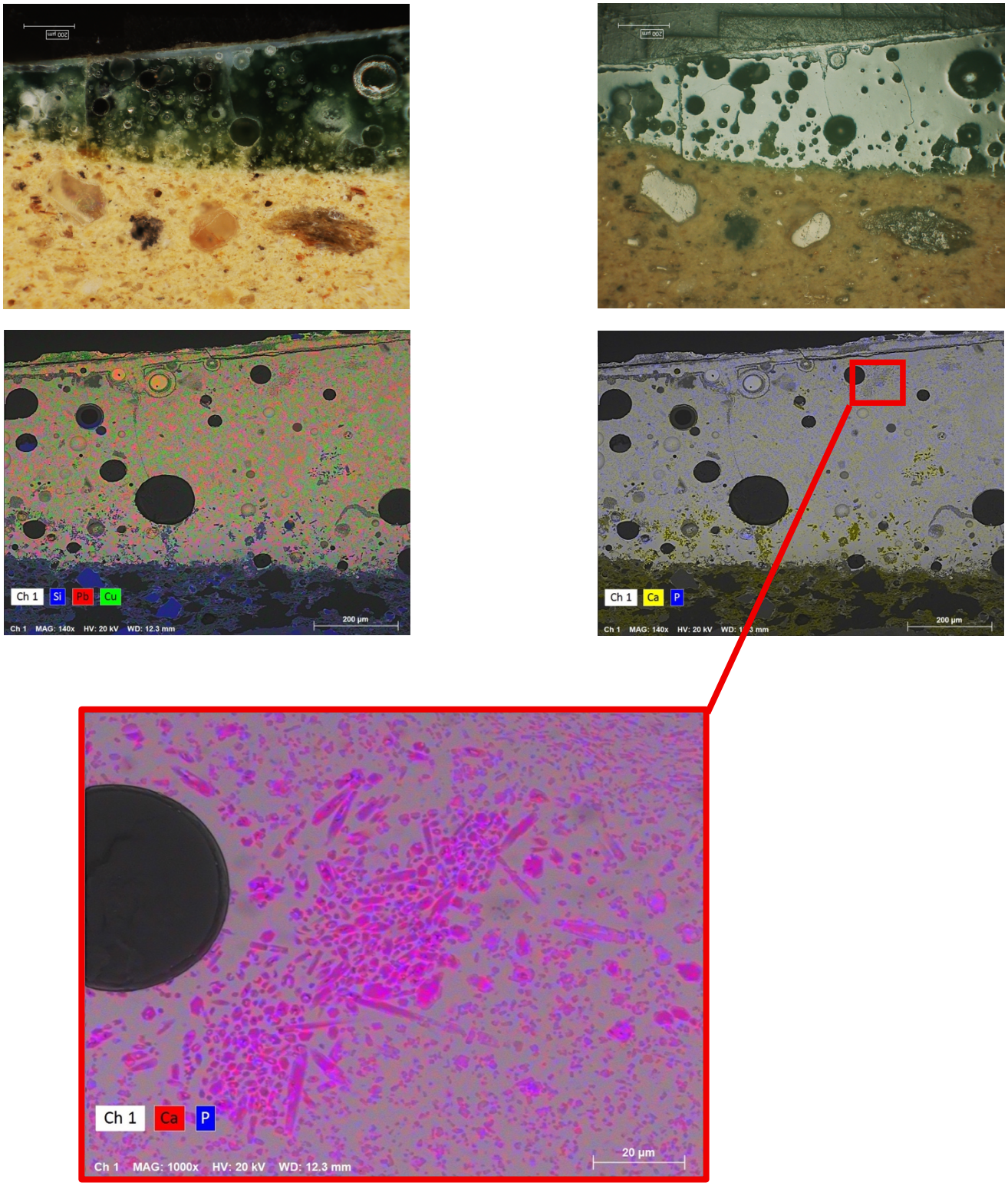
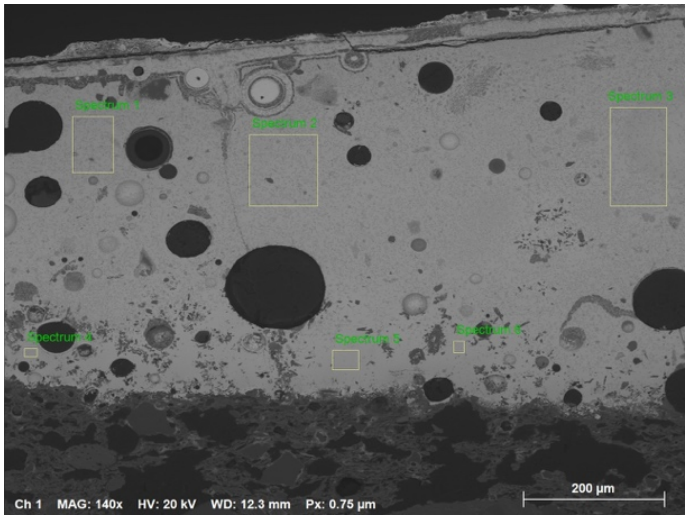


Figure 28. Digital Microscopy image in PL & XPL,, and EDS elemental mapping of sample CRVM666 GREEN, with detail of SEM-EDS composite elemental map of the glaze (Ca = red, P = blue). The distinct magenta coloration of the dispersed acicular (needle-like) crystals reveals a perfect spatial correlation between calcium and phosphorus, confirming the widespread precipitation of a calcium phosphate phase.



	AVR	SD
Na_2O	1.15	0.22
MgO	0.46	0.09
Al_2O_3	1.87	1.37
SiO_2	25.56	3.71
P_2O_5	2.04	2.05
K_2O	0.63	0.33
CaO	5.27	2.11
Fe_2O_3	0.78	0.42
PbO	53.82	1.99
TiO_2	0.08	0.09
SnO_2	0.57	0.22
MnO	/	/
CuO	1.84	0.13

Table 10. Quantitative chemical composition (wt.%) of the glaze oxides determined by EDS analysis.

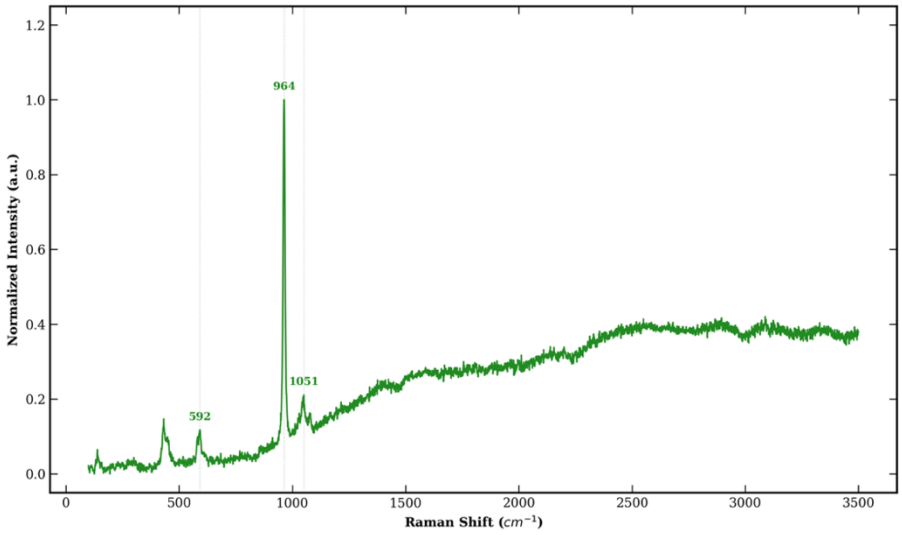
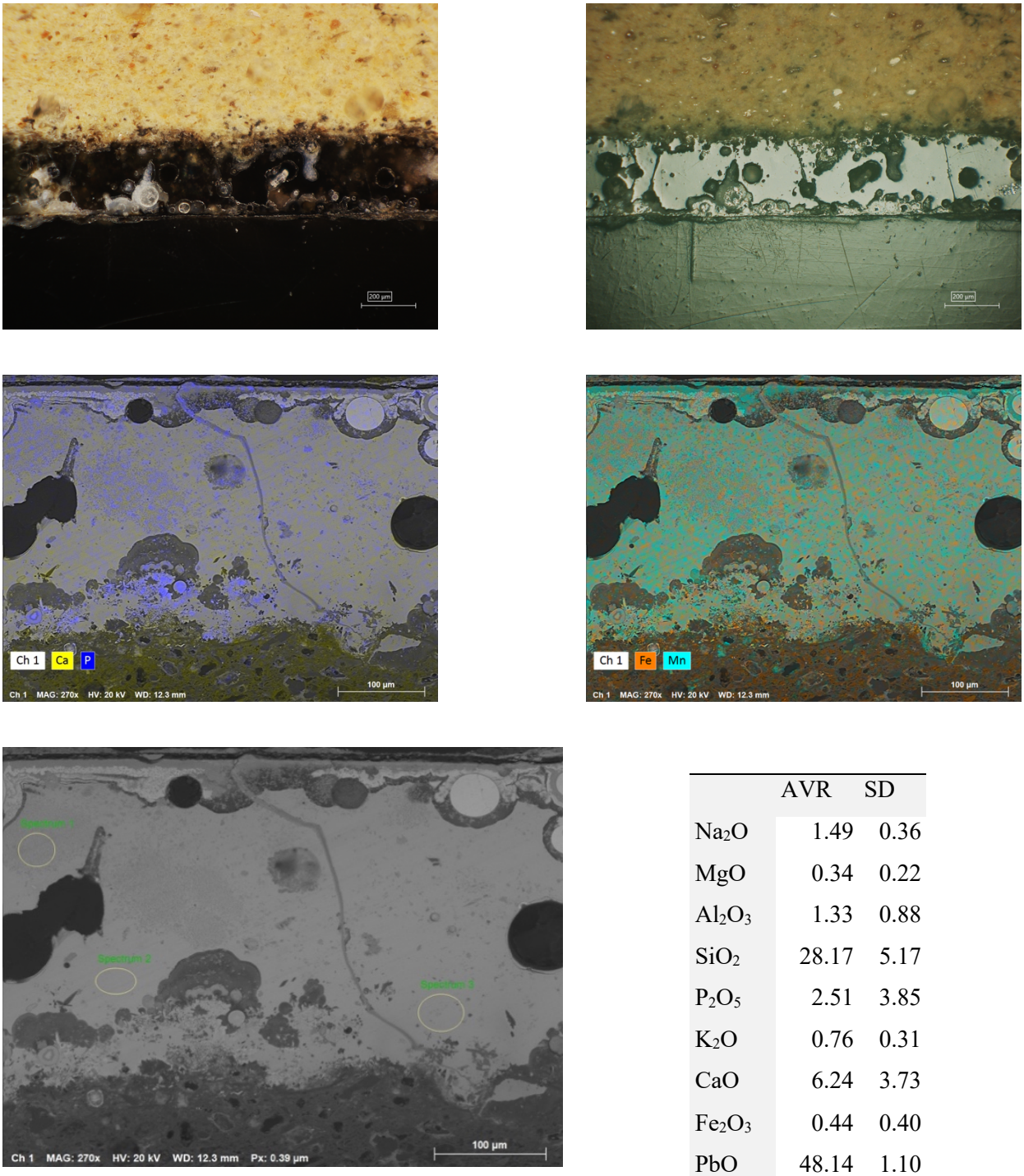


Figure 29. Raman spectrum of crvm666 GREEN SPOT

The Raman spectrum displays a well-resolved band at 962–965 cm^{-1}, consistent with the ν_1 PO_4^{3-} stretching mode of calcium phosphate, confirming that bone-ash-derived hydroxyapatite survives within the glaze matrix. The co-occurrence of measurable P (2.04 wt%) and elevated Ca (5.27 wt%) in the EDS data supports this identification. CuO (1.84 wt%) is the chromophore responsible for the green colouration of this zone. SEM-EDS elemental mapping clearly shows the diffuse precipitation of acicular crystals. The perfect stoichiometric overlap of Ca and P (magenta areas) confirms that

these sub-micrometric inclusions are indeed calcium phosphates, providing the primary opacification mechanism.

CRVM666 BLACK



	AVR	SD
Na_2O	1.49	0.36
MgO	0.34	0.22
Al_2O_3	1.33	0.88
SiO_2	28.17	5.17
P_2O_5	2.51	3.85
K_2O	0.76	0.31
CaO	6.24	3.73
Fe_2O_3	0.44	0.40
PbO	48.14	1.10
TiO_2	0.07	0.03
SnO_2	1.00	0.49
MnO	2.40	0.59

Figure 30. Digital Microscopy image in PL & XPL, SEM-BSE image, and EDS elemental mapping of sample CRVM666 BLACK

Table 11. Quantitative chemical composition (wt.%) of the glaze oxides determined by EDS analysis.

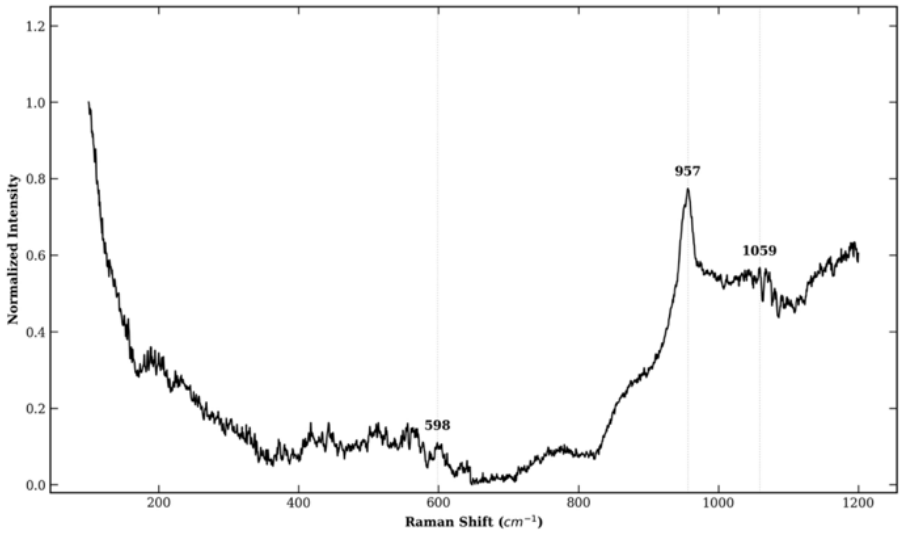


Figure 31. Raman spectrum of crvm666 BLACK SPOT

The EDS data for sample 666 show the highest concentrations of P and Ca (P = 2.51 wt%, Ca = 6.24 wt%), with a Ca/P ratio consistent with the use of bone ash as a phosphate-bearing opacifier. However, the Raman spectrum lacks the sharp peak typically associated with crystalline hydroxyapatite (the main component of bone ash) in the 960–970 cm^{-1} region. This suggests that the bone ash may have partially reacted with or dissolved into the silicate matrix, resulting in a poorly crystalline or amorphous phosphate phase that remains below the Raman detection limit. Mn (2.40 wt%) acts as the primary chromophore for the dark colouration

CRWM1668 GREEN

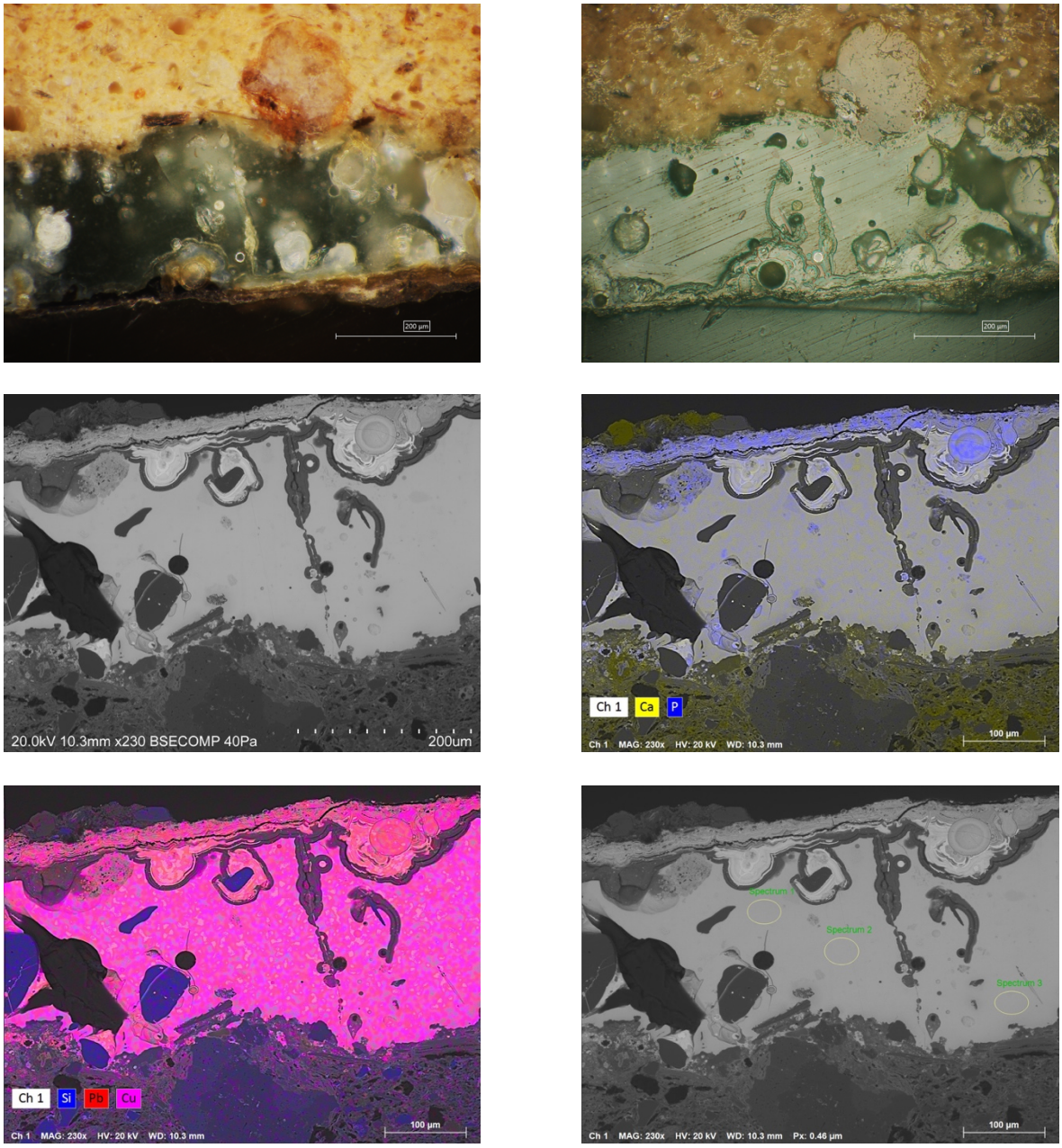


Figure 32. Digital Microscopy image in PL & XPL, SEM-BSE image, and EDS elemental mapping of sample CRVM1668 GREEN.

	AVR	SD
Na_2O	1.80	0.07
MgO	0.10	0.07
Al_2O_3	1.21	0.08
SiO_2	34.36	0.34
P_2O_5	0.00	0.00
K_2O	0.65	0.08
CaO	2.54	0.41
Fe_2O_3	0.58	0.11
PbO	52.03	0.53
TiO_2	0.05	0.02
SnO_2	0.00	0.00
MnO	0.52	0.08
CuO	1.27	0.06

Table 12. Quantitative chemical composition (wt.%) of the glaze oxides determined by EDS analysis.

EDS elemental mapping reveals a complex distribution of phosphorus: while a significant concentration is observed in the uppermost layer—likely due to environmental contamination during burial—P-bearing particles are also scattered within the bulk glaze. Despite their presence, these particles remained undetectable via Raman spectroscopy, likely due to their small size, low crystallinity, or concentrations falling below the instrumental threshold. Furthermore, the lack of a clear stoichiometric Ca/P correlation in certain spots suggests that while bone ash was indeed introduced, it may have partially dissolved into the glassy matrix or remained as sub-micrometric clusters at the limit of detection. This explains the difficulty in confirming the phase as crystalline hydroxyapatite, despite the chemical evidence provided by EDS.

CRVM1668 BLACK

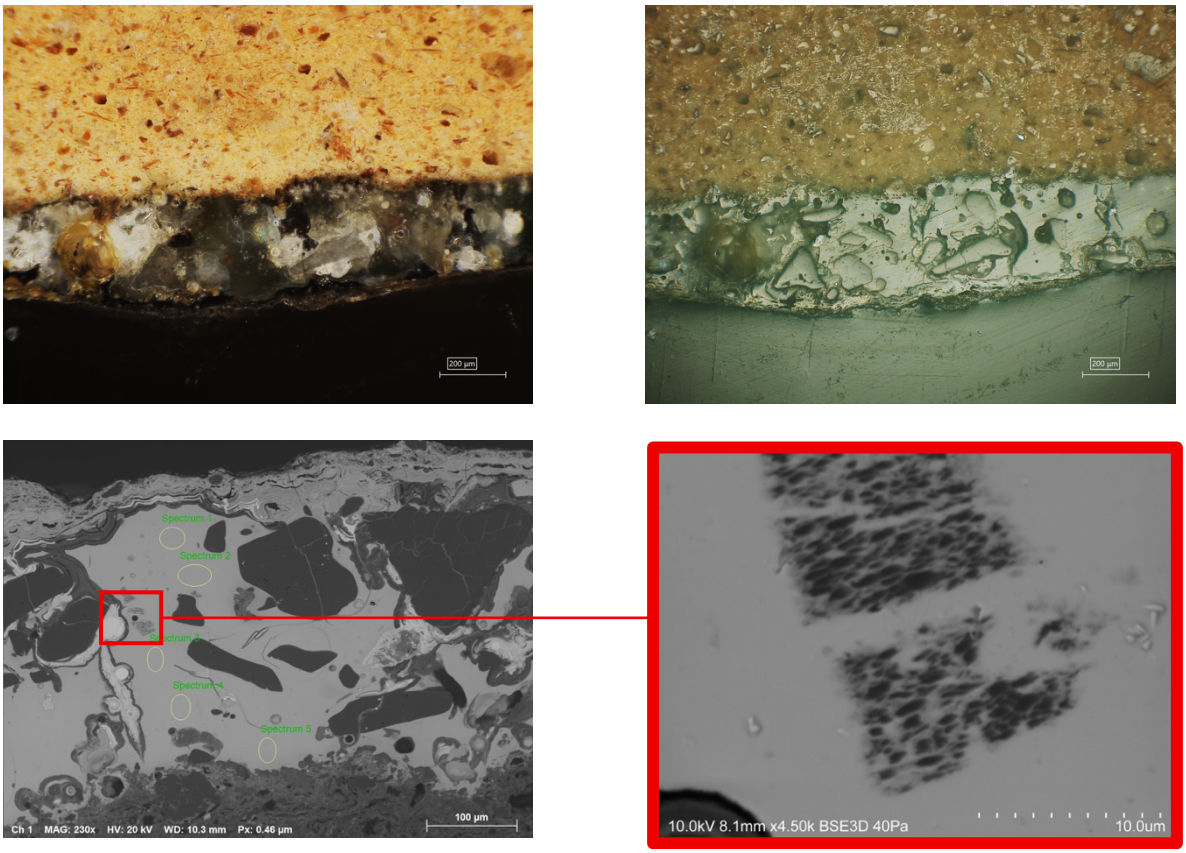


Figure 33. Digital Microscopy image in PL & XPL, SEM-BSE image, and detail of sample CRVM1668 BLACK.

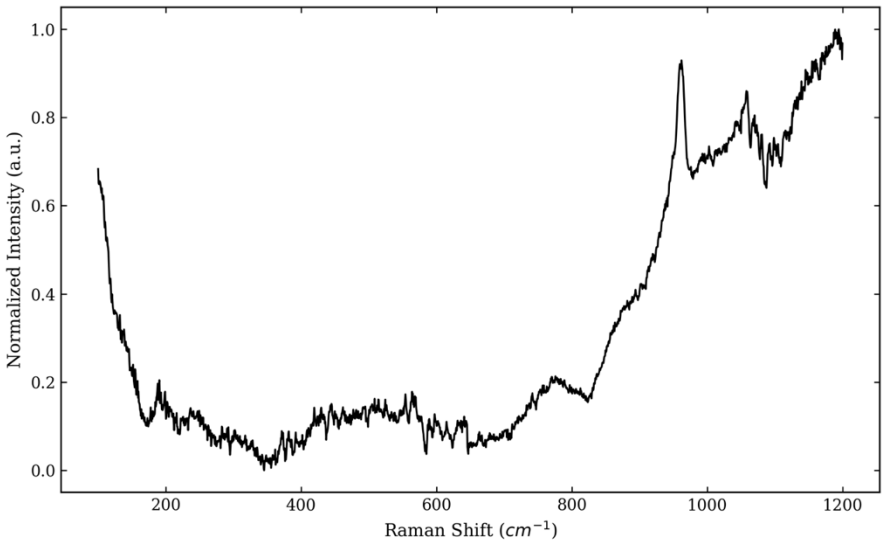


Figure 34. Raman spectrum of sample CRVM1668 BLACK.

Table 13. Quantitative chemical composition (wt.%) of the glaze oxides determined by EDS analysis.

	Mean	SD
Na_2O	1.74	0.09
MgO	0.10	0.05
Al_2O_3	1.01	0.35
SiO_2	33.00	5.89
P_2O_5	0.00	0.00
K_2O	0.51	0.06
CaO	2.24	0.45
Fe_2O_3	0.48	0.27
PbO	51.70	7.54
TiO_2	0.01	0.01
SnO_2	1.89	0.47
MnO	1.32	0.21

As in the green zone, P is undetectable throughout the black glaze area (P = 0.00 wt%). The presence of Sn (1.89 wt%) indicates that tin oxide is the primary opacifier in this zone, in contrast to the bone-ash-based strategy identified in sample 666. The SEM detail inset reveals dense, sub-rectangular crystalline inclusions distributed throughout the glaze layer, consistent in morphology with cassiterite (SnO_2) precipitates.

CRVM623 SECONDARY GLAZE

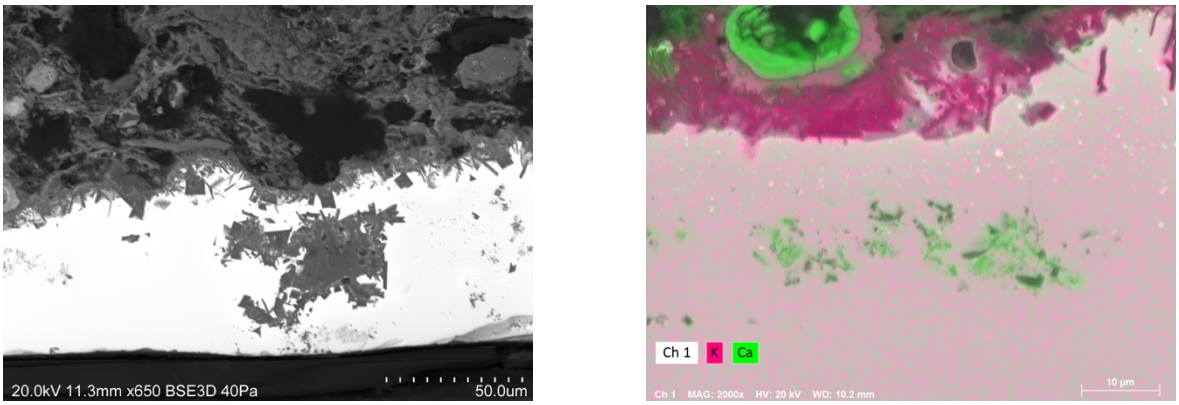


Figure 35. SEM-BSE image of sample CRVM623 "under", and EDS elemental mapping of a detail.

	AVR	SD
Na_2O	0.98	0.06
MgO	0.56	0.06
Al_2O_3	4.59	0.39
SiO_2	32.70	0.67
P_2O_5	0.00	0.00
K_2O	2.43	0.03
CaO	3.61	0.05
Fe_2O_3	1.82	0.07
PbO	45.37	0.06
TiO_2	0.13	0.07
SnO_2	0.51	0.21
MnO	0.21	0.05
CuO	0.07	0.08

Table 14. Quantitative chemical composition (wt.%) of the glaze oxides determined by EDS analysis.

The EDS data for sample 623 show a distinctive pattern: P = 0.00 wt% across all analysed zones, including the secondary glaze area imaged here. The extremely low Pb content (0.76 wt%) and the high standard deviations across most oxides reflect the highly heterogeneous and degraded character of the secondary glaze, where body-derived contamination and post-depositional alteration make compositional interpretation uncertain. No Raman spectra could be extracted from this sample: although EDS mapping identified localised areas with marginally elevated Ca, phosphorus concentrations remained below the threshold for a reproducible spectroscopic signal. Sample 623 therefore provides neither positive nor negative evidence for bone ash use, and its opacification strategy remains unresolved pending higher-resolution analysis.

5.4 Characterisation of replicas: DM, SEM Images, Raman Spectra, EDS quantifications

R7

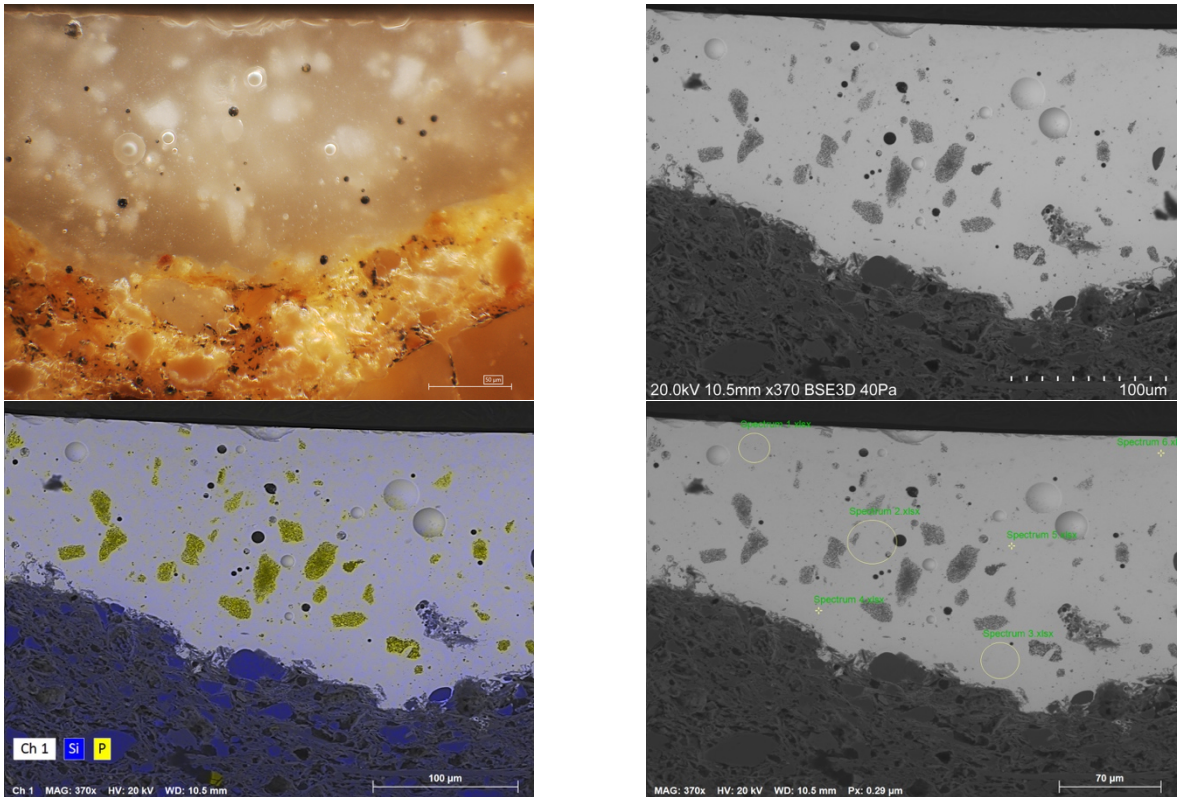


Figure 36. Digital Microscopy image at [1000x] magnification, SEM-BSE image, and EDS elemental mapping of sample R7.

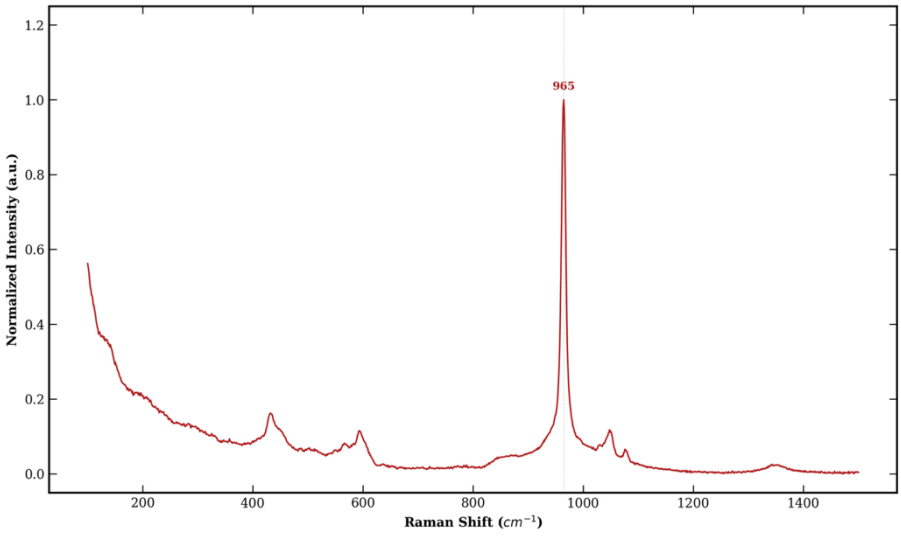


Figure 37. Raman spectrum of sample R7,

	AVR	SD
Na_2O	0.39	0.05
MgO	0.28	0.09
Al_2O_3	2.25	0.84
SiO_2	26.80	2.24
P_2O_5	0.73	0.69
K_2O	0.25	0.10
CaO	2.65	0.53
Fe_2O_3	0.45	0.28
PbO	58.67	2.35
TiO_2	0.18	0.07
SnO_2	1.71	0.54

Table 15. Quantitative chemical composition (wt.%) of the glaze oxides determined by EDS analysis.

The band at 965 cm^{-1} identifies residual crystalline hydroxyapatite retained within the glaze at 700 °C. The SEM-BSE image confirms an incompletely fused matrix with abundant spherical bubbles; at this temperature, light scattering by entrapped air is the dominant whitening mechanism rather than crystalline opacification.

R8

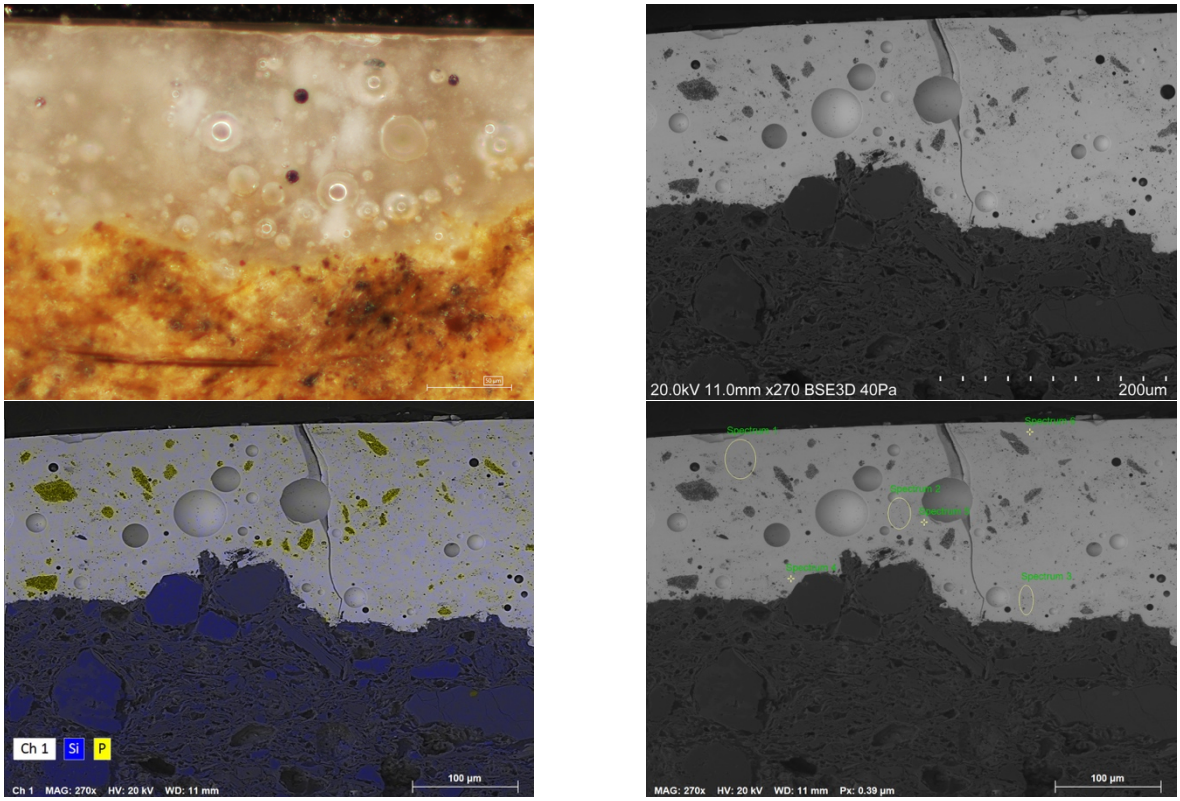


Figure 38. Digital Microscopy image at [1000x] magnification, SEM-BSE image, and EDS elemental mapping of sample R8.

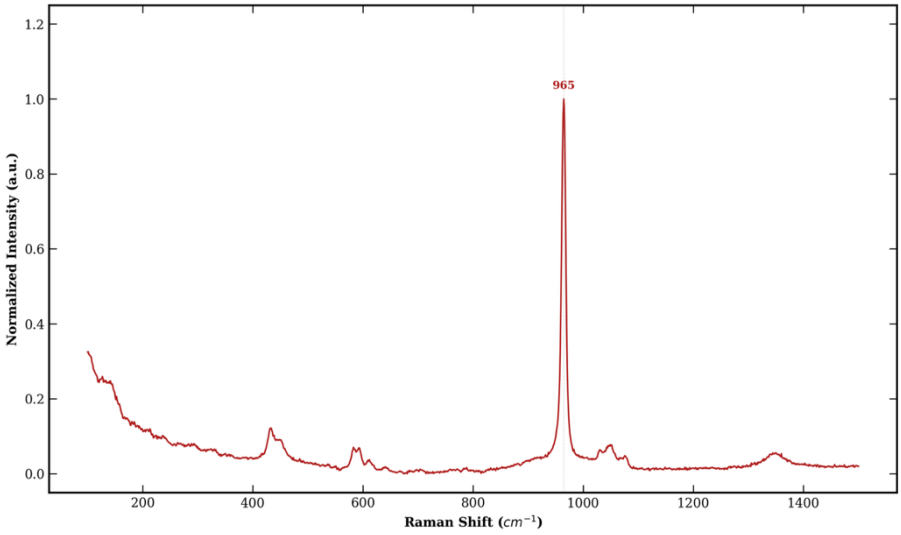


Figure 39. Raman spectrum of sample R8,

	AVR	SD
Na_2O	0.34	0.12
MgO	0.16	0.01
Al_2O_3	1.82	0.29
SiO_2	25.35	0.21
P_2O_5	0.69	0.15
K_2O	0.22	0.08
CaO	2.10	0.43
Fe_2O_3	0.29	0.11
PbO	61.13	1.35
TiO_2	0.04	0.01
SnO_2	1.93	0.64

Table 16. Quantitative chemical composition (wt.%) of the glaze oxides determined by EDS analysis.

At 800 °C the phosphate band persists at 965 cm^{-1} and the glaze matrix is partially fused. The BSE image shows a reduction in bubble population relative to R7, and the first discrete Ca-P crystallites and tin-oxide clusters become visible, marking the transition from bubble-dominated to crystalline opacification.

R9

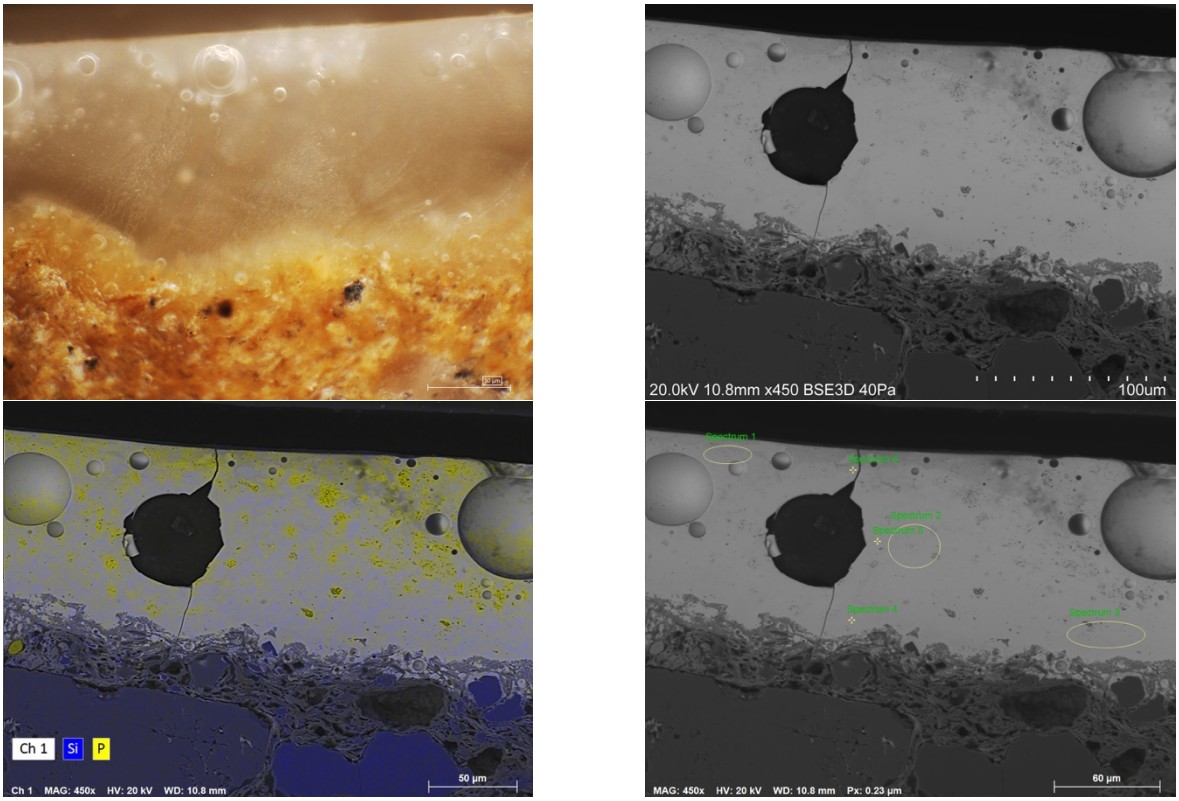


Figure 40. Figure X. Digital Microscopy image at [1000x] magnification, SEM-BSE image, and EDS elemental mapping of sample R9.

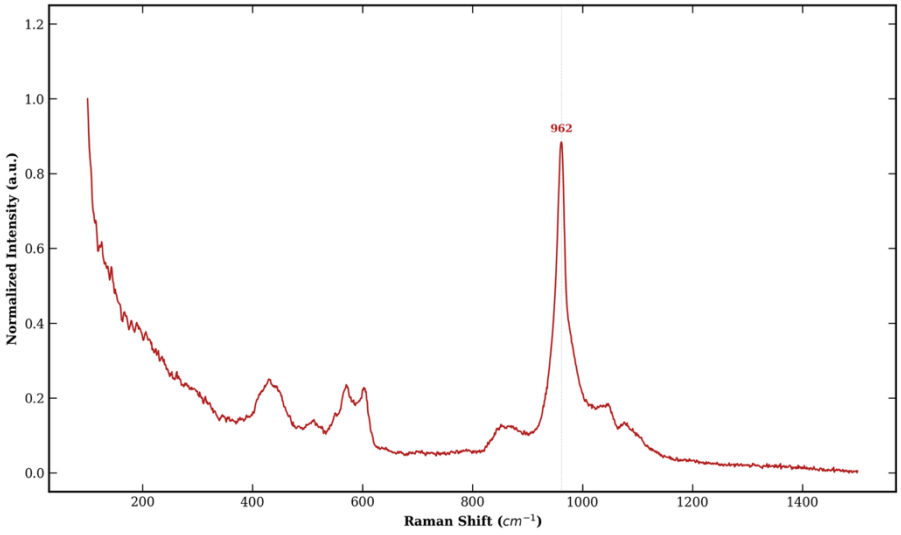


Figure 41. Raman spectrum of sample R9

	AVR	SD
Na_2O	0.26	0.03
MgO	0.32	0.06
Al_2O_3	3.16	1.96
SiO_2	26.95	4.14
P_2O_5	1.80	1.92
K_2O	0.46	0.22
CaO	4.24	1.25
Fe_2O_3	0.62	0.33
PbO	53.56	3.47
TiO_2	0.11	0.07
SnO_2	2.06	0.12

Table 17. Quantitative chemical composition (wt.%) of the glaze oxides determined by EDS analysis.

The slight shift of the phosphate band to 962 cm^{-1} in R9 is consistent with partial structural rearrangement of the calcium phosphate phase at 900 °C. At this temperature the glaze is fully liquid, air bubbles have been largely expelled, and Ca-P crystallites concentrated near the glaze surface become the dominant scattering centres governing opacity

Y7

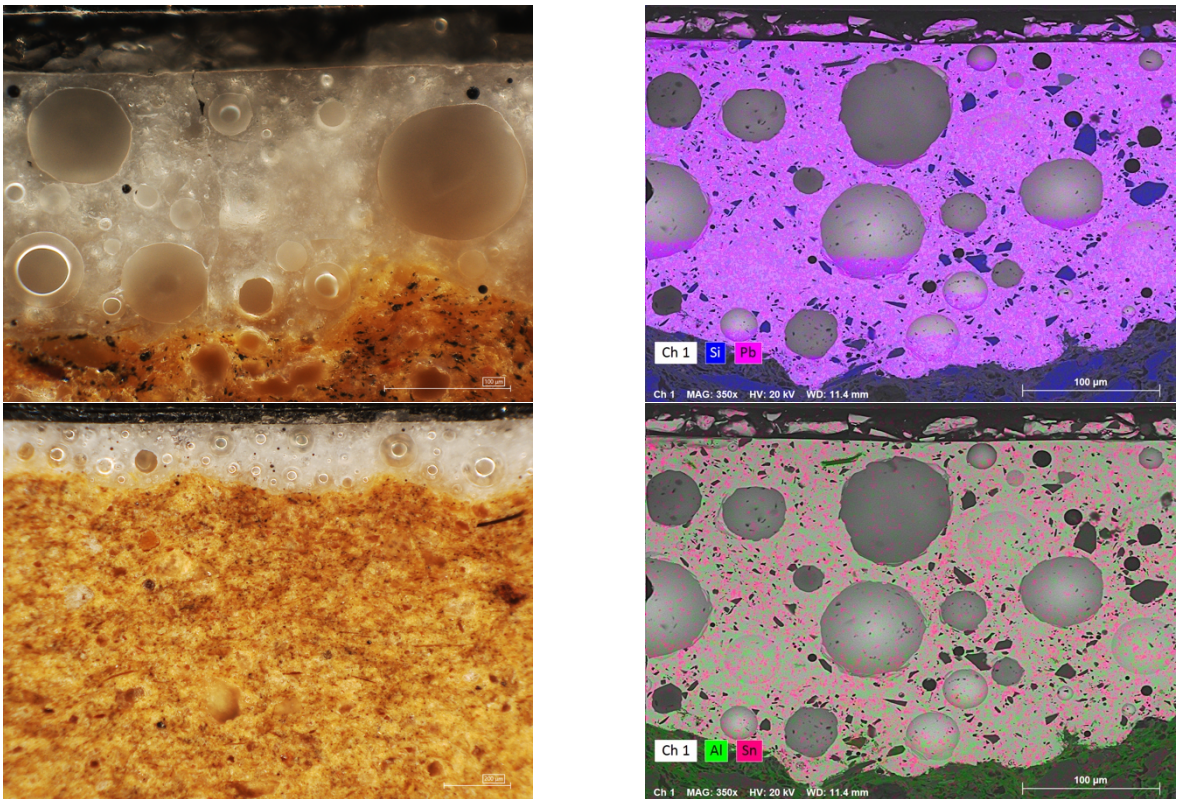


Figure 42. Digital Microscopy images at [700x high and 200x mid] magnification, and EDS elemental mapping of sample Y7.

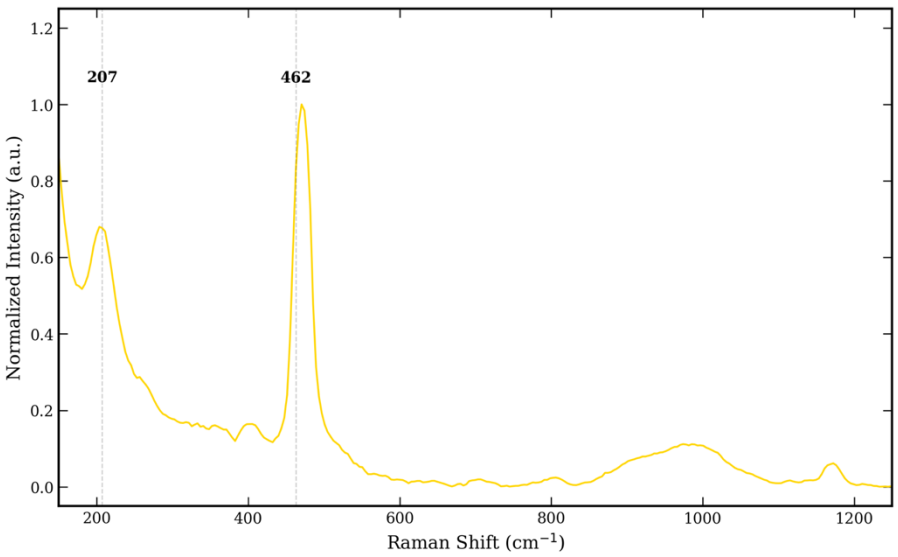


Figure 43. Raman spectrum of sample Y7

	AVR	SD
Na_2O	0.00	0.00
MgO	0.00	0.00
Al_2O_3	1.76	0.08
SiO_2	30.71	0.53
P_2O_5	0.00	0.00
K_2O	0.00	0.00
CaO	0.57	0.11
Fe_2O_3	0.18	0.06
PbO	57.36	0.31
TiO_2	0.00	0.00
SnO_2	2.32	0.44

Table 18. Quantitative chemical composition (wt.%) of the glaze oxides determined by EDS analysis.

The Raman spectrum of sample Y7 is dominated by the characteristic modes of crystalline α-quartz: the most intense band at 462 cm^{-1} (symmetric Si–O–Si stretching) and a secondary peak at 207 cm^{-1},

confirming the high crystallinity of the quartz component in the glaze batch. Consistent with the bone-ash-free formulation of the YELLOW recipe, no band is observed in the 960–970 cm^{-1} region; phosphorus is also undetectable by EDS (P = 0.00 wt% across all zones). The characteristic vibrational mode of cassiterite (SnO_2) near 633 cm^{-1} is not detectable, indicating an absence of crystalline precipitates. This is consistent with SEM-EDS observations, where no discrete crystals were observed, suggesting that the tin content (Sn ≈ 2.32 wt.%) remains entirely dissolved within the glassy matrix. The broad asymmetric band between 950 and 1100 cm^{-1} reflects the stretching vibrations of the silicate glass network (Si–O–Si units), confirming full vitrification of the glaze at the firing temperature used. The SiO_2/PbO molar ratio of the YELLOW recipe (0.635) is close to that of the RED/LT599 series (0.553), making Y7 a useful compositional comparator for assessing the effect of bone ash addition independently of changes in the lead–silica balance.

P8

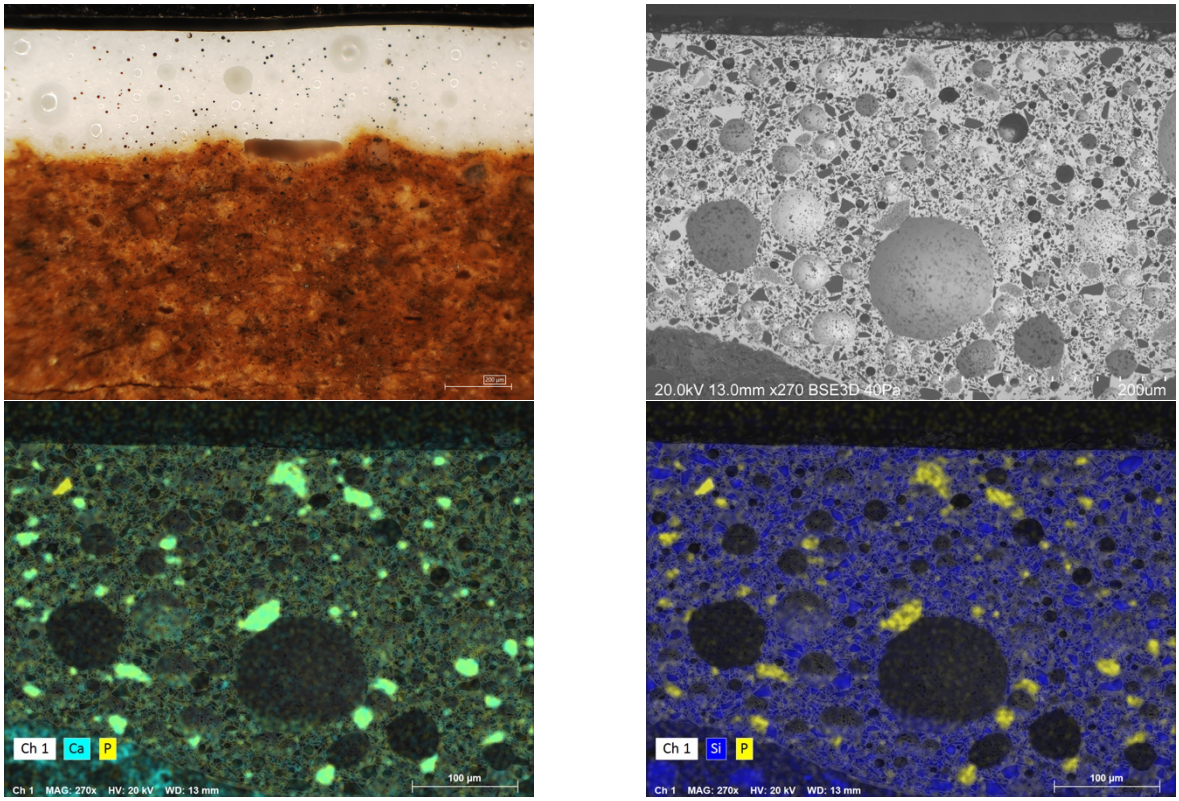


Figure 44. Digital Microscopy images at [200x] magnification, SEM-BSE image, and EDS elemental mapping of sample P8.

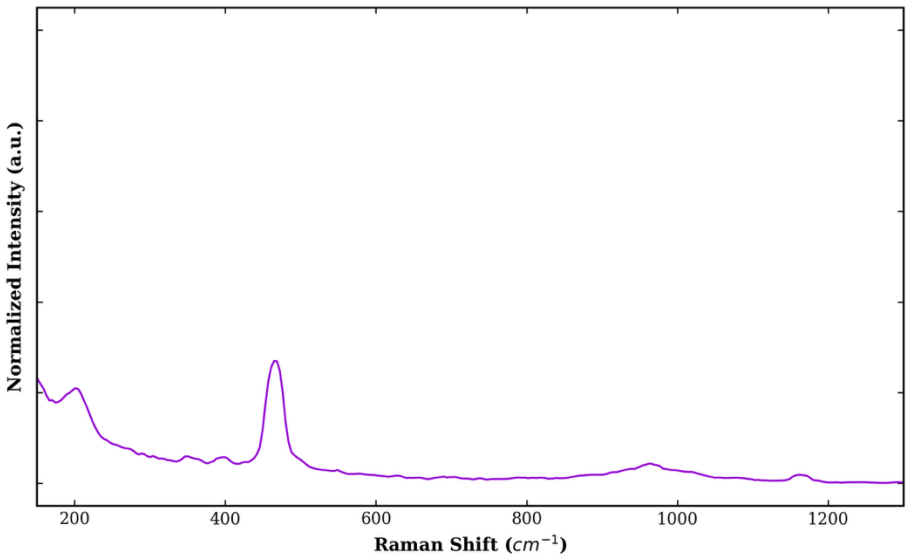


Figure 45. Raman spectrum of sample P8.

	AVR	SD
Na_2O	0.19	0.04
MgO	0.08	0.09
Al_2O_3	1.51	0.48
SiO_2	42.32	1.68
P_2O_5	1.98	2.45
K_2O	0.15	0.13
CaO	2.55	0.91
Fe_2O_3	0.27	0.12
PbO	41.19	0.79
TiO_2	0.00	0.00
SnO_2	1.72	0.17

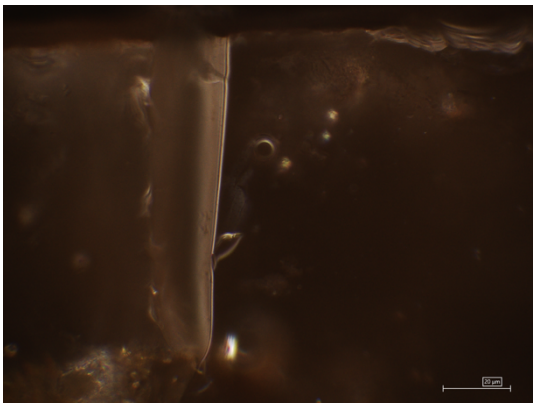
Table 19. Quantitative chemical composition (wt.%) of the glaze oxides determined by EDS analysis.

The Raman spectrum of sample P8 (PURPLE recipe, 800 °C) is dominated by medium quartz bands at 207 and 462 cm^{-1}, reflecting the high SiO_2/PbO molar ratio of the PURPLE formulation (0.783):

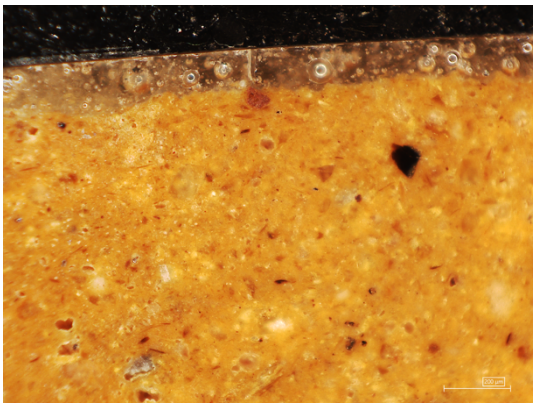
at this composition, large quantities of undissolved quartz remain in the incompletely fused matrix even at 800 °C. The phosphate-related band near 962–965 cm^{-1} is absent or unresolved, not because bone ash was omitted — it is present in the batch — but because the matrix has not achieved sufficient fluidity for the calcium phosphate to dissolve and reprecipitate as well-defined crystalline apatite. The absence of a sharp cassiterite peak near 633 cm^{-1} is consistent with the EDS data, which confirm that tin remains predominantly dissolved in the glassy fraction rather than precipitating as discrete SnO_2 particles. The SEM-BSE image confirms the abundance of residual quartz inclusions (dark irregular particles) dispersed throughout the partially fused lead-silicate matrix.

LT599

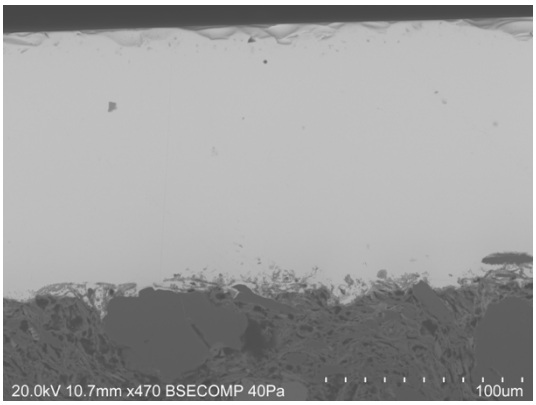
L7 mid 200x



L7 mid 200x



SEM-BSE L7



SEM-BSE L8

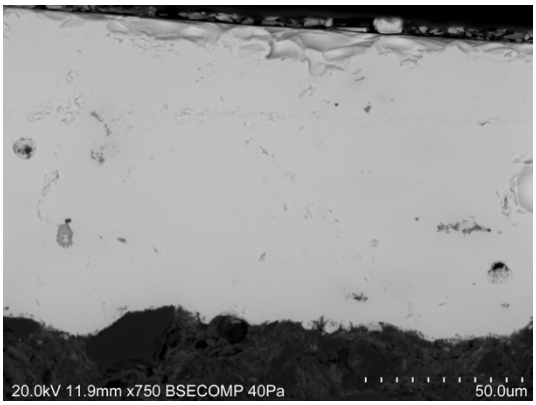


Figure 46. Digital Microscopy images at [200x] magnification, SEM-BSE images of samples L7 and L8

L7	AVR	SD	L8	AVR	SD	L9	AVR	SD
Na_2O	0.27	0.04	Na_2O	0.43	0.01	Na_2O	0.33	0.07
MgO	0.08	0.05	MgO	0.29	0.08	MgO	0.36	0.04
Al_2O_3	1.66	0.52	Al_2O_3	2.57	0.90	Al_2O_3	3.63	0.63
SiO_2	26.32	0.53	SiO_2	27.71	1.46	SiO_2	30.33	1.71
P_2O_5	0.00	0.00	P_2O_5	0.00	0.00	P_2O_5	0.00	0.00
K_2O	0.05	0.05	K_2O	0.33	0.11	K_2O	0.58	0.13
CaO	0.59	0.11	CaO	1.25	0.39	CaO	2.10	0.32
Fe_2O_3	0.22	0.05	Fe_2O_3	0.38	0.20	Fe_2O_3	0.66	0.10
PbO	65.49	0.95	PbO	61.25	3.06	PbO	54.37	2.85
TiO_2	0.07	0.01	TiO_2	0.00	0.00	TiO_2	0.00	0.00

Table 20.. Quantitative chemical composition (wt.%) of the glaze oxides determined by EDS analysis.

The LT599 series (bone-ash-free pure frit, SiO_2/PbO molar ratio 0.553) serves as the primary transparent-glaze control for the experimental matrix. The SEM-BSE images of L7 and L8 confirm that the glaze achieves good fusion at both 700 and 800 °C, with fewer residual —almost none— quartz inclusions than in the higher-molar-ratio recipes (BLUE, PURPLE). The EDS data show a clear compositional gradient from top to bottom, with Pb and Si highest in the upper glaze and Al, Fe, and Ca increasing toward the body-side interface, recording the progressive diffusion of ceramic-body components into the molten glaze. No phosphorus is detected at any point (P = 0.00 wt%), confirming the absence of bone ash and validating LT599 as the negative control against which P-bearing compositions are compared.

6. Discussion

6.1 Experimental recipes vs. theoretical targets

The degree of agreement between measured and calculated compositions was evaluated qualitatively through the distribution and abundance of residual quartz particles visible in the EDS maps. Quartz-rich regions indicate that not all silica entered the glassy matrix, signaling incomplete melting and, consequently, a larger deviation from the calculated oxide proportions. Among the five recipes, RED and LT599 displayed the fewest residual quartz inclusions in their maps, indicating that these two formulations approached their theoretical targets most closely after firing. This result is consistent with their shared low SiO_2/PbO molar ratio of 0.553, the lowest in the experimental series: a higher proportion of lead oxide acts as a powerful flux, lowering the liquidus temperature and promoting full dissolution of the silica component at all three firing temperatures.

The Yellow (Y) recipe, with a molar ratio of 0.635, and the Blue (B) recipe at 0.648 showed progressively larger populations of undissolved quartz, particularly at 700 °C. The Purple (P) recipe, at the highest molar ratio of 0.783, retained the most abundant quartz inclusions across all temperatures, confirming that higher silica loads require either higher temperatures or longer soaking times for complete incorporation.

The SiO_2/PbO molar ratio governs not only the degree of melting but also the intensity of whiteness in the finished glaze. Increasing silica relative to lead produced white glazes at all three firing temperatures, but at 700–800 °C the glaze was not yet fully fused: the white appearance at these lower temperatures is attributed primarily to light scattering by entrapped air bubbles rather than to the crystallisation of opacifying phases (see Section 6.3). At 900 °C the glaze matrix was sufficiently fluid for crystalline calcium phosphate and tin oxide clusters to nucleate and grow, becoming the dominant source of opacity.

EDS area analyses at top, middle, and bottom positions within the glaze layer confirmed a compositional gradient. In the RED recipe at 700 °C, the top zone yielded Pb = 60.93 wt%, Si = 25.71 wt%, Ca = 2.22 wt%; the bottom zone showed Pb = 56.24 wt%, Si = 29.38 wt%, Ca = 2.49 wt%. At 900 °C, the gradient steepened: top Pb = 56.06 wt%, Si = 22.47 wt%, Ca = 5.69 wt%; bottom Pb = 49.59 wt%, Si = 30.65 wt%, Ca = 3.58 wt%. The increase of Ca toward the glaze top at high temperature records the upward diffusion of calcium from the ceramic body and from bone ash dissolution, while Pb and Si are diluted by the incorporation of body-derived elements (Al, Fe, K).

The Yellow recipe, which contains no bone ash, provides a useful control: P was consistently 0.00 wt% across all zones and temperatures (mean Si = 30.71 wt%, Pb = 57.36 wt%, Ca = 0.57 wt%, P = 0.00 wt%), confirming that any phosphorus detected in the bone-ash-containing recipes derives exclusively from the added bone ash.

LT599 showed the highest Pb values at all temperatures (e.g., 700 °C top: Pb = 66.88 wt%, Si = 25.49 wt%; 900 °C bottom: Pb = 51.40 wt%, Si = 32.20 wt%) and zero phosphorus throughout, as expected for the bone-ash-free reference frit. The progressive enrichment in Al, Fe, and Ca from top to bottom in LT599 (e.g., at 900 °C: Al top = 2.91, bottom = 4.05 wt%) records diffusion from the clay body into the glaze, even in the absence of bone ash.

6.2 Bone ash identification

The identification of bone ash as an opacifier constitutes the central analytical result of this thesis. The approach combined Raman spectroscopy with SEM-BSE imaging and EDS spot analysis to produce complementary lines of evidence.

Raman spectra acquired on the glaze cross-sections of the bone-ash-containing replicas R7 (RED fired at 700 °C), R8 (RED at 800 °C), and R9 (RED at 900 °C) all displayed a prominent band centred at 962–965 cm^{-1}. This band corresponds to the symmetric stretching mode (ν_1) of the PO_4^{3-} tetrahedron in calcium phosphate phases, and it overlaps precisely with the Raman spectrum of the pure bone ash reference material used in the batch formulations. The peak was sharp and well-resolved in R7 and R8 (965 cm^{-1}), and slightly shifted to 962 cm^{-1} in R9, consistent with partial structural rearrangement of the phosphate phase at higher temperature.

The two bone-ash-free control recipes—LT599 and Yellow (Y)—did not exhibit any band in the 960–970 cm^{-1} region, regardless of firing temperature. This absence confirms the diagnostic specificity of the ~962–965 cm^{-1} Raman signature for bone-ash-derived calcium phosphate: the peak cannot arise from the lead-silicate glass matrix alone, nor from tin oxide, quartz, or any other component of the bone-ash-free formulations.

EDS quantification on the replicas provides compositional data that support the Raman identification. Sample R8 (800 °C) yielded a mean composition of Pb = 61.13 ± 1.35 wt%, Si = 25.35 ± 0.21 wt%, Ca = 2.10 ± 0.43 wt%, P = 0.69 ± 0.15 wt%, and Sn = 1.93 ± 0.64 wt%. Sample R9 (900 °C) gave Pb = 53.56 ± 3.47 wt%, Si = 26.95 ± 4.14 wt%, Ca = 4.24 ± 1.25 wt%, P = 1.80 ± 1.92 wt%, and Sn = 2.06 ± 0.12 wt%. Sample R7 (700 °C) showed Pb = 58.67 ± 2.35 wt%, Si = 26.80 ± 2.24 wt%, Ca = 2.65 ± 0.53 wt%, P = 0.73 ± 0.69 wt%, and Sn = 1.71 ± 0.54 wt%. The co-occurrence of

measurable P and Ca in all bone-ash-containing replicas, and their simultaneous absence in the controls, confirms that both elements originate from the added hydroxyapatite.

The Ca/P molar ratio serves as a quantitative bridge between the experimental replicas and the archaeological ceramics. In stoichiometric hydroxyapatite, Ca/P = 1.67. The experimental replicas display ratios that deviate from this theoretical value because calcium is contributed both by bone ash and by diffusion from the calcareous ceramic body, while phosphorus derives solely from bone ash. This divergence is itself informative: any archaeological sample that shows measurable phosphorus in its glaze, coupled with a Ca/P ratio exceeding the hydroxyapatite stoichiometry, is consistent with a production technology that employs bone ash as an additive to a calcareous-body ceramic.

SEM-BSE images of the bone-ash-containing replicas revealed two distinct populations of inclusions: high-contrast (bright) particles attributable to tin-oxide-rich clusters, and low-contrast (dark) particles whose spot analyses returned elevated Ca and P signals, consistent with residual or partially dissolved bone ash grains. The low-contrast particles were absent from LT599 and Y, reinforcing the assignment of these inclusions to bone-ash-derived material.

The same characteristic Raman band at ~962–965 cm^{-1} was also detected in certain archaeological samples examined in this study. The presence of this band, which corresponds significantly to the reference material (bone ash), in both the experimental replicas and the historical glazes constitutes converging evidence that Islamic potters employed bone ash as a deliberate opacifier in lead-glazed ceramic production. This finding is not merely an experimental artefact: the spectroscopic overlap — shown in Figure 47— between replicas and archaeological objects demonstrates continuity of raw material choice across the experimental reconstruction and the original manufacturing tradition.

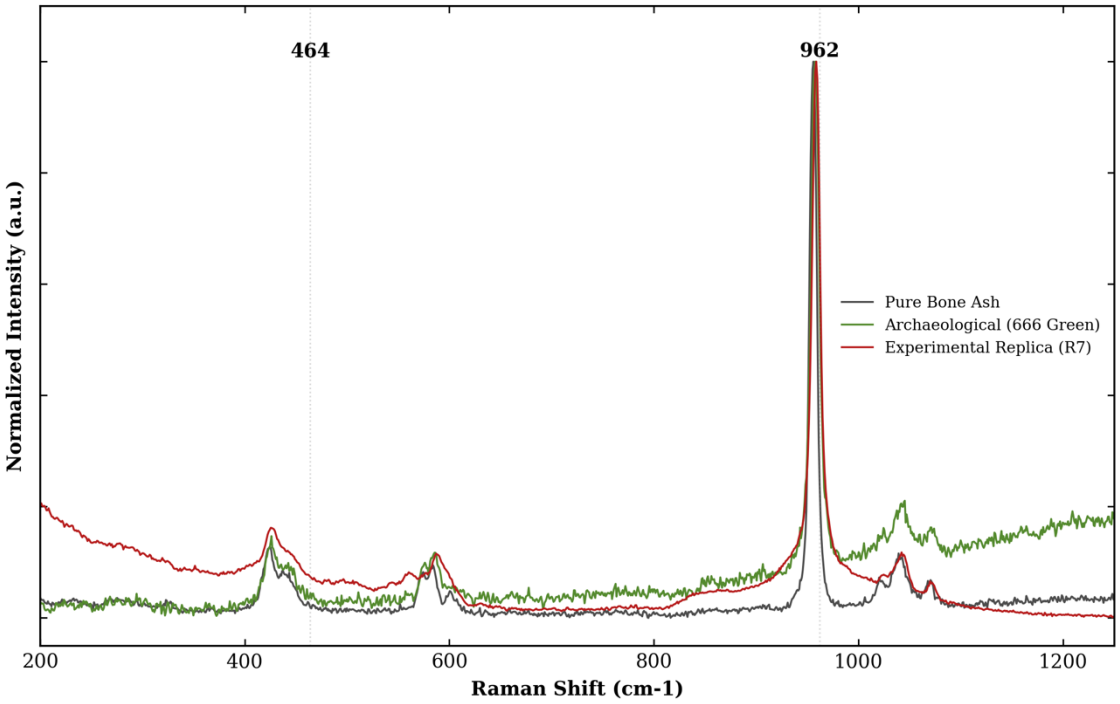


Figure 47. Overlaid Raman spectra comparison between Pure Bone Ash (black), Archaeological sample CRVM666 (green), and Experimental Replica R7 (red). The spectra are normalized and corrected for instrumental shift (-6 cm^{-1}). The diagnostic peak for hydroxyapatite is highlighted at 962 cm^{-1}.

The high degree of overlap between the three spectra suggests that the crystalline structure of the hydroxyapatite remains stable even after being incorporated into the disordered silicate glass matrix.

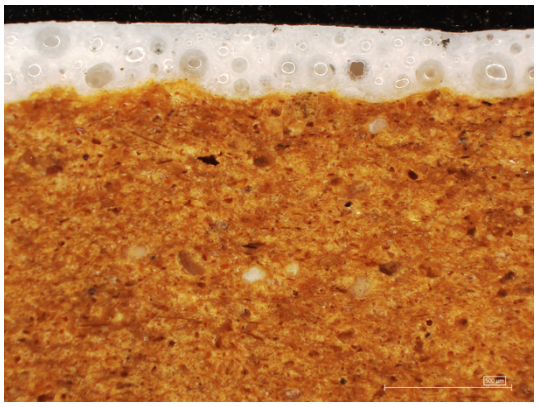
Specifically:

- Mineralogical Stability: The presence of the 962 cm^{-1} peak in both the archaeological and experimental samples indicates that the calcination and subsequent firing processes did not lead to the complete dissolution of the phosphate phase, which remains the key factor for the glaze's opacity.
- Glass-Ceramic Interaction: While the Pure Bone Ash exhibits a narrower Full Width at Half Maximum (FWHM), the slightly broader peaks in CRVM666 and R7 reflect the interaction between the crystalline phosphates and the amorphous glass, a typical characteristic of complex glass-ceramic systems.
- Methodological Accuracy: The systematic correction of the instrumental bias ensured that the experimental data aligns perfectly with theoretical values, providing a robust basis for the comparative analysis.

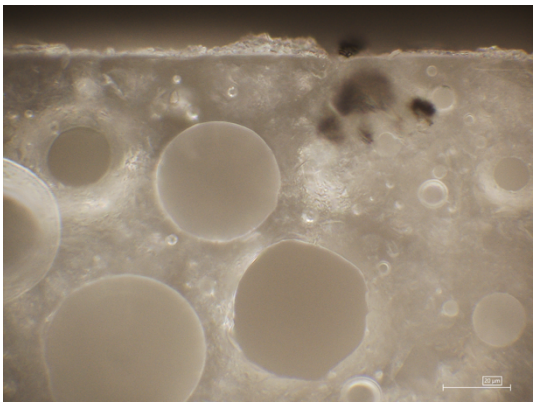
This evidence strongly supports the technological hypothesis regarding the intentional addition of calcium phosphates to achieve the desired aesthetic and functional properties in the production of historical glazes.

6.3 Opacification mechanisms

The mechanism of opacification in lead glazes containing bone ash and tin oxide varies as a function of firing temperature. At 700 °C, the glaze matrix is not yet fully molten. The white visual appearance of the 700 °C samples is attributed predominantly to the entrapment of air bubbles within the viscous, partially fused glaze. SEM-BSE images of the 700 °C cross-sections confirm abundant spherical voids distributed throughout the glaze layer. These bubbles scatter incident light effectively, producing a diffuse white reflectance that mimics true opacification but is not caused by crystalline scattering centres as shown in the following images.



mid 140x



high 2000x

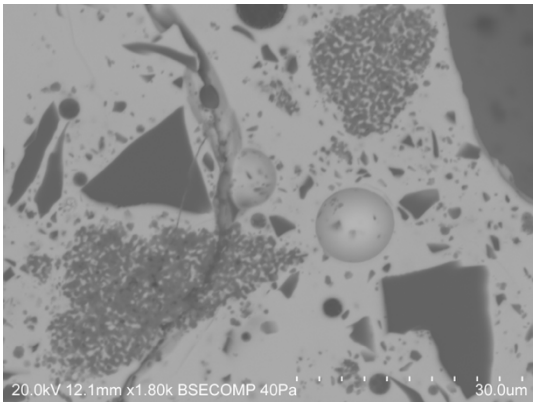
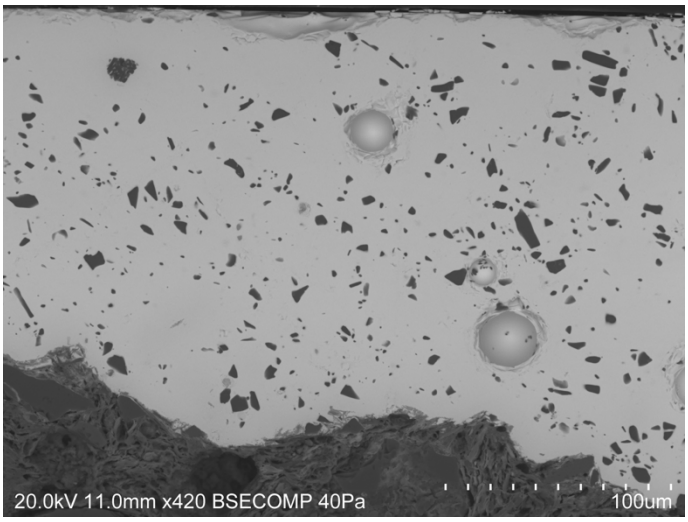
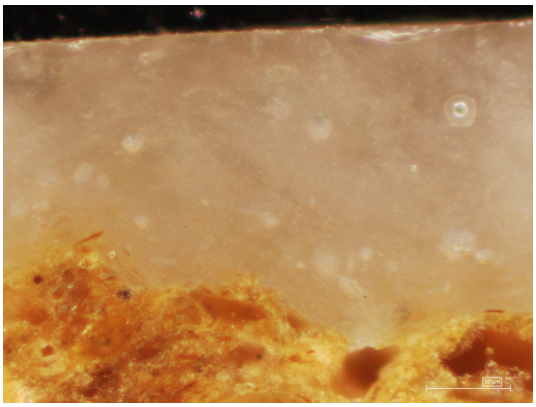


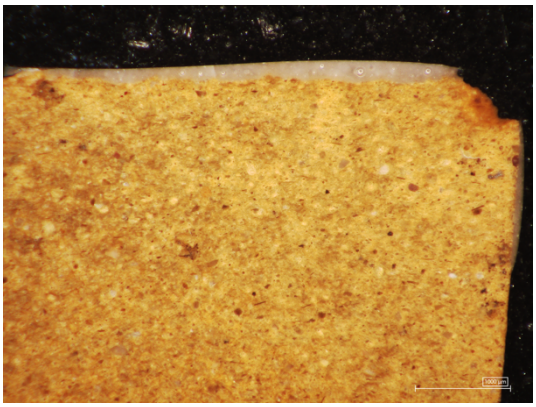
Figure 48. Digital Microscopy image at [140x] magnification of mid B7 and high B7 at [2000x] magnification, SEM-BSE image of B7 detail.

At 800 °C, the glaze begins to achieve full fusion. Bubble populations decrease, and the first crystalline opacifying particles become visible in the BSE images: fine calcium phosphate crystallites (identified by their Raman signature at 962–965 cm^{-1}) and tin oxide clusters (high-contrast BSE particles confirmed by EDS). Both phases contribute to opacity through light scattering at the

interface between crystallites and the surrounding glassy matrix. The combined effect of residual bubbles and incipient crystallisation produces a transitional opacification regime.







mid 100x wide 50x

Figure 49. SEM-BSE image of Y8 sample, Digital Microscopy image at [100x] magnification of mid Y8 and at [50x] magnification.

At 900 °C, the glaze is fully liquid. Air bubbles have largely been expelled, and crystalline calcium phosphate and tin oxide become the dominant scattering centres. The opacity is now governed by the number density, size, and spatial distribution of these crystallites. EDS data confirm that calcium and phosphorus are enriched in the upper portion of the glaze at 900 °C (e.g., RED 900 °C top: Ca = 5.69 wt%, P = 4.00 wt%), indicating that calcium phosphate crystallites concentrate near the surface where they are most effective as opacifiers, as it also visible in the DM and SEM images below.

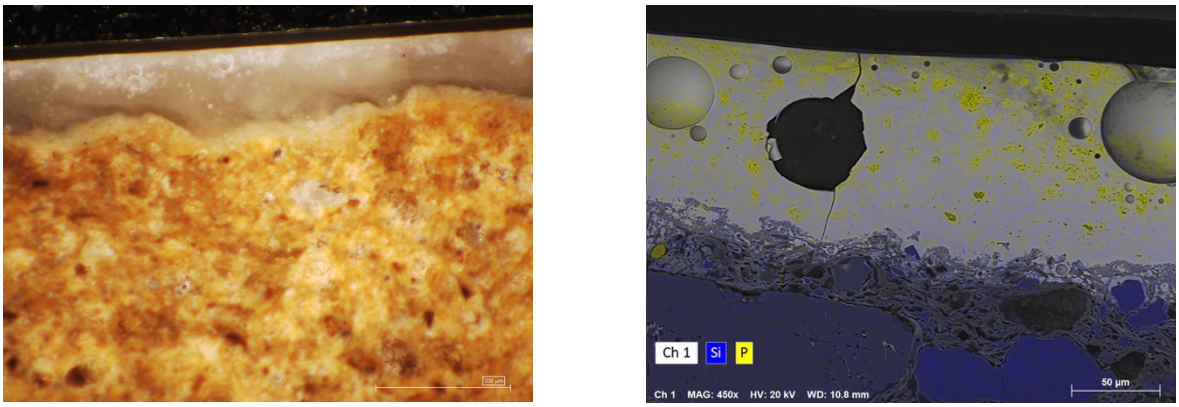


Figure 50. Digital Microscopy image at [400x] magnification of mid R9 sample, and EDS elemental mapping.

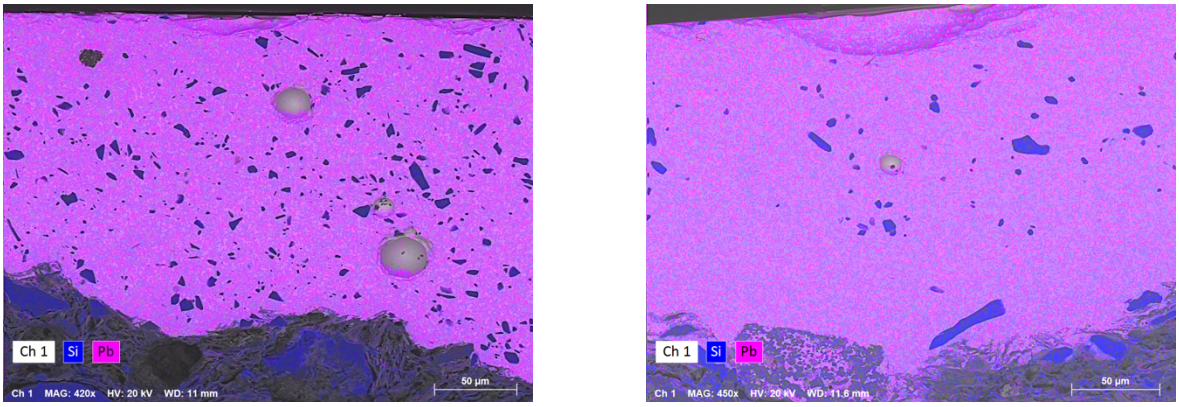


Figure 51. EDS elemental mapping comparing samples Y8 and Y9, demonstrating a significant decrease in crystallite density as firing temperature increases.

Archaeological samples display coarse crystalline inclusions that produce both opacity and optical discontinuity—visible as a granular, heterogeneous white surface rather than a smooth opaque layer. This coarsening is consistent with slower cooling rates in wood-fired kilns compared to the laboratory muffle furnace used for the replicas, which allows longer crystal growth times.

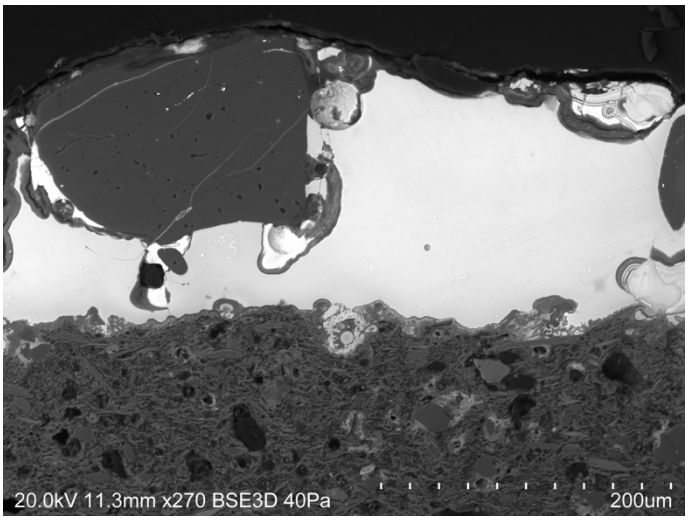


Figure 52. SEM-BSE image of archaeological sample

A working hypothesis for future investigation is that extending the soaking time at low temperatures (700 °C) could eliminate air bubbles without raising the firing temperature, thereby decoupling bubble-driven whiteness from true crystalline opacification. If confirmed, this would provide a route to distinguishing temperature from time effects in the archaeological record.

The EDS data also reveal that effective whitening by tin oxide requires substantially higher Sn concentrations than the batch formulation predicts. In the YELLOW recipe, the mean Sn content across Y7, Y8, and Y9 ranges from 1.73 to 2.92 wt%, yet the optical whiteness remains moderate. This observation suggests that a large fraction of the added SnO_2 remains dissolved in the lead-silicate glass rather than precipitating as discrete cassiterite (SnO_2) particles. This is confirmed by the absence of the diagnostic peak of casserite in the Raman spectrum (see previous Chapter). Effective tin-based opacification therefore demands a higher initial tin loading than simple stoichiometric calculation would suggest—a finding with direct implications for interpreting tin concentrations in archaeological glazes.

6.4 Glaze–body interface and digestion process

The interaction between the lead glaze and the ceramic body during firing produces a reaction zone at their interface whose morphology and thickness encode information about firing conditions and sequence. This process, termed “digestion,” involves three sequential stages: decomposition of clay-body phases (dehydroxylation of clay minerals, decarbonation of calcite), diffusion of elements across the interface, and formation of new crystalline phases within the reaction zone [53].

EDS elemental maps and line profiles across the glaze–body interface of the experimental replicas, as well as those of the archeological samples, confirm this sequence. Elements originating from the

ceramic paste—Al, Fe, Ca, K—increase progressively from the glaze top toward the body. Conversely, Pb and Si, the primary glaze components, decrease toward the interface as they are diluted by the influx of body-derived species. Na remains comparatively stable across the profile, consistent with its relatively low mobility in these systems.

Table 21. Figure 53

		sem	**OXIDES**	C	Na	Mg	Al	Si	P	K	Ca	Fe	Pb	Ti	Sn
YELLOW	700	area 1	TOP		0.00	0.00	1.74	30.79	0.00	0.00	0.46	0.15	57.02	0.00	2.31
		area 2	MIDDLE		0.00	0.00	1.69	30.15	0.00	0.00	0.59	0.13	57.62	0.00	2.76
		area 3	BOTTOM		0.00	0.00	1.85	31.20	0.00	0.00	0.67	0.24	57.44	0.00	1.88
YELLOW	800	area 1	TOP		0.22	0.09	8.69	27.49	0.00	0.11	0.43	0.13	55.08	0.05	1.73
		area 2	MIDDLE		0.10	0.00	1.79	34.02	0.00	0.13	0.59	0.20	54.10	0.00	2.40
		area 3	BOTTOM		0.28	0.27	2.46	35.02	0.00	0.33	1.25	0.41	51.78	0.16	2.00
YELLOW	900	area 1	TOP		0.00	0.00	1.72	30.92	0.00	0.00	0.74	0.16	58.63	0.00	1.77
		area 2	MIDDLE		0.00	0.00	2.06	31.37	0.00	0.00	0.92	0.30	56.65	0.00	2.92
		area 3	BOTTOM		0.00	0.00	3.58	32.68	0.00	0.00	1.60	0.78	53.95	0.00	1.81

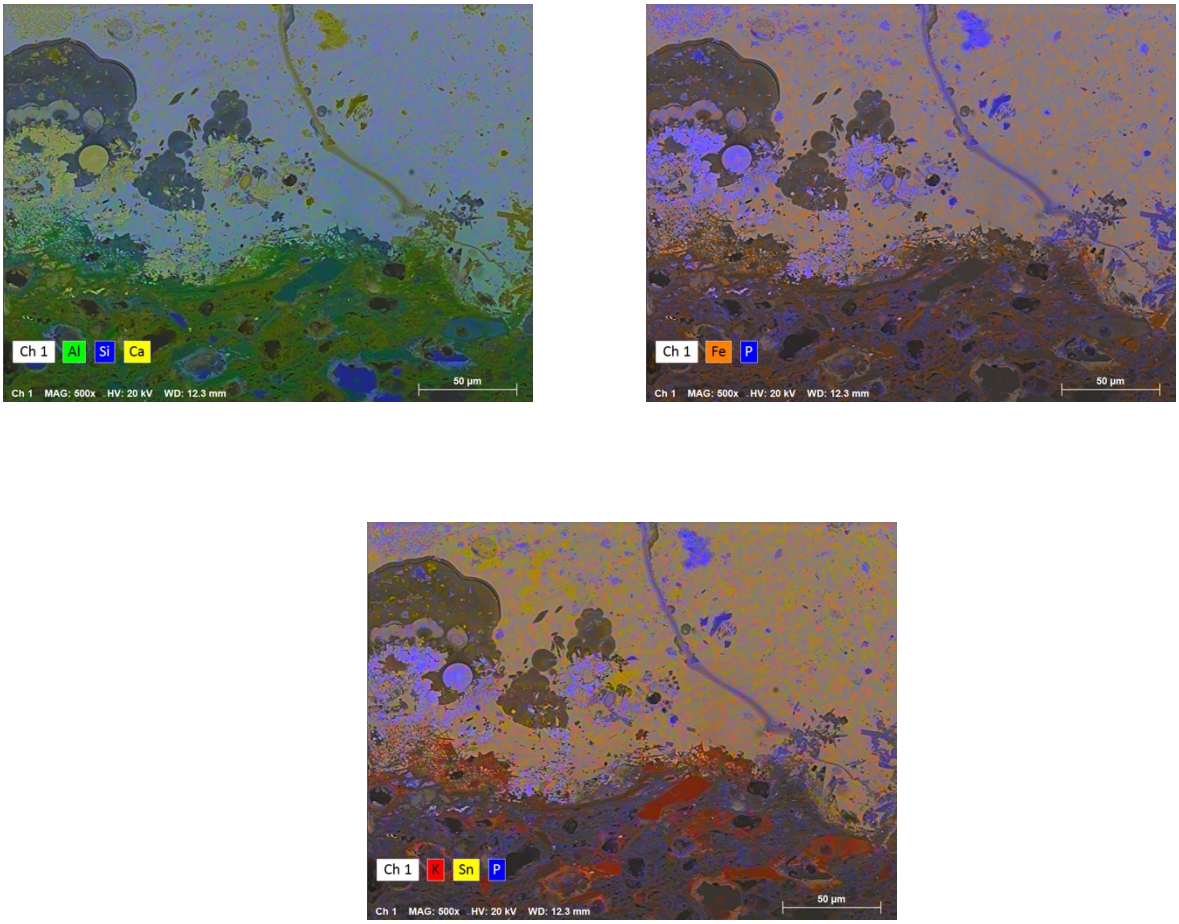


Figure 54. EDS elemental mappings of sample CRVM666.

In the RED recipe, the compositional gradient becomes more pronounced with increasing firing temperature. At 700 °C, the bottom zone shows only a modest enrichment in Al (3.21 wt%) relative to the top (1.63 wt%). At 900 °C, the bottom zone reaches Al = 5.35 wt% while the top remains at 1.58 wt%, indicating that diffusion distances increase with temperature. Ca follows the same trend: top values of 2.22 wt% (700 °C) and 5.69 wt% (900 °C) reflect the progressive dissolution of calcareous body components into the glaze.

At temperatures above 900 °C with slow cooling rates (20 °C/h), the interface can exceed 200 μm. Under these conditions, diffusion is complete and the glaze composition approaches homogeneity after approximately 4 hours at maximum temperature. The crystallites formed within the reaction zone are also larger under slow cooling, because extended time at elevated temperature permits Ostwald ripening.

The mineralogy of the interface crystallites depends on the clay body composition. Kaolinitic bodies act as stabilisers, suppressing crystallite growth at the interface and producing a narrow, well-defined reaction zone. Illitic clays, by contrast, favour the crystallisation of K–Pb feldspars due to the release of potassium during firing. Carbonate-rich pastes promote the formation of Ca-rich pyroxenes, which float upward into the glaze because their density is lower than that of the surrounding lead-silicate melt. This buoyancy-driven transport explains the enrichment of Ca-bearing crystalline phases in the upper portion of the glaze observed in several replicas and archaeological samples.

6.5 Comparison with archaeological samples

The quantitative oxide data extracted from the SEM-EDS measurements of the archaeological samples—623, 666, and 1668— across multiple glaze zones, permit a direct comparison with the experimental replica series.

Sample 666 provides the most informative case for bone ash identification. The black zone of sample 666 yielded a mean P = 3.01 wt%, Ca = 6.67 wt%, with Si = 26.85 wt% and Pb = 49.39 wt%. The green zone gave P = 2.04 wt%, Ca = 5.27 wt%, Pb = 53.82 wt%. The whie zone showed P = 0.00 wt%, Ca = 3.39 wt%, Pb = 40.69 wt%, Si = 39.75 wt%. The “under” zone returned P = 0.00 wt%, Ca = 3.72 wt%, Pb = 48.96 wt%.

Sample 623 shows a contrasting pattern: P = 0.00 wt% across all zones (green mean: Si = 34.21 wt%, Ca = 2.35 wt%, Pb = 47.56 wt%; trs under: Ca = 3.61 wt%, Pb = 45.37 wt%; trs: Si = 38.19 wt%, Pb = 44.72 wt%). The absence of phosphorus in all glaze areas of sample 623 indicates that bone ash was ipotetically used in very little, non-detectable quantities, which explains why no Raman spectra

were collected from this sample: even if some areas that contain P were identified by EDS mapping, we were not able to extract a consistent Raman signal.

Sample 1668. The black zone yielded P = 0.00 wt%, Ca = 2.24 wt%, Pb = 51.70 wt%, Sn = 1.89 wt%. The green zone: P = 0.00 wt%, Ca = 2.21 wt%, Pb = 51.63 wt%. The bianco zone: P = 0.00 wt%, Ca = 1.77 wt%, Pb = 51.18 wt%, Sn = 2.77 wt%. The SiO_2/PbO molar ratios for 1668 (nero: 0.0055; verde: 0.0057; bianco: 0.0058) are closely clustered, indicating a relatively homogeneous glaze composition consistent with careful batch control.

Contamination effects are visible in the archaeological glazes, particularly in secondary (undecorated) glaze areas. The verde and nero zones of sample 666 show elevated Ca and P from opacifier residues, along with higher Fe and Al signals from body-derived contamination, consistent with the digestion process described in Section 6.4. The secondary glaze areas of archaeological ceramics are expected to accumulate more contamination because they are typically applied less thickly and are more susceptible to diffusion from the body.

The SiO_2/PbO molar ratios calculated for the archaeological samples (sample 623: verde 0.0057, under 0.0054, trs 0.0064; sample 666: nero 0.0045, verde 0.0043, under 0.0053, bianco 0.0066; sample 1668: nero 0.0055, verde 0.0057, under 0.0059, bianco 0.0058) fall within a range that brackets the experimental recipes (LT599 and RED: 0.553; Y: 0.635; B: 0.648; P: 0.783). The lower molar ratios observed in the archaeological nero and verde zones of sample 666 are consistent with lead-rich, silica-poor formulations optimised for low melting points and good wetting on coloured decoration.

The Ca/P molar ratio in the experimental replicas and its overlap with values measured in the archaeological glazes containing phosphorus provides the most direct chemical evidence for the use of bone ash. In sample 666, the black zone Ca/P ratio substantially exceeds the hydroxyapatite stoichiometry of 1.67, consistent with the superimposition of body-derived calcium on bone-ash-derived phosphorus—the same pattern observed in the experimental replicas. The convergence of Raman spectroscopic evidence (the ~962–965 cm^{-1} band present in both replicas and archaeological objects) and chemical evidence (Ca/P ratios, P distribution) demonstrates that Islamic potters in this production tradition used bone ash as a raw material for glaze opacification.

6.6 Expected vs. observed outcomes

Several outcomes diverged from initial expectations based on the theoretical framework.

First, the batch calculation predicted that the added SnO_2 (0.188 g per 7.5 g batch) would provide effective white opacification across all temperatures. However the experimental data show that the

measured Sn concentrations (R7: 1.71 wt%, R8: 1.93 wt%, R9: 2.06 wt%) correspond to modest opacity, and that a substantial fraction of tin remains dissolved in the glass. Effective tin-based whitening requires significantly higher Sn loadings than the initial formulation supplied—a finding that has direct relevance for interpreting Sn/Pb ratios in archaeological analyses, where low Sn values should not be taken as evidence against the intentional use of tin as an opacifier.

Second, the dominant opacification mechanism at 700 °C was not crystalline scattering, as initially anticipated, but air bubble entrapment. This was unexpected because the theoretical model assumed full fusion at all three temperatures. The persistence of a viscous, bubble-rich matrix at 700 °C indicates that the LT599 frit, despite its high lead content, does not achieve complete vitrification at this temperature within the 2-hour soaking time used in the experiments.

Third, the compositional gradient from top to bottom of the glaze was steeper than expected at 900 °C, with Al reaching 5.35 wt% in the bottom zone of the RED recipe—more than three times the top value. This indicates that the digestion of the clay body proceeds much faster than anticipated at high temperature, and that any bulk EDS analysis of an archaeological glaze that does not account for this gradient will underestimate the true Pb and Si content of the original batch and overestimate the contribution of body-derived elements.

Fourth, the Purple recipe (P), formulated with the highest SiO_2/PbO ratio of 0.783, retained abundant undissolved quartz at all temperatures. The Si values for Purple (mean ~42–45 wt% across zones) remained the highest of any recipe, and the Pb values the lowest (~39–44 wt%). This confirms that pushing the molar ratio above ~0.65 in these lead-silicate systems results in incomplete melting under the firing conditions tested, and that the practical upper limit for a well-fused glaze lies between 0.65 and 0.78.

These discrepancies between prediction and observation underscore the value of experimental replication as a tool for archaeometric interpretation. Theoretical batch calculations, while essential for experimental design, cannot capture the kinetic constraints, diffusion phenomena, and phase-equilibrium behaviour that govern the real microstructure of a fired glaze. The experimental replicas produced in this study provide a calibrated reference framework that accounts for these effects.

Conclusions

This thesis aimed to reconstruct the glazing technology of the Islamic "green and brown" ceramics recovered at Mértola by combining chemical and microstructural characterisation of archaeological samples with a laboratory-based experimental replica programme. The work addressed three interconnected research questions, and the results allow the following conclusions to be drawn.

Regarding the identification of opacifying agents, the combined evidence from Raman spectroscopy, SEM-BSE imaging, and EDS analysis demonstrates that bone ash was used as a deliberate opacifier. The diagnostic Raman band at ~962–965 cm^{-1}, corresponding to the ν_1 PO_4^{3-} stretching mode of calcium phosphate, was detected in the experimental replicas as well as in archaeological samples CRVM666 and CRVM1668. In sample CRVM623, no consistent Raman signal could be extracted. It must be noted, however, that the identification of bone-ash-derived calcium phosphate particles by micro-Raman proved challenging across all archaeological samples: the phosphate crystallites are extremely fine and dispersed within the glaze matrix, making them difficult to target with the laser spot. Raman spectroscopy, while diagnostic when a signal is obtained, is therefore not the most straightforward technique for this purpose. Complementary SEM-EDS data provided a systematic confirmation: the co-occurrence of phosphorus and calcium in the coloured glaze zones — and their absence in bone-ash-free areas — together with Ca/P molar ratios exceeding the hydroxyapatite stoichiometry of 1.67, consistently support the presence of apatite-derived material in the glaze. This finding represents, to the best of the author's knowledge, the first experimental demonstration that bone ash was employed as an alternative to tin oxide in the Islamic glazed ceramic tradition .

Concerning the role of the lead-to-silica molar ratio, the experimental results confirm that the SiO_2/PbO ratio governs both quartz dissolution and the resulting whiteness of the glaze. Lower ratios (0.553) achieved nearly complete melting, whereas higher ratios (up to 0.783) retained abundant undissolved quartz even at 900 °C, placing the practical upper limit for a well-fused glaze between approximately 0.65 and 0.78. The opacification mechanism was also shown to be temperature-dependent: at 700 °C the white appearance derives mainly from entrapped air bubbles in a partially fused matrix, while at 900 °C crystalline calcium phosphate and tin oxide become the dominant scattering centres.

As for the position of the Mértola ceramics within the broader Al-Andalus tradition, the data suggest a local technological adaptation: the use of bone ash likely reflects the loss of reliable access to tin sources in the north of the Iberian Peninsula, while the general glaze formulation — a high-lead, low-silica system on calcareous bodies — remains consistent with the wider Islamic glazing framework,

indicating that core technological knowledge was preserved even as specific raw materials were substituted.

Taken together, these results demonstrate the value of integrating analytical archaeometry with experimental archaeology. The replicas provided a calibrated reference framework that captures kinetic and diffusion effects beyond the reach of theoretical calculations alone. Future work should extend the programme to coloured glaze formulations, explore soaking-time effects on bubble elimination at low temperatures, and expand the archaeological sample set to assess whether the use of bone ash is specific to Mértola or part of a wider regional practice.

References

[1] R. B. Heimann and M. Maggetti, “The struggle between thermodynamics and kinetics: Phase evolution of ancient and historical ceramics,” vol. 20, pp. 233–281, Aug. 2019, doi: 10.1180/EMU-notes.20.6.

[2] L. Teodorescu *et al.*, “Characterization of Archaeological Artefacts Using Methods Specific to Materials Science: The Case Study of Dacian Ceramics from 2nd c. BC to 1st c. AD,” *Materials*, vol. 14, no. 14, p. 3908, Jan. 2021, doi: 10.3390/ma14143908.

[3] M. Vendrell, J. Molera, and M. S. Tite, “Optical Properties of Tin-Opacified Glazes,” *Archaeometry*, vol. 42, no. 2, pp. 325–340, 2000, doi: 10.1111/j.1475-4754.2000.tb00885.x.

[4] E. Salinas and T. Pradell, “The secret is quartz: technology of production of an eleventh-twelfth century western Mediterranean polychrome glazed ware,” *Archaeol Anthropol Sci*, vol. 16, no. 8, p. 135, Jul. 2024, doi: 10.1007/s12520-024-02040-2.

[5] O. Watson, “Revisiting Samarra: the Rise of Islamic Glazed Pottery,” *Beitr. zur Islam. Kunst Archäol.*, vol. 4, pp. 125–144, Jan. 2014, doi: 10.29091/9783954906024/010.

[6] C. Camara, M. J. Gonçalves, J. A. P. Mirão, S. Gómez, and M. Beltrame, “MORPHO-FUNCTIONAL, DECORATIVE AND PETROGRAPHIC STUDY OF ISLAMIC GLAZED/UNGLAZED CERAMICS FROM THE CITIES OF ÉVORA, MÉRTOLA AND SILVES”.

[7] C. A. Camara, M. J. Gonçalves, J. A. P. Mirão, S. G. Martínez, and M. Beltrame, “High-Lead Glazed Ceramic Production in Western Iberia (Gharb al-Andalus) between the 10th and Mid-13th Centuries: An Approach from the City of Évora (Portugal),” *Ceramics*, vol. 6, no. 4, pp. 2213–2242, Dec. 2023, doi: 10.3390/ceramics6040135.

[8] R. B. Mason and M. S. Tite, “The Beginnings of Tin-Opacification of Pottery Glazes,” *Archaeometry*, vol. 39, no. 1, pp. 41–58, 1997, doi: 10.1111/j.1475-4754.1997.tb00789.x.

[9] “Characterization and Elemental Quantification of Natural Hydroxyapatite Produced from Cow Bone - Akindoyo - 2019 - Chemical Engineering & Technology - Wiley Online Library.” Accessed: Apr. 13, 2026. [Online]. Available: https://onlinelibrary.wiley.com/doi/10.1002/ceat.201800636

[10] A. Silvestri, F. Nestola, and L. Peruzzo, “Multi-methodological characterisation of calcium phosphate in late-Antique glass mosaic tesserae,” *Microchemical Journal*, vol. 124, Oct. 2015, doi: 10.1016/j.microc.2015.10.026.

[11] M. R. Mesquida, M. Vendrell, and J. Pérez-Arantegui, “Lustre Recipes from A Medieval Workshop in Paterna,” *Archaeometry*, vol. 43, no. 4, p. 455, 2001, doi: 10.1111/1475-4754.00028.

[12] R. B. Mason and M. S. Tite, “The Beginnings of Tin-Opacification of Pottery Glazes,” *Archaeometry*, vol. 39, no. 1, pp. 41–58, 1997, doi: 10.1111/j.1475-4754.1997.tb00789.x.

[13] M. Tite, “Revisiting the beginnings of tin-opacified Islamic glazes”.

[14] E. Salinas, J. D. Juan, J. M. Piñero, M. T. Casal, N. Schibille, and T. Pradell, “From Glass to Glaze in al-Andalus: Local Invention and Technological Transfer,” *European Journal of Archaeology*, vol. 25, no. 1, pp. 22–41, Feb. 2022, doi: 10.1017/eaa.2021.23.

[15] E. Salinas, “Entanglements in the western Islamic lands: Early glazed ceramics of al-Andalus,” in *Explorations in Islamic Archaeology*, Brepols Online, 2025, pp. 129–154. doi: 10.1484/M.MPAS-EB.5.150668.

[16] “(PDF) Ceramic technology. How to characterise ceramic glazes,” *ResearchGate*, doi: 10.1007/s12520-020-01136-9.

[17] “Muslim Spain and Portugal: A Political History of al-Andalus,” Routledge & CRC Press. Accessed: Apr. 13, 2026. [Online]. Available: https://www.routledge.com/Muslim-Spain-and-Portugal-A-Political-History-of-al-Andalus/Kennedy-Kennedy/p/book/9780582495159

[18] H. (Hugh N.) Kennedy, *The Prophet and the age of the Caliphates : the Islamic Near East from the sixth to the eleventh century*. Harlow, England ; New York : Pearson/Longman, 2004.

Accessed: Apr. 13, 2026. [Online]. Available: http://archive.org/details/prophetageofcali0000kenn_n8u3
[19] "Revisiting Samarra: the Rise of Islamic Glazed Pottery | Request PDF," *ResearchGate*, Jan. 2026, Accessed: Mar. 16, 2026. [Online]. Available: https://www.researchgate.net/publication/285087932_Revisiting_Samarra_the_rise_of_Islamic_glazed_pottery
[20] M. Matin, M. Tite, and O. Watson, "On the origins of tin-opacified ceramic glazes: New evidence from early Islamic Egypt, the Levant, Mesopotamia, Iran, and Central Asia," *Journal of Archaeological Science*, vol. 97, pp. 42–66, Sep. 2018, doi: 10.1016/j.jas.2018.06.011.
[21] M. Matin, "Tin-based opacifiers in archaeological glass and ceramic glazes: a review and new perspectives," *Archaeol Anthropol Sci*, vol. 11, no. 4, pp. 1155–1167, Apr. 2019, doi: 10.1007/s12520-018-0735-2.
[22] M. Matin, M. Tite, and O. Watson, "On the origins of tin-opacified ceramic glazes: New evidence from early Islamic Egypt, the Levant, Mesopotamia, Iran, and Central Asia," *Journal of Archaeological Science*, vol. 97, pp. 42–66, Sep. 2018, doi: 10.1016/j.jas.2018.06.011.
[23] R. B. Mason and M. S. Tite, "The Beginnings of Tin-Opacification of Pottery Glazes," *Archaeometry*, vol. 39, no. 1, pp. 41–58, 1997, doi: 10.1111/j.1475-4754.1997.tb00789.x.
[24] E. Salinas and T. Pradell, "The introduction of the glaze in al-Andalus: Technological waves and Oriental influences".
[25] E. Salinas, "Entanglements in the western Islamic lands: Early glazed ceramics of al-Andalus," in *Medieval and Post-Medieval Mediterranean Archaeology*, vol. 7, J. Vroom and H. Nol, Eds., Turnhout, Belgium: Brepols Publishers, 2025, pp. 129–154. doi: 10.1484/M.MPAS-EB.5.150668.
[26] E. Salinas, T. Pradell, and J. Molera, "Glaze production at an early Islamic workshop in al-Andalus," *Archaeol Anthropol Sci*, vol. 11, no. 5, pp. 2201–2213, May 2019, doi: 10.1007/s12520-018-0666-y.
[27] E. Salinas, J. D. Juan, J. M. Piñero, M. T. Casal, N. Schibille, and T. Pradell, "From Glass to Glaze in al-Andalus: Local Invention and Technological Transfer," *European Journal of Archaeology*, vol. 25, no. 1, pp. 22–41, Feb. 2022, doi: 10.1017/eaa.2021.23.
[28] J. Molera, M. Vendrell-Saz, and J. Pérez-Arantegui, "Chemical and Textural Characterization of Tin Glazes in Islamic Ceramics from Eastern Spain," *Journal of Archaeological Science*, vol. 28, no. 3, pp. 331–340, Mar. 2001, doi: 10.1006/jasc.2000.0606.
[29] E. Gliozzo, "Ceramic technology. How to reconstruct the firing process," *Archaeological and Anthropological Sciences*, vol. 12, no. 11, 2020, doi: 10.1007/S12520-020-01133-Y.
[30] M. S. Tite, I. Freestone, R. Mason, J. Molera, M. Vendrell-Saz, and N. Wood, "Lead Glazes in Antiquity—Methods of Production and Reasons for Use," *Archaeometry*, vol. 40, no. 2, pp. 241–260, 1998, doi: 10.1111/j.1475-4754.1998.tb00836.x.
[31] R. F. Geller and E. N. Bunting, "The system PbO-B2O3-SiO2".
[32] "Interactions between Clay Bodies and Lead Glazes - Molera - 2001 - Journal of the American Ceramic Society - Wiley Online Library." Accessed: Apr. 14, 2026. [Online]. Available: https://ceramics.onlinelibrary.wiley.com/doi/abs/10.1111/j.1151-2916.2001.tb00799.x
[33] "(PDF) Discovery, production and use of tin-based opacifiers in glasses, enamels and glazes from the Late Iron Age onwards: A reassessment," *ResearchGate*, Accessed: Apr. 14, 2026. [Online]. Available: https://www.researchgate.net/publication/229670572_Discovery_production_and_use_of_tin-based_opacifiers_in_glasses_enamels_and_glazes_from_the_Late_Iron_Age_onwards_A_reassessment
[34] "Abu'l-Qasim's Treatise." Accessed: Mar. 27, 2026. [Online]. Available: https://islamicceramics.ashmolean.org/Glossary/abulqasim.htm
[35] "The production of a lead glaze with galena: Thermal transformations in the PbS–SiO2 system - Di Febo - 2018 - Journal of the American Ceramic Society - Wiley Online Library."

Accessed: Mar. 27, 2026. [Online]. Available: https://ceramics.onlinelibrary.wiley.com/doi/full/10.1111/jace.15346
[36] "From Glass to Glaze in al-Andalus: Local Invention and Technological Transfer | Request PDF," *ResearchGate*, Feb. 2026, doi: 10.1017/eaa.2021.23.
[37] "Abu'l Qasim's Treatise on Ceramics | Semantic Scholar." Accessed: Apr. 14, 2026. [Online]. Available: https://www.semanticscholar.org/paper/Abu%27l-Qasim%27s-Treatise-on-Ceramics-Allan/cfc7a20df764c1af77999cb17d731cd2b9144624
[38] "(PDF) Discovery, production and use of tin-based opacifiers in glasses, enamels and glazes from the Late Iron Age onwards: A reassessment," *ResearchGate*, Accessed: Apr. 14, 2026. [Online]. Available: https://www.researchgate.net/publication/229670572_Discovery_production_and_use_of_tin-based_opacifiers_in_glasses_enamels_and_glazes_from_the_Late_Iron_Age_onwards_A_reassessment
[39] E. Salinas and T. Pradell, "The introduction of the glaze in al-Andalus: Technological waves and Oriental influences," *Libyan Studies*, vol. 51, pp. 87–98, Nov. 2020, doi: 10.1017/lis.2020.8.
[40] S. Maltoni and A. Silvestri, "Investigating a Byzantine technology: experimental replicas of Ca-phosphate opacified glass," *Journal of Cultural Heritage*, vol. 39, pp. 251–259, Sep. 2019, doi: 10.1016/j.culher.2019.02.015.
[41] "CUERDA SECA CERAMICS FROM AL-ANDALUS, ISLAMIC SPAIN AND PORTUGAL (10TH−12TH CENTURIES AD): INVESTIGATION WITH SEM–EDX AND CATHODOLUMINESCENCE* - CHAPOULIE - 2005 - Archaeometry - Wiley Online Library." Accessed: Apr. 14, 2026. [Online]. Available: https://onlinelibrary.wiley.com/doi/full/10.1111/j.1475-4754.2005.00217.x
[42] "From tin- to antimony-based yellow opacifiers in the early Islamic Egyptian glazes: Regional influences and ruling dynasties - ScienceDirect." Accessed: Mar. 31, 2026. [Online]. Available: https://www.sciencedirect.com/science/article/pii/S2352409X19302597
[43] E. Salinas, T. Pradell, and J. Molera, "Glaze production at an early Islamic workshop in al-Andalus," *Archaeological and Anthropological Sciences*, vol. 11, May 2019, doi: 10.1007/s12520-018-0666-y.
[44] "Evidence of Tin Oxide Recrystallization in Opacified Lead Glazes - Molera - 1999 - Journal of the American Ceramic Society - Wiley Online Library." Accessed: Apr. 14, 2026. [Online]. Available: https://ceramics.onlinelibrary.wiley.com/doi/abs/10.1111/j.1151-2916.1999.tb02170.x
[45] "(PDF) Synchrotron Radiation Micro-XRD in the Study of Glaze Technology," *ResearchGate*, doi: 10.1007/s00339-010-5639-7.
[46] S. Nikologianni *et al.*, "Provenance and technology of relief and/or lustre glazed ceramics from *Mértola* (Portugal)," *Journal of Archaeological Science: Reports*, vol. 69, p. 105494, Feb. 2026, doi: 10.1016/j.jasrep.2025.105494.
[47] T. P. Ologunwa, "DEVELOPING CERAMICE GLAZE OPACIFIER USING BONE ASH IN NIGERIA", Accessed: Mar. 31, 2026. [Online]. Available: https://www.academia.edu/5391250/DEVELOPING_CERAMICE_GLAZE_OPACIFIER_USING_BONE_ASH_IN_NIGERIA
[48] S. Weiner and O. Bar-Yosef, "States of preservation of bones from prehistoric sites in the Near East: A survey," *Journal of Archaeological Science*, vol. 17, no. 2, pp. 187–196, Mar. 1990, doi: 10.1016/0305-4403(90)90058-D.
[49] C. Rey, C. Combes, C. Drouet, and M. J. Glimcher, "Bone mineral: update on chemical composition and structure," *Osteoporos Int*, vol. 20, no. 6, pp. 1013–1021, Jun. 2009, doi: 10.1007/s00198-009-0860-y.
[50] J. O. Akindoyo, S. Ghazali, M. D. H. Beg, and N. Jeyaratnam, "Characterization and Elemental Quantification of Natural Hydroxyapatite Produced from Cow Bone," *Chemical*

Engineering & Technology, vol. 42, no. 9, pp. 1805–1815, Sep. 2019, doi: 10.1002/ceat.201800636.

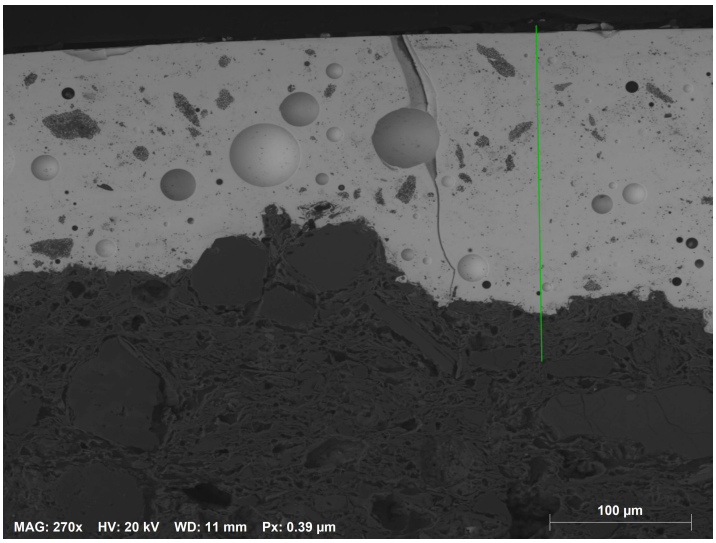
[51] "(PDF) High-Lead Glazed Ceramic Production in Western Iberia (Gharb al-Andalus) between the 10th and Mid-13th Centuries: An Approach from the City of Évora (Portugal)," *ResearchGate*, Mar. 2026, doi: 10.3390/ceramics6040135.

[52] D. Santacreu, J. C. Carvajal López, and A. Durán Benito, Eds., *Mineralogical Approaches to Archaeological Materials: Technological and Social Insights*. Basel: MDPI - Multidisciplinary Digital Publishing Institute, 2022.

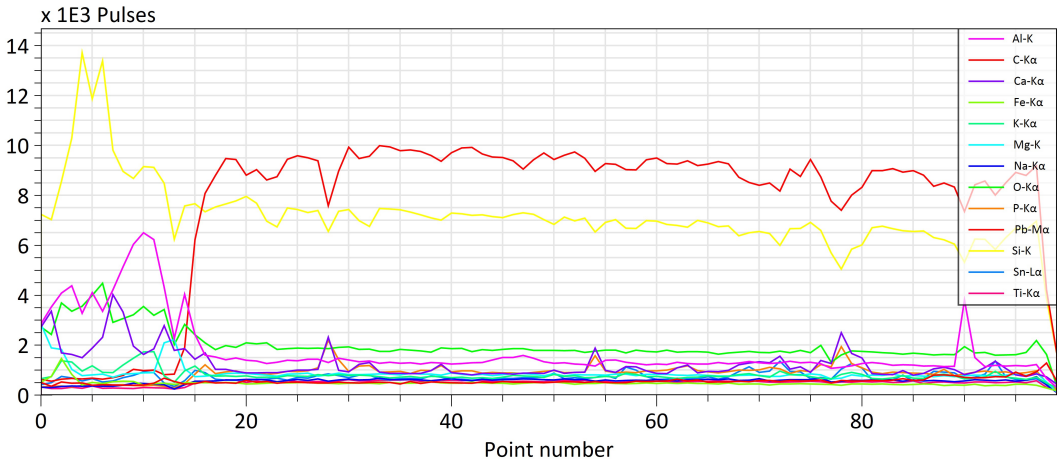
[53] J. Molera, T. Pradell, N. Salvadó, and M. Vendrell, "Interactions between Clay Bodies and Lead Glazes," *Journal of the American Ceramic Society*, vol. 84, pp. 1120–1128, Dec. 2004, doi: 10.1111/j.1151-2916.2001.tb00799.x.

Supporting info

Application Note



Name	Date	Time	HV [kV]	Mag	WD [mm]
Ch 1	12/21/2025	1:15:15 PM	20.0 keV	270x	11.0 mm





Name	Date	Time	Points	Length
Scan data	12/21/2025	1:30:32 PM	100	237.2 µm

Acknowledgements

First and foremost, I would like to express my deepest gratitude to my supervisor, Professor Lorenzo Malavasi. I am sincerely grateful for the opportunity to work on this project and for the trust he placed in me, allowing me to conduct my research with independence while always providing insightful guidance. Thank you for introducing me to this fascinating challenge: combining Materials Science with the world of Cultural Heritage. This interdisciplinarity has not only enriched my academic background but has also profoundly shaped my perspective on scientific research.

My sincere thanks go to my co-supervisors, Massimo Beltrame and Professor Mathilda Larsson Dias Coutinho, for their constant support and mentorship at the HERCULES Laboratory in Évora. Their expertise, patience, and daily guidance during the experimental phase were fundamental to the success of this work. I would also like to thank the former director of the laboratory, Professor José Mirão, for welcoming me into such a prestigious research environment.

Completing this thesis has been much more than an academic achievement; it has been a profound lesson in endurance and resilience. I am deeply grateful for everything this journey has taught me.

I would like to dedicate a special thanks to my friends, who were my pillars of support and made this journey lighter. Thank you to Cate, for always knowing how to make me laugh; to Maria, Bea, Anna, Saaud, Ester, Lucrezia, Diego, Salvo, and Nicoló, whom I met in Evora, for being as you are and for your constant presence.

I am deeply grateful to the cities that have been the background of my academic journey, and the theather of so many encounters. To Pavia, my city of study, and to Évora, for welcoming me so warmly and for teaching me invaluable lessons, both professional and personal.

Finally, a special thanks to my family. Thank you for always standing by my side, for your unwavering support, and for believing in my abilities even when I doubted them myself.

And lastly, to myself: for the tenacity, the long hours in the lab, and the courage to see this through to the end.



GC-CIGA

Ref. : 2023.13937.PEX – DOI: https://doi.org/10.54499/2023.13937.PEX